FUNDAMENTAL STUDIES OF RESPONSIVE MICROGEL THIN FILMS AT INTERFACES

A Dissertation
Presented to
The Academic Faculty

by

Courtney Davis Sorrell

In Partial Fulfillment
of the Requirements for the Degree
Doctor of Philosophy in the
School of Chemistry and Biochemistry

Georgia Institute of Technology
August 2008

FUNDAMENTAL STUDIES OF RESPONSIVE MICROGEL THIN FILMS AT INTERFACES

Approved by:

Dr. L. Andrew Lyon, Advisor
School of Chemistry & Biochemistry
Petit Institute for Bioengineering & Bioscience
Georgia Institute of Technology

Dr. Jiri A. Janata
School of Chemistry & Biochemistry
Georgia Institute of Technology

Dr. Arthur J. Ragauskas
School of Chemistry & Biochemistry
Institute of Paper Science & Technology
Georgia Institute of Technology

Dr. Haskell W. Beckham
School of Chemistry & Biochemistry
School of Polymer, Textile, & Fiber Engineering
Georgia Institute of Technology

Dr. Gary J. Pielak
Department of Chemistry
Department of Biochemistry & Biophysics
The University of North Carolina at Chapel Hill

Date Approved: June 13, 2008

For Muz

ACKNOWLEDGEMENTS

I am grateful to many people for their assistance and support throughout my time at Georgia Tech. First and foremost, I would like to thank Prof. L. Andrew Lyon, not only for his unwavering support, patience, and periodic assistance with long-lost instrumentation and techniques in the lab, but for giving me a chance in the first place. Without his timely intervention, I would not be here today. I would like to thank the rest of the members of my committee, Prof. Janata, Prof. Ragauskas, and Prof. Beckham at Georgia Tech for their advice and support during my research. I would also like to thank Prof. Pielak at UNC-CH for being not only a last-minute addition to my committee, but also a good friend and full of indispensible advice for much of my life.

Many of my colleagues and fellow students have been instrumental in my success at Georgia Tech and I would like to thank them individually. First, a heartfelt thank you to all past and present members of the Lyon Group without whom I would have been lost, in general. I would like to particularly thank Dr. Mike Serpe, Dr. Jonathan McGrath, Bart Blackburn, Zhiyong Meng, and Grant Hendrickson for their assistance on specific aspects of my research. I also want to extend thanks to my many friends and colleagues who have provided me with their support, guidance, and much-needed diversions from time to time: Brandy Moneypenny, Elaine Monbureau, Dawn Zarimba, Meg Morris, Kiisa Wiegand, Cameron Thomson, Shelby Highsmith, Angie and Tushar Thrivikraman, Stefanie McCans, Alexis Neill, Jane Brzostowicz, Andrea Gersh, Natalie Carpenter, Krystyn Hall, Sarah Chi, and Eric Horowitz.

Additional thanks go to people in industry who have helped me with data collection and analyses throughout my research: Dr. Ryan Fuierer, Keith Jones, Jason Li, and Jason Bemis at Asylum Research, and Dr. Sigrid Kuebler and Dr. Aym Berges at Wyatt Technologies.

Lastly, I extend my thanks to my family for their unwavering love and support – Mom, Dad, Sue, Liz, Grandmom and Grandpop. And Kitty – of course.

TABLE OF CONTENTS

	Page
ACKNOWLEDGEMENTS	iv
LIST OF CHARTS, SCHEMES, AND TABLES	ix
LIST OF FIGURES	x
LIST OF SYMBOLS AND ABBREVIATIONS	xii
SUMMARY	xiv
CHAPTER	
1 Introduction	15
1.1 Building with Blocks	15
1.2 Impact of Microstructure on Thin Films	16
1.3 Microstructured Hydrogels	19
1.4 Microgel Thin Films	21
1.5 Fabrication and Responsivities of Microgel Films	23
References	28
2 Methods and Instrumentation	33
2.1 Atomic Force Microscopy	33
2.1.1 Introduction	33
2.1.2 Theory	34
2.1.3 Experimental	39
2.2 Quartz Crystal Microgravimetry	45
2.2.1 Introduction	45
2.2.2 Theory	46
2.2.3 Experimental	51

2.3 Surface Plasmon Resonance 55
2.3.1 Introduction 55
2.3.2 Theory 55
2.3.3 Experimental 58
2.4 Conclusions 62
References 63
3 Synthesis and Characterization of Materials 67
3.1 Microgel Synthesis 67
3.1.1 Introduction 67
3.1.2 Methods 74
3.2 Particle Characterization 76
3.2.1 Dynamic Light Scattering 77
3.2.2 Static Light Scattering 78
3.2.3 Refractometry for *dn/dc* Determination 81
References 87
4 Bimodal Swelling Responses in Microgel Thin Films 90
4.1 Introduction 90
4.2 Experimental 91
4.3 Results 98
4.4 Discussion 104
4.5 Conclusions 116
References 118
5 Deformation Controlled Assembly of Binary Microgel Thin Films 120
5.1 Introduction 120
5.2 Experimental 124

5.2.1 Microgel Synthesis 125

5.2.2 Light Scattering Analysis 126

5.2.3 Film Preparation 130

5.2.4 Atomic Force Microscopy Measurements 134

5.3 Results 136

5.4 Discussion 141

5.5 Conclusions 146

References 148

6 Deformation controlled *co*-Cross-linked Microgel Thin Films 151

6.1 Introduction 151

6.2 Experimental 152

6.2.1 Microgel Synthesis 152

6.2.2 Light Scattering Analysis 154

6.2.3 Film Preparation 154

6.2.4 Atomic Force Microscopy Measurements 155

6.3 Results 157

6.4 Discussion 159

6.5 Conclusions 163

References 166

7 Future Directions 168

APPENDIX A: Characterization of Physically Cross-Linked “Paint-On” Colloidal Crystals 170

VITA 186

LIST OF CHARTS, SCHEMES, AND TABLES

Page

Scheme 2.1: Depiction of AFM imaging 36

Scheme 2.2: Depiction of KPFM imaging 38

Chart 2.1: Representation of a cantilever driven magnetically for fluid imaging 41

Chart 2.2: Equivalent circuit representation of a quartz crystal actuator 48

Chart 2.3: Equivalent circuit representation of a quartz crystal actuator employing capacitance nullification 51

Scheme 2.3: Depiction of SPR measurements 57

Scheme 3.1: Environmentally responsive hydrogels 68

Scheme 3.2: Configuration of pNIPAm in water 69

Scheme 3.3: Microgel synthesis 71

Scheme 3.4: “Seed-and-feed” core/shell microgel synthesis 72

Scheme 3.5: Mechanism for periodate cleavage of 1,2-diols 73

Table 3.1: Results of the *dn/dc* values for *co*-cross-linked microgels 84

Scheme 4.1: Schematic depiction of the bimodal swelling model 92

Table 4.1: Calculated mass data for films constructed with 15 000 MW PAH 113

Table 4.2: Calculated mass data for films constructed with 70 000 MW PAH 113

Scheme 5.1: Depiction of film formation and AFM characterization 122

Table 5.1: Particle properties for microgel products **(1)3** and **(2)3** 127

Table 5.2: Film composition results determined by AFM 138

Table 6.1: Amounts of reactants for synthesis for co-cross-linked microgels 153

Table 6.2: Particle properties for *co*-cross-linked microgels 155

Table 6.3: Analysis of change in particle height due to degradation 157

LIST OF FIGURES

Page

Figure 2.1: Representative AFM image of a binary film 40

Figure 2.2: Representative AFM images of a microgel film in air and in liquid 42

Figure 2.3: KPFM analysis of a 2.5-bilayer microgel film 44

Figure 2.4: KPFM analysis of an APTMS functionalized glass cover slip 44

Figure 2.5: Impedance analysis of a 5 MHz quartz crystal 49

Figure 2.6: Impedance analysis data for microgel layer-by-layer films 52

Figure 2.7: Graph of QCM data from the capacitance nulling experiment 53

Figure 2.8: Representative QCM data for a 1.5-bilayer microgel film 54

Figure 2.9: Photograph of the SPR instrument 60

Figure 2.10: Representative SPR data for a 3-bilayer microgel film 61

Figure 3.1: Graphs of representative dRI data for *dn/dc* determination 83

Figure 4.1: AFM image showing film thickness analysis 97

Figure 4.2: AFM Images showing film characterization 98

Figure 4.3: Graph of AFM thickness data 99

Figure 4.4: Graph of SPR thickness data 101

Figure 4.5: Graph of ellipsometry thickness data 103

Figure 4.6: SPR data for 2.5- and 3-bilayer films 105

Figure 4.7: Wavelength resolved SPR data for 2.5- and 3-bilayer films 106

Figure 4.8: SPR data for a 4.5 layer film constructed with 70 000 MW PAH 108

Figure 4.9: QCM time course data for films constructed with 15 000 MW PAH 110

Figure 4.10: QCM time course data for films constructed with 70 000 MW PAH 111

Figure 5.1: Analysis of particle electrophoretic mobility as a function of pH 129

Figure 5.2: AFM images of the jamming experiment 132

Figure 5.3: Graph of the surface coverage jamming limit as a function of ionic strength 133

Figure 5.4: AFM images of binary microgel monolayer films 135

Figure 5.5: Size analysis for microgels **(1)3** and **(2)3** by AFM 138

Figure 5.6: Surface coverage of each particle represented in the films 140

Figure 5.7: Representative line profiles for non-degraded and degraded films 142

Figure 5.8: Number of each particle represented in the films 144

Figure 6.1: AFM images of microgel **9** 158

Figure 6.2: AFM images of microgels **6** and **7** 160

Figure 6.3: AFM analysis of films composed of microgel **4** 162

Figure 6.4: AFM images of microgel **8** after degradation 164

Figure A.1: AFM images of unannealed crystals, in air 176

Figure A.2: AFM images of crystals annealed for 3 days, in air 177

Figure A.3: AFM images of crystals annealed for 6 days, in air 178

Figure A.4: AFM images of crystals annealed for 3 days, unwetted, in air 179

Figure A.5: AFM images of crystals annealed for 6 days, unwetted, in air 180

Figure A.6: AFM images of crystals annealed for 6 days, in water 181

LIST OF SYMBOLS AND ABBREVIATIONS

NIPAm	*N*-Isopropylacrylamide
pNIPAm	poly(*N*-Isopropylacrylamide)
AAc	Acrylic acid
pNIPAm-*co*-AAc	poly(*N*-Isopropylacrylamide-*co*-acrylic acid)
BIS	*N,N'*-Methylene(bisacrylamide)
DHEA	*N,N'*-(1,2-Dihydroxyethylene)-bisacrylamide
APS	Ammonium persulfate
SDS	Sodium dodecyl sulfate
$NaIO_4$	Sodium periodate
PBS	Phosphate Buffered Saline
APTMS	3-Aminopropyltrimethoxysilane
MPTMS	3-Mercaptopropyltrimethoxysilane
MEA	2-Mercaptoethylamine
DI	deionized
AFM	Atomic Force Microscopy
KPFM	Kelvin Probe Force Microscopy
QCM	Quartz Crystal Microgravimetry
SPR	Surface Plasmon Resonance
LCST	Lower Critical Solution Temperature
VPTT	Volume Phase Transition Temperature
PCS	Photon Correlation Spectroscopy
DLS	Dynamic Light Scattering
MALLS	Multi-angle Laser Light Scattering

SLS	Static Light Scattering
RI	Refractive Index
dRI	Differential Refractive Index
MWCO	Molecular Weight Cut Off
MES	2-[*N*-morpholino]ethanesulfonic acid hydrate
PAH	poly(allylamine hydrochloride)
RCF	Relative Centrifugal Force
LbL	Layer-by-layer
scLbL	Spin-coated Layer-by-layer
rms	root mean square
RGD	Rayleigh-Gans-Debye

SUMMARY

The research described covers fundamental studies of environmentally-responsive microgel-based thin films as a function of film architecture, microgel chemistry, film thickness, and environmental stimulus. Studies of multi-layer microgel thin films were conducted primarily using atomic force microscopy (AFM), quartz crystal microgravimetry (QCM), and surface plasmon resonance (SPR), each of which probed different aspects the film architecture as a function of pH of the environment around the film. Binary thin films were constructed by changing the ratios and composition of the microgels in solution to create multi-functional thin films for surface modification applications and were studied using AFM. The basic understanding of how these components create films at surfaces gives us insight into how the films perform and will allow for greater diversity without the guesswork. The morphology of films created from microgels with a degradable cross-linker was examined by AFM as a function of degradation of the particles' structure. This thesis focuses mainly on very thin microgel films (<5 layers) studied using QCM, SPR, and AFM. Additional studies involving the characterization of semi-soft colloidal "paint-on" photonics are discussed in Appendix A.

CHAPTER 1

INTRODUCTION

1.1 Building with Blocks

Throughout the course of human history, people have built and used many kinds of materials in a top-down approach to making tools, clothing, pottery, glass, etc., manipulating materials is to make use of their inherent properties or physical shapes. For example, utilizing a stone to make a knife, a hide and sinew to make clothing, or a piece of wood to make a bowl show man's inherent ability to exploit his environment to suit his needs. However, these tools still retain the original structure/property relationships of the materials from which they were made.

The need for more complex objects requires the use of a bottom-up assembly method whereby seemingly innocuous materials can be transformed into something different, stronger, or bigger. Indeed, every child at some point in his or her development learns to build things in this bottom-up fashion, which is an important learning step in their development because it instills in them a curiosity about their surroundings and helps them to understand the world. On macroscopic length scales, a child's building blocks are often made of wood, plastic, or fabric and are easy for a child to manipulate. As they grow, their abilities to manipulate and build more complex structures are developed until it is almost instinctual to do so. These macroscale building techniques are carried over into the world as houses, offices, and monuments. Nevertheless, more and more of our

complex world is being built on a microscopic scale and that is where attention must be focused in the future.

Microstructured materials can have unusual structure/property relationships, and from early in human history many developments have taken advantage of them. The use of clay to make bowls was an important step in the development of a bottom-up approach to making tools. While clay, sand, fire, and water were all available to early man, the ability to understand how to use all of them to create a bowl, for example, required some understanding of how those materials needed to be put together. Once that process was understood, the technique could be applied broadly to create other tools. The same is true for many materials, some of which were discovered by accident. Stained glass, now known to contain nanomaterials that have a visible absorption spectrum similar to those of quantum dots, is one such case. Stained glass provides an excellent example of a nano- or microstructured materials in which the microstructure adds some property to the material that would not otherwise be present. Colorless glass is useful for constructing windows, but stained glass, because of its bright colors, can be used not only to make windows, but also to create massive and beautiful works of art.

1.2 Impact of Microstructure on Thin Films

The construction of randomly organized micro- and nanostructured films has been dominated by the Langmuir-Blodgett[1,2], chemisorption-from-solution,[3,4] and layer-by-layer techniques.[5,6] The Langmuir-Blodgett (LB) technique was originally designed as a method for transferring layers of surfactants, oils, and fatty acid films from water onto glass. The result was an ability to assemble multiple layers of material on a solid surface

for the study of their optical properties. Interestingly, it was observed that the conformation of the adsorbed material was the same on the substrate as it had been on the liquid surface from which it was adsorbed.[2] Bigelow, *et al.*, stumbled onto the idea that films could be adsorbed from non-polar liquids in a similar fashion to the LB technique, and they touted this procedure as an expansion of the LB method[3], leading to the development of the self-assembled monolayer techniques that have been pivotal in surface modification chemistry research.[4]

The layer-by-layer assembly technique was originally described by Decher, *et al.*, in 1992,[6] and they proposed this methodology as an alternative to and expansion of the Langmuir-Blodgett technique.[5] Decher held that the LB and chemisorption techniques were only useful for certain classes of molecules and that development of the layer-by-layer (LbL) technique would allow researchers to use organic molecules, clays, inorganic clusters, polymers, colloids, and biological materials such as proteins.[5] With these building blocks, the layer-by-layer technique would allow one to construct materials with greater control over the structures and functions of the films. Decher suggested that films constructed via these methods could be used for optics and sensors applications, as well as for friction-reducing coatings. In the intervening years, researchers have exploited Decher's idea for the development of many kinds of layered materials,[7-9] continuing at the same time to characterize the fundamental polymer chemistry and physics of the new structures.[10]

As per Decher's projection, a particularly interesting and growing area of film and materials construction is the use of hydrogel microparticles (microgels) as building blocks, whereby hydrogels are used to create responsive films with properties that are

tunable or switchable via external stimuli. One can visualize the construction of microgel films by means of a "bricks and mortar" analogy. In general, microstructured films using materials such as hydrogels are built from the substrate in the same way that a brick wall is built from the ground up. In these films, the micron-sized components represent the bricks, and they can largely dictate the functionality and behavior of the film. The "mortar" can be any of a number of materials that interacts with the "bricks", such as a linear polyelectrolyte with a charge opposite that of the microgel.

To extend the utility of the polyelectrolyte LbL technique, Kim and co-workers have developed a method to build robust multilayer biomaterials by forming covalent links between the layers. Layered assemblies of dendrimers and enzymes were easily fabricated by simple reductive amination chemistry.[11] Starting with an amine-terminated gold surface, periodate-treated glucose oxidase was immobilized at a surface via a Schiff base reaction. Layer buildup was achieved by exposing the enzyme layer to an amine-terminated dendrimer. By alternating the enzyme and dendrimer building blocks, these researchers were able to build a multilayer thickness-controlled glucose sensing interface.

Decher and others have since developed methods for changing the composition of the film through changes in the concentrations of the depositing solutions,[12] creating stable core/shell nanoparticles via layer-by-layer deposition,[13] and constructing free-standing membranes composed of polyelectrolyte multilayers.[14] The use of layer-by-layer and adsorption kinetics techniques to create complex microgel materials has been explored.[15-17] Randomly assembled micro- and nanostructured materials have also been constructed and characterized as composite film structures using microgels,[18,19] dendrimers,[20] and star polymers[21] embedded in hydrogel networks. These efforts have enabled a broad range of

studies to be carried out to explore both the fundamental and applied aspects of layer-by-layer assembly. Considerable research has gone into developing multilayer films that function as electrodes,[22] non-fouling surfaces,[23] tunable drug and other controlled-release substrates,[19,24,25] and materials for lightweight and flexible display screens.[26,27] In addition to these applications, several studies have investigated ways to construct thin films on unconventional substrates such as hydrophobic surfaces[28] and through unconventional means like micropatterning,[29] or by creating films using pH tunable polyelectrolytes to control deposition.[30]

1.3 Microstructured Hydrogels

The characteristics of responsive, water-soluble polymers and swellable gels have been studied extensively[31] and are touted by many researchers as valuable starting materials for drug delivery and separation systems, chemomechanical actuators, controllable membranes for separations, and sensors.[32] One of the most extensively studied thermoresponsive polymers is poly(*N*-isopropylacrylamide) (pNIPAm), which undergoes a sharp volume phase transition in water as the temperature increases above 32 °C,[31] changing from a random coil to a globular conformation: its overall structure is maintained despite a sudden decrease in the degree of swelling. These polymer networks are often described as "smart" materials.

Polymer nanocomposites have been extensively studied for about 20 years[33] and these materials introduce completely new combinations of properties to the performance space of traditional polymers. Properties such as increased optical clarity, self-passivation, and decreased permeability have been achieved with low volume additions of nanoparticles

such as clay (1-5% as compared with 15-40% of traditional fillers).[33] These materials have been extensively studied by Haraguchi, whose research has focused on soft, responsive hydrogels.[34-38] He reported that these materials, compared with traditional hydrogels, exhibited extraordinary mechanical, optical and swelling/deswelling properties, which he attributed to the idea that the polymer chain lengths were more uniform than those of a gel network with a chemical cross-linker. Haraguchi has studied the effects of cross-linker concentration on the material's mechanical and optical properties[34] and on the mechanisms of gel formation.[35,37] These efforts elucidated some of the basis for the enhanced mechanical properties of these films, namely that a polymer "shell" appears to surround the platelets and to influence gel formation and mechanics.[36,37] This platelet-polymer clustering phenomenon creates a microstructure, which is known to add strength to polymeric materials.[19]

Some research has also been done in the area of composite films. Dawson and co-workers described these structures as "plum-pudding" gels[39] and they observed two interesting phenomena that result from their structures. The first was that some of the inherent problems with the responsivity of bulk pNIPAm gels were overcome by the incorporation of microgels. They found that even low microgel loading amounts (10-20 mol%) decrease the relaxation time of the shrinking kinetics and dramatically reduces the "skin layer" formation in bulk gels. They also found by incorporating 20 mol% of NIPAm microgel particles that they could induce thermoresponsivity in a heretofore unresponsive gel network made from *N*,*N*-dimethylacrylamide. The other gel properties remained intact.

In the area of thin-films research, Lyon and co-workers showed that if microgels were polymerized into a thin film gel matrix, their impact on the dynamics of the film structure were meaningful.[18] In a hydrogel thin film, it appears as though a restructuring of the polymer matrix occurs following the film volume phase transition. When microgels are present in the film, this restructuring occurs faster indicating that the microgels facilitate this process. Similarly, dendrimer-hydrogel composites show improved responsivity as a function of dendrimer incorporation.[25] Work by Zhuo and co-workers showed that microgel impregnated hydrogel films had improved responsivity as a function of microgel loading.[19] They were also able to show that the mechanical strength properties of the gel were improved, though this phenomenon did not scale linearly with microgel loading. Improved mechanical properties in everyday products such as paper have been demonstrated upon adding microgels or linear polymers to the polymer matrix. Work done by Pelton and co-workers[40] showed that microgels adsorbed to handsheets greatly enhanced the strength of wet paper, but microgels impregnated into filter paper disrupted the fiber-fiber interactions and reduced its tensile strength. On the other hand, linear polymers had the opposite effects on handsheets and filter paper. Thus, treating paper with microgels followed by treatment with linear polymers greatly increased the strength of wet paper.

1.4 Microgel Thin Films

It is clear from the studies described in previous sections that a substance's microstructure has a positive impact on structure/property relationships when that substance is included as a filler in bulk materials. If microgels are incorporated as

additives into larger structures (e.g. hydrogels), it is apparent that they will influence the material in a different way than by dominating its morphology. The materials will most like have the same properties they had before, but the microstructure may impart additional strength, responsivity, or other properties not yet determined. While only preliminary studies into these complex structures have been accomplished, they do give us a window into seeing how the properties of the building block will influence the properties of the entire structure. From this glimpse we can infer that incorporating more functionality into these building blocks will accordingly change the structure/property relationships of the materials.

When the bulk materials (e.g. films) are built primarily from microgels or other microsctructures such as dendrimers, the properties of those building blocks will dominate the properties of the materials that they form. Microgels maintain many of the advantages of bulk hydrogels, such as thermoresponsity and shape memory, but they have enhanced properties such as faster deswelling rates.[41]

Lyon and co-workers developed a spin-coating layer-by-layer (scLbL) technique to build multilayer polyelectrolyte microgel films.[42] This procedure provides a faster and more homogenous method for building the films and gives a linear increase in film thickness.[17,42] They further showed that the formation of polyelectrolyte films using microgels has little impact on the *ability* of the film to respond to its environment, but that the films do respond *differently* than discrete microgels in solution.[17] Films of this nature are ideal for the work proposed here because they are readily assembled and their structure/property relationships are tunable. Using microgels also allows for the facile

incorporation of different building blocks without significantly changing the fabrication techniques.[43]

Inspired by these efforts, Lyon and co-workers have looked at the properties and potential uses of thin films constructed from microgel particles.[42,44-47] Microgels are interesting in their own right because of their potential to be used in controlled release applications.[42,44,47,48] Using microgels in a thin film format will combine their excellent properties as potential "capsules" with a construction method that can be more easily manipulated by the immediate surrounding environment. Using hollow or degradable core/shell particles further increases the utility of the microgel and the thin film for drug encapsulation and release.[49,50] Sensor applications for biologically relevant targets are also on the horizon for microgel particles,[51,52] and their incorporation into particulate thin films could amplify their utility properties and broaden their applications. Other efforts being studied include work on non-fouling surfaces[24] for use in biomedical devices and implant technology. Continuing efforts in these areas will continue to broaden the field of thin film technology as well as to give us a greater understanding of thin film materials.

1.5 Fabrication and Responsivities of Microgel Films

The most facile method for microgel thin film assembly is by passive alternate layer adsorption. Lyon and co-workers introduced the concept of making a layer-by-layer construct composed of thermoresponsive microgel thin films in 2003.[15] Starting with a positively charged surface, polyelectrolyte films were fabricated via a LbL mechanism. In their investigations, a negatively charged microgel made of pNIPAm and acrylic acid (9:1) was synthesized for the building blocks. After adsorption of the microgel,

poly(allylamine hydrochloride) (PAH), a cationic linear polymer, was adsorbed to the film to provide a positive-charged surface onto which the negative-charged microgels can adsorb. Many layered films can conceivably be built in this fashion, but the reported investigation limited itself to applying 5 layers of microgels.

The data presented by Lyon and co-workers in their initial LbL work indicated that the films fabricated in this fashion are formed in a quasi-3-D fashion whereby the first few depositions serve to fill in the base layer closest to the substrate and that subsequent deposition add in the *z*-dimension.[15] It was further shown by their data that films formed at room temperature were more homogeneous than those formed at temperatures above the LCST of the particles, and that the particles deposited at high temperature remained pinned in their deswollen conformation. They further demonstrated that the films retained the responsivities of the microgel building blocks. At pH values below the pK_a of the microgel, the films showed enhanced swelling and deswelling as a function of temperature. At pH values above the pK_a of the particles, however, there was a stepwise decrease in the swelling of the films, which indicated an ability of the films to retain a local pH environment upon cycling.

Following these investigations Lyon and co-workers tried using a spin-coating layer-by-layer (scLbL) technique to build multilayer microgel films by again using a negative-charged microgel with a cationic polymer for the glue.[42] This method introduced a faster and more homogenous method for building the films. They clearly demonstrated by measuring the absorbance of fluorecein isothiocyanate (FITC) labeled insulin pre-loaded into the microgels that the films were built in a linear fashion to at least 9 layers of microgels. Fluorescence micrographs show the uniformity of the films. The pulsatile

release of the insulin from the film further demonstrated that even though these films were built via a more stressful method, the films still retain the responsivities of the microgels. Further studies of these films showed that layer-by-layer deposition remains linear up to at least 30 layers and that drug release rates can be tuned by film thickness.[24] As a result, these materials have become excellent examples for utilization as drug delivery vehicles.

Work done by Lyon and co-workers have clearly demonstrated that the formation of polyelectrolyte films using microgels has little impact on the *ability* of the film to respond to its environment. However, they have shown that the films do have different responses than one would expect from the responsivities of the free microgels in solution.[16,17]

To observe microgel film morphology, a combination of quartz crystal microgravimetry (QCM) and surface plasmon resonance (QCM) spectroscopy has to be employed. In the report by Serpe, *et al.*, it was noted that the microgel films layered with PAH responded in a fashion commensurate with a change in the solvation state of the material.[16] When the film was exposed to pH 6.5 buffer, the attractive forces in the film were enforced, but when exposed to pH 3.0 buffer these same forces were disrupted; these behaviors scaled with film thickness such that thicker films were less perturbed by solvent addition. The researchers further noted that protonation of the AAc in the films did not result in dissolution of the film and that PAH/microgel entanglement must be a contributing factor to film robustness.

Inspired by all of these previous efforts, the research described by this thesis seeks to investigate and develop soft actuators based on small changes in a microgel thin film construct. Soft actuators in this context are defined as sensors employing soft materials.

Much of the inspiration for these projects was provided by a short paper published by Buttry and Lasky in 1989.[53] They noted that when hexokinase was embedded in a polyacrylamide gel attached to a quartz crystal microbalance electrode, the resulting change in the response of the film in the presence of glucose was greater than expected for just a simple binding event. While they were not able to explain in that publication why this phenomenon occurs, it was clear that some morphological change in the film was taking place. Thus, the idea that one could unexpectedly and fundamentally change a film's morphology with a simple binding event or environmental change was conceived. Using microgels in a thin film format could translate their responsive properties into a construct that could be easily manipulated by the immediate surrounding environment. Because the behavior of microgels in solution is well understood, it was reasonable to believe that those properties would translate easily to the situation that instead utilized a microgel thin film. Once its structure was studied and known, changes can be introduced to stimulate the desired response.

The following chapters describe several types of thin films constructed from carefully selected microgel architectures. Briefly, Chapter 2 describes film characterization techniques. A combination of atomic force microscopy, quartz crystal microgravimetry, and surface plasmon resonance spectroscopy was used to elucidate film architecture and to measure their abilities to respond to their environment. Chapter 3 describes the synthesis methods for the microgels and the characterization techniques used to measure the particles' sizes, responsivities, molecular masses, diffusion rates, and other characteristics. If one understands the morphology of the particles, it is straightforward to translate that knowledge to understand how those properties affect film

architecture. Chapter 4 describes the pH responsivities of multilayer microgel thin films and how the structures of the microgels and their complexation and decomplexation properties with different molecular weights of a polycation affect a film's swelling properties.[17] Chapter 5 describes a binary microgel system and how the solution composition affects the film composition.[43] Chapter 6 takes a glance at microgels composed of both degradable and non-degradable cross-linkers and provides some insight into how the film morphology changes with the degree of degradation of the particle. The future directions outlined in Chapter 7 summarize how this body of work has taken a fundamental first step toward the development of deployment of soft actuators.

References

1. Blodgett, K. B.; Langmuir, I., "Built-up films of barium stearate and their optical properties." *Phys. Rev.* **1937,** 51, 964-82.

2. Blodgett, K. B., "Monomolecular films of fatty acids on glass." *J. Am. Chem. Soc.* **1934,** 56, 495.

3. Bigelow, W. C.; Pickett, D. L.; Zisman, W. A., "Oleophobic monolayers : I. Films adsorbed from solution in non-polar liquids." *J. Colloid Sci.* **1946,** 1, 513-538.

4. Schreiber, F., "Structure and growth of self-assembling monolayers." *Prog. Surf. Sci.* **2000,** 65, 151-256.

5. Decher, G., "Fuzzy Nanoassemblies: Toward Layered Polymeric Multicomposites." *Science* **1997,** 277, 1232-1237.

6. Decher, G.; Hong, J. D.; Schmitt, J., "Buildup of untrathin multilayer films by a self-assembly process: III. Consecutively alternating adsorption of anionic and cationic polyelectrolytes on charged surfaces." *Thin Solid Films* **1992,** 210/211, 831-835.

7. Chen, L. H.; McBranch, D. W.; Wang, H. L.; Helgeson, R.; Wudl, F.; Whitten, D. G., "Highly sensitive biological and chemical sensors based on reversible fluorescence quenching in a conjugated polymer." *PNAS* **1999,** 96, 12287-12292.

8. Halls, J. J. M.; Walsh, C. A.; Greenham, N. C.; Marseglia, E. A.; Friend, R. H.; Moratti, S. C.; Holmes, A. B., "Efficient Photodiodes from Interpenetrating Polymer Networks." *Nature* **1995,** 376, 498-500.

9. Churochkina, N. A.; Starodoubtsev, S. G.; Khokhlov, A. R., "Swelling and collapse of the gel composites based on neutral and slightly charged poly(acrylamide) gels containing Na-montmorillonite." *Polymer Gels and Networks* **1998,** 6, 205-215.

10. Mermut, O.; Lefebvre, J.; Gray, D. G.; Barrett, C. J., "Structural and mechanical properties of polyelectrolyte multilayer films studied by AFM." *Macromolecules* **2003,** 36, 8819-8824.

11. Yoon, H. C.; Kim, H. S., "Multilayered assembly of dendrimers with enzymes on gold: Thickness-controlled biosensing interface." *Anal. Chem.* **2000,** 72, 922-926.

12. Hübsch, E.; Ball, V.; Senger, B.; Decher, G.; Voegel, J.-C.; Schaaf, P., "Controlling the Growth Regime of Polyelectrolyte Multilayer Films: Changing from Exponential to Linear Growth by Adjusting the Composition of Polyelectrolyte Mixtures." *Langmuir* **2004,** 20, 1980-1985.

13. Schneider, G.; Decher, G., "From Functional Core/Shell Nanoparticles Prepared via Layer-by-Layer Deposition to Empty Nanospheres." *Nano Lett.* **2004,** 4, 1833-1839.

14. Farhat, T. R.; Hammond, P. T., "Engineering Ionic and Electronic Conductivity in Polymer Catalytic Electrodes Using the Layer-By-Layer Technique." *Chem. Mater.* **2006,** 18, 41-49.

15. Jones, C. D.; Serpe, M. J.; Schroeder, L.; Lyon, L. A., "Microlens Formation in Microgel/Gold Colloid Composite Materials via Photothermal Patterning." *J. Am. Chem. Soc.* **2003,** 125, 5292-5293.

16. Kim, J.; Serpe, M. J.; Lyon, L. A., "Hydrogel Microparticles as Dynamically Tunable Microlenses." *J. Am. Chem. Soc.* **2004,** 126, 9512-9513.

17. Sorrell, C. D.; Lyon, L. A., "Bimodal Swelling Responses in Microgel Thin Films." *J. Phys. Chem. B* **2007,** 111, 4060-4066.

18. Nayak, S.; Debord, S. B.; Lyon, L. A., "Investigations into the Deswelling Dynamics and Thermodynamics of Thermoresponsive Microgel Composite Films." *Langmuir* **2003,** 19, 7374-7379.

19. Zhang, J.; Fredin, N. J.; Janz, J. F.; Sun, B.; Lynn, D. M., "Structure/property relationships in erodible multilayered films: influence of polycation structure on erosion profiles and the release of anionic polyelectrolytes." *Langmuir* **2006,** 22, 239-245.

20. Khopade, A. J.; Caruso, F., "Investigation of the factors influencing the formation of dendrimer/polyanion multilayer films." *Langmuir* **2002,** 18, 7669-7676.

21. Oral, E.; Peppas, N. A., "Responsive and recognitive hydrogels using star polymers." *J. Biomed. Mater. Res. A* **2004,** 68A, 439-447.

22. Farhat, T. R.; Hammond, P. T., "Fabrication of a \"soft\" membrane electrode assembly using layer-by-layer technology." *Adv. Funct. Mater.* **2006,** 16, 433-444.

23. Berg, M. C.; Yang, S. Y.; Mendelsohn, J. D.; Hammond, P. T.; Rubner, M. F., "Controlling mammalian cell adhesion on patterned weak polyelectrolyte multilayers." *Abstracts of Papers, 225th ACS National Meeting, New Orleans, LA, United States, March 23-27, 2003* **2003**, PMSE-026.

24. Nolan, C. M.; Reyes, C. D.; Debord, J. D.; Garcia, A. J.; Lyon, L. A., "Phase transition behavior, protein adsorption, and cell adhesion resistance of poly(ethylene glycol) crosslinked microgel particles." *Biomacromolecules* **2005,** 6, 2032-2039.

25. Zhang, J.; Chua, L. S.; Lynn, D. M., "Multilayered Thin Films that Sustain the Release of Functional DNA under Physiological Conditions." *Langmuir* **2004,** 20, 8015-8021.

26. DeLongchamp, D. M.; Hammond, P. T., "Multiple-Color Electrochromism from Layer-by-Layer-Assembled Polyaniline/Prussian Blue Nanocomposite Thin Films." *Chem. Mater.* **2004,** 16, 4799-4805.

27. DeLongchamp, D. M.; Kastantin, M.; Hammond, P. T., "High-Contrast Electrochromism from Layer-By-Layer Polymer Films." *Chem. Mater.* **2003,** 15, 1575-1586.

28. Park, J.; Fouche, L. D.; Hammond, P. T., "Multicomponent patterning of layer-by-layer assembled polyelectrolyte/nanoparticle composite thin films with controlled alignment." *Adv. Mater.* **2005,** 17, 2575-2579.

29. Park, J.; Hammond, P. T., "Multilayer transfer printing for polyelectrolyte multilayer patterning: direct transfer of layer-by-layer assembled micropatterned thin films." *Adv. Mater.* **2004,** 16, 520-525.

30. Park, S. Y.; Rubner, M. F.; Mayes, A. M., "Free Energy Model for Layer-by-Layer Processing of Polyelectrolyte Multilayer Films." *Langmuir* **2002,** 18, 9600-9604.

31. Schild, H. G., "Poly(N-isopropylacrylamide): experiment, theory and application." *Prog. Polym. Sci.* **1992,** 17, 163-249.

32. Osada, Y.; Gong, J.-P., "Soft and Wet Materials: Polymer Gels." *Adv. Mater.* **1998,** 10, 827-837.

33. Winey, K. I.; Vaia, R. A., "Polymer Nanocomposites." *MRS Bulletin* **2007,** 32, 314-319.

34. Haraguchi, K.; Takehisa, T., "Nanocomposite hydrogels: A unique organic-inorganic network structure with extraordinary mechanical, optical, and swelling/de-swelling properties." *Adv. Mater.* **2002,** 14, 1120-1124.

35. Haraguchi, K.; Li, H. J., "Control of the coil-to-globule transition and ultrahigh mechanical properties of PNIPA in nanocomposite hydrogels." *Angew. Chem., Int. Ed.* **2005,** 44, 6500-6504.

36. Haraguchi, K.; Li, H. J.; Okumura, N., "Hydrogels with hydrophobic surfaces: Abnormally high contact angles for water on PNIPA nanocomposite hydrogels." *Macromolecules* **2007,** 40, 2299-2302.

37. Miyazaki, S.; Endo, H.; Karino, T.; Haraguchi, K.; Shibayama, M., "Gelation mechanism of poly(N-isopropylacrylamide)-clay nanocomposite gels." *Macromolecules* **2007,** 40, 4287-4295.

38. Haraguchi, K.; Li, H. J.; Song, L. Y.; Murata, K., "Tunable optical and swelling/deswelling properties associated with control of the coil-to-globule transition of poly(N-isopropylacrylamide) in polymer-clay nanocomposite gels." *Macromolecules* **2007,** 40, 6973-6980.

39. Lynch, I.; Dawson, K. A., "Synthesis and characterization of an extremely versatile structural motif called the "plum-pudding" gel." *J. Phys. Chem. B* **2003,** 107, 9629-9637.

40. Miao, C. W.; Chen, X. N.; Pelton, R., "Adhesion of poly(vinylamine) microgels to wet cellulose." *Ind. Eng. Chem. Res.* **2007,** 46, 6486-6493.

41. Gehrke, S. H., "Synthesis, equilibrium swelling, kinetics, permeability and applications of environmentally responsive gels." *Adv. Polym. Sci.* **1993,** 110, 81-144.

42. Nolan, C. M.; Serpe, M. J.; Lyon, L. A., "Thermally modulated insulin release from microgel thin films." *Biomacromolecules* **2004,** 5, 1940-1946.

43. Sorrell, C. D.; Lyon, L. A., "Deformation Controlled Assembly of Binary Microgel Thin Films." *Langmuir* **2008**, In press.

44. Nolan, C. M.; Serpe, M. J.; Lyon, L. A., "Pulsatile release of insulin from Layer-by-Layer assembled microgel thin films." *Macromol. Symp.* **2005,** 227, 285-294.

45. Serpe, M. J.; Jones, C. D.; Lyon, L. A., "Layer-by-Layer Deposition of Thermoresponsive Microgel Thin Films." *Langmuir* **2003,** 19, 8759-8764.

46. Serpe, M. J.; Lyon, L. A., "Optical and Acoustic Studies of pH-Dependent Swelling in Microgel Thin Films." *Chem. Mater.* **2004,** 16, 4373-4380.

47. Serpe, M. J.; Yarmey, K. A.; Nolan, C. M.; Lyon, L. A., "Doxorubicin Uptake and Release from Microgel Thin Films." *Biomacromolecules* **2005,** 6, 408-413.

48. Nayak, S.; Lee, H.; Chmielewski, J.; Lyon, L. A., "Folate-mediated cell targeting and cytotoxicity using thermoresponsive microgels." *J. Am. Chem. Soc.* **2004,** 126, 10258-10259.

49. Nayak, S.; Gan, D.; Serpe, M. J.; Lyon, L. A., "Hollow thermoresponsive microgels." *Small* **2005,** 1, 416-421.

50. Nayak, S.; Lyon, L. A., "Ligand-functionalized core/shell microgels with permselective shells." *Angew. Chem., Int. Ed.* **2004,** 43, 6706-6709.

51. Kim, J.; Nayak, S.; Lyon, L. A., "Bioresponsive Hydrogel Microlenses." *J. Am. Chem. Soc.* **2005,** 127, 9588-9592.

52. Kim, J.; Singh, N.; Lyon, L. A., "Label-free biosensing with hydrogel microlenses." *Angew. Chem., Int. Ed.* **2006,** 45, 1446-1449.

53. Lasky, S. J.; Buttry, D. A., "Detection of Glucose Using Hexokinase." *ACS Symposium Series: Sensors Based on Biomolecules Immobilized on the Piezoelectric Quartz Crystal Microbalance* **1989,** 403, 237-246.

CHAPTER 2

METHODS AND INSTRUMENTATION FOR FILM CHARACTERIZATION

Chemistry, and the chemistry of materials in particular, deals with the structures, properties, and interactions within systems composed of atoms and molecules; the limit to the size of the system is restricted only by the precision with which small changes need to be understood.[1] Several techniques were employed to gain an intimate understanding about systems designed from microgels. A fundamental understanding of these materials allows for expansion of applications for which these materials can have an impact. Several techniques were employed to characterize films constructed from microgels, namely atomic force microscopy (AFM), quartz crystal microgravimetry (QCM), and surface plasmon resonance (SPR). It is important to understand these techniques so that the data can be interpreted in a meaningful manner. This chapter seeks to explain each of the primary techniques used for film characterization. Some experimental details and data are also included.

2.1 Atomic Force Microscopy

2.1.1 Introduction

Atomic force microscopy (AFM) has become very popular for surface and film characterization since its inception in 1986.[1-4] The requirement for an imaging technique

as precise as AFM in addition to other scanning probe techniques reflects the needs for scientists to see and understand chemical systems at sub-micron to atomic level resolution. Microgels, in some cases, are under the diffraction limit (~400 nm) for optical microscopy and a more sensitive technique must be used. Advances in scanning probe microscopy have allowed scientists to see at the molecular and atomic levels, and even to differentiate between spin states on molecules. As a result, many research programs have incorporated this technique to elucidate and understand the myriad structure/property relationships of layer-by-layer films,[5,6] colloidal systems,[7-10] polymer blends,[11-13] and semiconductor materials.[4] While the studies presented in this thesis were not intended to look at these systems at the atomic level, the use of atomic force microscopy gave us a window through which to examine these materials at the nanometer scale.

2.1.2 Theory

AFM operates on a relatively simple principle. Using the forces inherent between two materials (e.g. van der Waals, magnetic, capacitance, etc.), a probe of finite sharpness is used to scan a surface. Line scans are performed in the x-y plane of finite dimensions to give a topographical "map" of the surface. Interaction of the probe tip with objects in the scanned area also gives information about the sample. The first AFM microscopes used a contact mode method which dragged the sharp tip across a sample in a line-by-line fashion to reveal the topography of surfaces while giving information about tip-surface interactions. In recent years, development of an amplitude modulation (AM) method has been used to probe surfaces. The AM method, described in the following paragraph, reduces the stress on the sample since the tip is not dragged across the surface. The

development of the AM method has greatly improved the AFM technique for use in the study of polymeric, biological, and other soft materials. Performing the imaging process in liquids has been developed for use in biological systems, but it is also valuable for studying polymer systems. The resolution is not changed by imaging within a liquid phase, but more care must be taken when imaging such samples. Amplitude modulation is the preferred mode for imaging in liquids.

During imaging, the area under study is scanned using a piezoelectric-based positioning system. The exact method of scanning is unique to each brand of AFM instrument, but the principles remain the same. The piezoelectric effect (Section 2.2.2) is used to drive either the tip assembly or a sample stage to scan the surface. Briefly, an electrical current is applied asymmetrically to a piezo-active material coupled to the tip assembly or sample stage, which drives it in a particular direction. Changing the direction of the bias will change the direction that the piezo element has moved the tip or sample. The magnitude of the bias influences the magnitude of the deformation of the piezo-active material such that using several piezo elements in conjunction gives the instrument the dynamic range to move in three dimensions with great precision and accuracy. An AC voltage is also applied to a piezo material coupled to the cantilever to oscillate the cantilever base and drive the cantilever at its resonant frequency. When the cantilever is in resonance, it “taps” the surface during imaging.

AFM cantilevers are made from the same silicon materials used mainly in microchip technology. Each cantilever has one tip located at the end that is used to probe the sample. Average AFM tips have a diameter of ~10 nm, but their sharpness will decrease

Scheme 2.1. Cartoon depicting atomic force microscope imaging of a microgel sample.

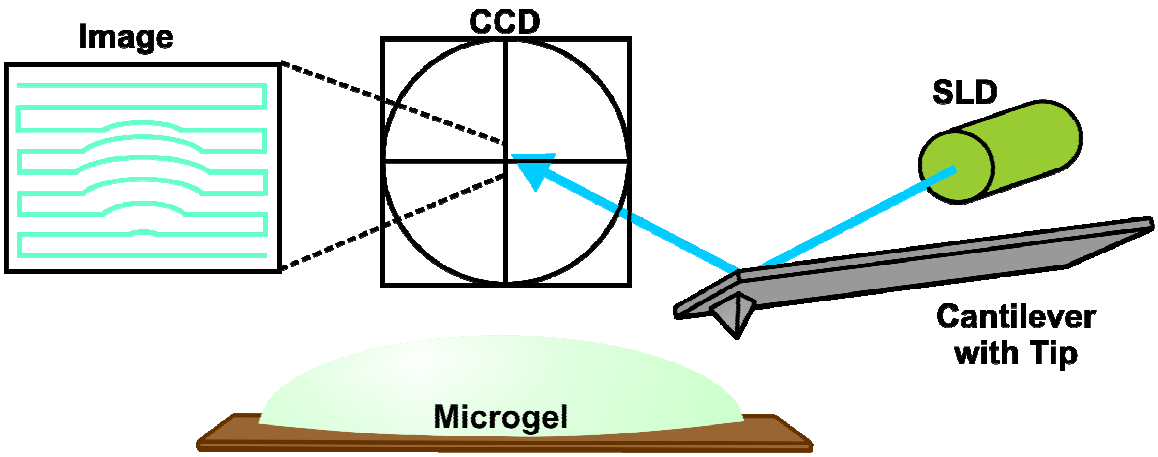

with use. Some convolution of the microgel's size in the xy plane is expected due to the tip shape and dimensions. A contaminated or broken tip will give false images based as much on the topology of the tip as on the topology of the sample. Ultra-sharp tips can be used for obtaining greater resolution on a smaller scale. One major disadvantage of AFM is that only the surface of a system is probed. Although force-volume techniques can give some indications about the softness or deformability of a material, these procedures are still limited as to the information that they provide about a material's inner workings. Combining AFM with optical techniques like confocal fluorescence or Raman microscopy techniques has been very popular for correlating surface topology with information about the interior structure of a material.

As previously mentioned, the image of a sample is a topographical map that represents the signal obtained from a laser reflected from the cantilever as it scans the surface (Scheme 2.1). The image is recorded indirectly by measuring the deflection of the

cantilever as it passes over the surface. This measurement is accomplished by shining a super luminescent diode (SLD) or laser on the back of the cantilever. The SLD signal is deflected from the back of the cantilever onto a CCD camera programmed with a Cartesian coordinate plane. Changes in the laser's position on this coordinate plane are recorded as variations in the deflection of the cantilever. The deflection term is converted to changes in the height and lateral dimensions of the sample which is recorded as a false-color or grayscale image. When performing AM imaging, the resonant frequency associated with the cantilever has an associated phase angle (similar to a simple harmonic oscillator). The phase is simply the lag (or lead) time between the response and drive sine waves; it is expressed in angular units (degrees or radians). Depending on the sample, changes in the phase angle can be interpreted as changes of a sample's morphology (e.g. stickiness, softness, sharpness, etc.) because the the tip's interaction with the surface changes the resonant frequency of the cantilever enough to affect the phase angle of the modulation. If the tip is being repelled by the surface these changes will be recorded as a negative phase change; and if it is being attracted by the surface the changes will be recorded as a positive phase change. Most imaging is performed so that the phase remains in the repulsive mode, but the changes in the phase are recorded relative to the initial set point.

Advanced techniques using scanning probe microscopy are also widely used for studying complex materials. In particular, Kelvin probe force microscopy (KPFM), or surface potential imaging, is very useful for understanding the contact potential difference between materials, which can depend on a variety of parameters such as the work function, adsorption layers, or temperature changes of a sample.[14,15] For this

technique, the use of a conductively coated cantilever is required. The tip is vibrating in non-contact mode above the surface of the sample (Scheme 2.2). An AC bias is applied to the cantilever to produce an electrical force that is proportional to the potential difference between the tip and the sample. To image with this technique, it is helpful to model the system as a parallel plate capacitor.[14] When a voltage is applied to the system, electrons flow from the material with the smaller work function to the material with a larger work function. The diffusion of current builds up a double layer at the interface which results in an electrostatic potential difference. When equilibrium is reached by shifting of the electron energy levels, the electrostatic force equals the

Scheme 2.2. Measurement cycle for Kelvin probe force imaging.

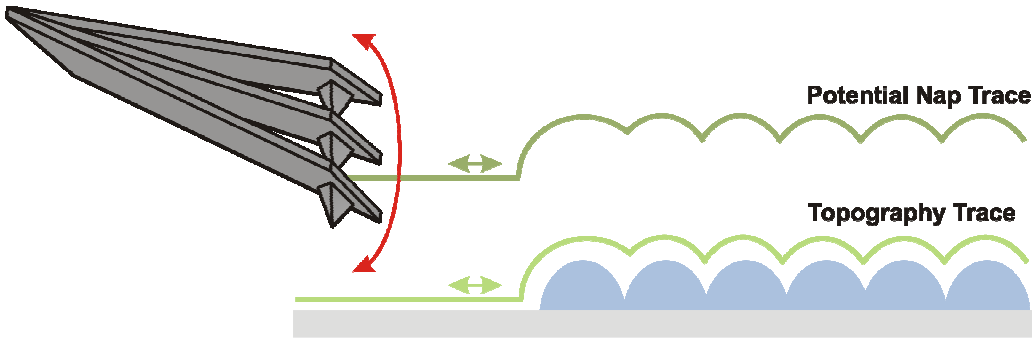

diffusion force and the contact potential equals the difference between the two work functions. KPFM uses the resulting electrostatic force to apply a voltage to compensate for the contact potential until the force is nulled. Variations in the contact potential between the tip and the sample as a result of material inhomogeneity can be easily mapped using a scanning system.

2.1.3 Experimental

All atomic force microscopy images and measurements were performed with an Asylum Research MFP-3D atomic force microscope. Specifics concerning tip use and sample preparation are delineated in the chapters where the data are presented.

In general, samples were prepared on glass cover slips or gold substrates using standard surface functionalization techniques. The samples were affixed to microscope slides using Leitsilber silver paint to ensure that the sample did not slip during imaging. An appropriate tip was selected for each experiment and tuned according to the guidelines provided with the instrument. The dry samples were imaged at scan speeds and sizes appropriate for accurate characterization of the materials under study. For studies requiring several images taken as a survey of the sample (Chapter 5), an add-in program provided by AR for use in the MFP-3D imaging environment was used to take up to 5 or 6 images in sequential fashion such that there was no overlapping. A typical image of microgel films with sample and imaging specifications is shown in Figure 2.1.

Imaging in the liquid phase was performed using the iDrive™ in-liquid imaging attachment designed for the MFP-3D by Asylum Research.[16] An AR-iDrive cantilever (a modified 100 μm triangular shape Olympus BL-TR400PB cantilever with f_0 = 35 kHz in air and k_0 = 0.09 N/nm) was used for in-liquid imaging with the iDrive. Imaging can also

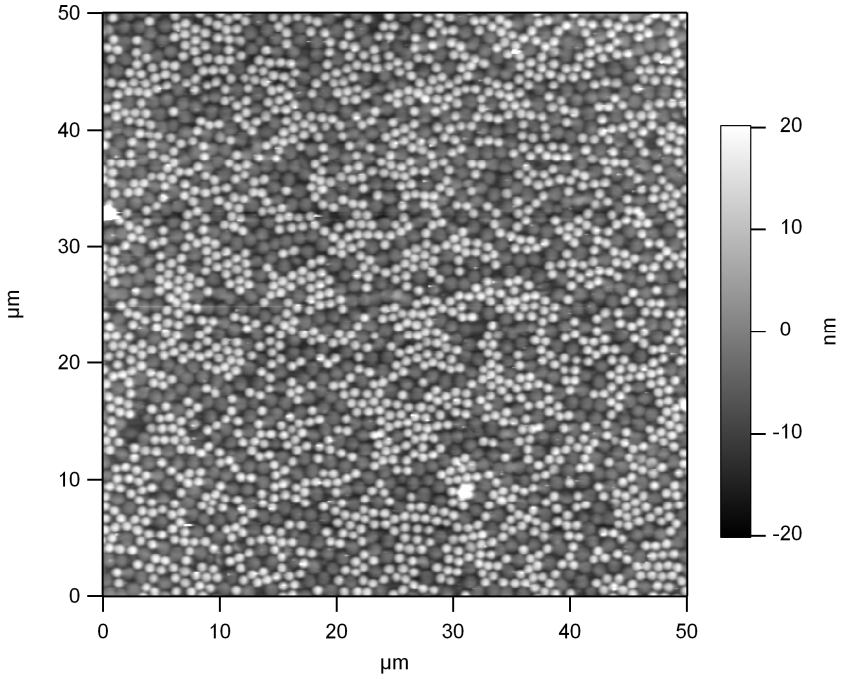

Figure 2.1. Representative binary microgel film. The image shows that the film is composed of two particles of differing softness. Images were recorded at a resolution of 512 scan lines with 512 points per line.

be performed using traditional AM mode imaging techniques and cantilevers designed for liquid imaging. The iDrive™ was specifically designed for polymer and biological samples and employs the Lorentz Force to magnetically actuate the cantilever. All in-liquid images were performed by using a sessile drop of either deionized water or an appropriate buffer on the sample. The cantilever assembly was lowered into the fluid on the sample to create a meniscus between the sample and the cantilever holder. Once immersed in the liquid, the cantilever was tuned and actuated magnetically using the iDrive™. Actuation of the cantilever is accomplished by applying a current through a V-shaped cantilever (typically used for contact mode imaging) that has been coated with gold and wired to couple electronically with a voltage source (Chart 2.1).[17] The current induces a magnetic field perpendicular to the flow of the current. In the presence of a

Chart 2.1. Representation of the cantilever with current *i* circulating along it. In this schematic, the magnetic field vector *B* is directed out of the page.[17]

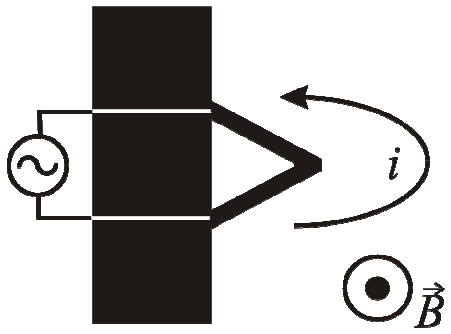

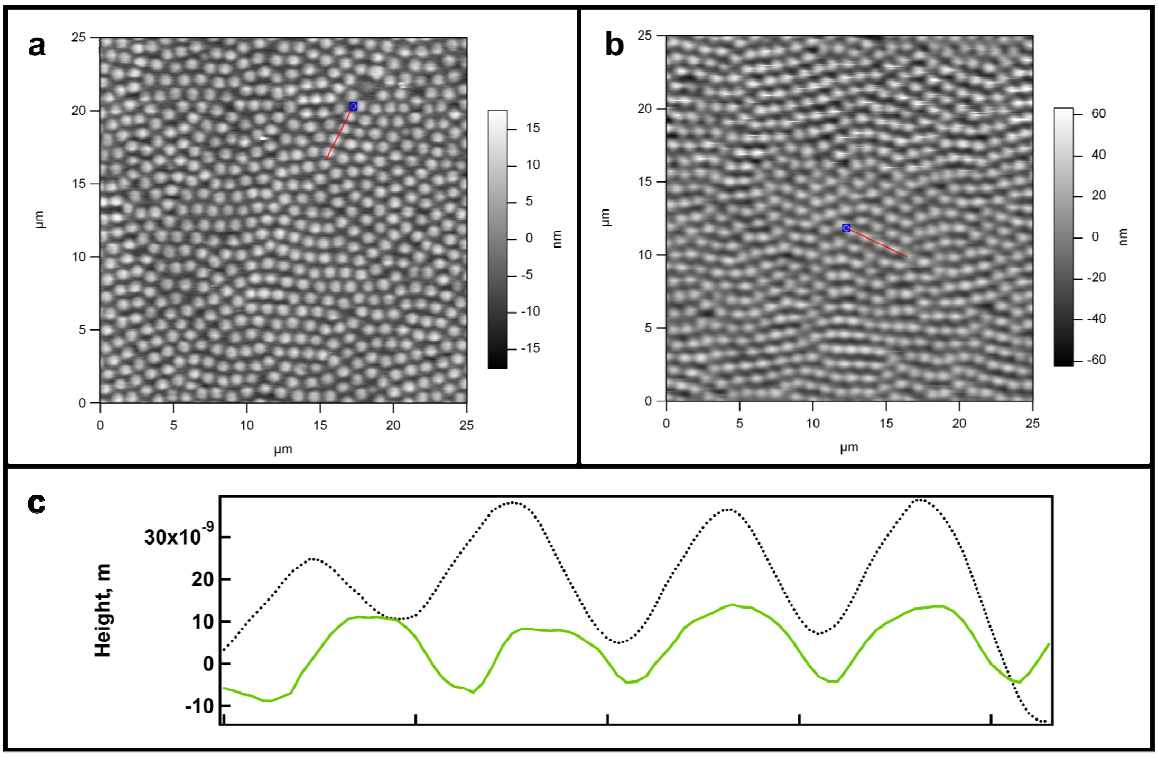

Figure 2.2. AFM images showing a representative *co*-cross-linked microgel film in (a) air and (b) in pH 6.5 buffer. The section graph (c) shows line sections of the film in air (solid, green line) and the film in pH 6.5 buffer (dotted, black line). The line sections clearly show that the film swells. The center-to-center distance does not appear to change indicating that the particles are not moving along the surface to fill space. Images were recorded at a resolution of 512 scan lines with 512 points per line.

magnet, the cantilever will be deflected towards or away from the magnet depending on the direction of the current. Using an alternating current makes the cantilever oscillate in a manner similar to that of traditional piezo-driven AM force microscopy. A typical in-fluid image is shown and compared to its dry analogue in Figure 2.2.

Kelvin probe force microscopy[14] was performed using Olympus Electri-Lever cantilevers (k = 2 N/m, f_0 = 70 kHz) with a platinum coating. A 4-pass imaging technique was used to image the surface and was implemented according to the guidelines set by Asylum Research.[18] The first two passes obtained images of the surface topography using typical AM mode imaging (topography, Scheme 2.2). The second two passes raised the tip above the surface (nap mode) and measured the potential difference between the sample and the tip. This technique was used as a characterization technique for microgel films and silane-functionalized glass surfaces.

A microgel film similar to those presented in Chapter 4 was subjected to KPFM for analysis. In the early stages, several different characterization techniques were applied to these films to make sure that linear, multi-layer build-up was occurring. For KPFM imaging, a spare 2.5-bilayer sample prepared on a gold surface was used and the images are shown in Figure 2.3. The surface potential image (Figure 2.3a) shows that there are four discrete levels: the top three, which represent the microgel film layers, and the lowest, which is probably the gold surface. The false color potential image (Figure 2.3a) shows that the electrostatic potential decreases away from the upper surface of the film. This particular sample does not show complete coverage for all layers, but it does confirm that the buildup occurred in a layer-by-layer rather than space-

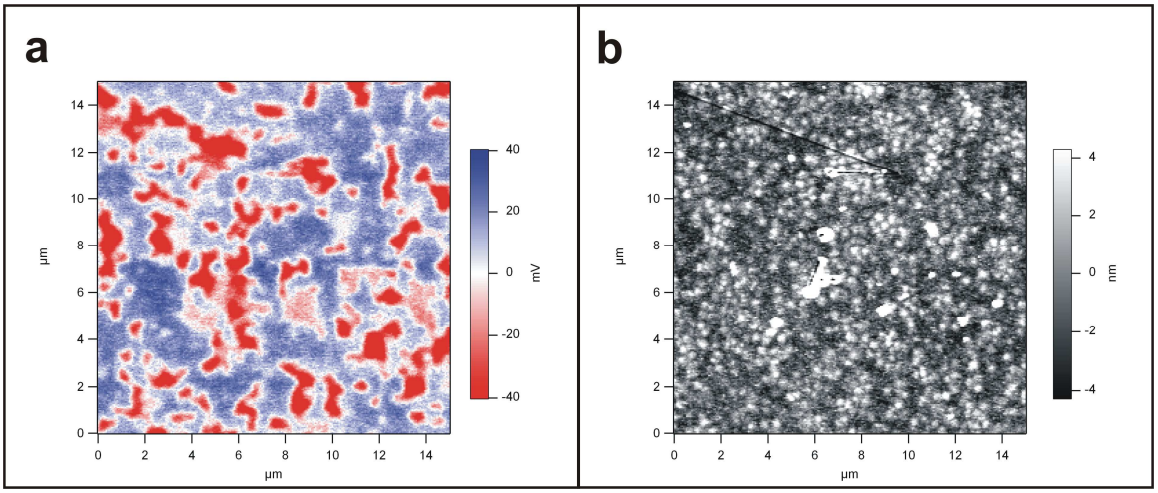

Figure 2.3. AFM image showing (a) surface potential and (b) height traces for a 2.5-bilayer microgel film on gold. The false color in the potential image shows clear layers of the film. Dark blue is the upper most level of the microgel, followed by a second layer in white, and a third layer in "pink". The dark red areas most likely represent the gold surface. This colored representation correlates well with the height image, and areas that are microgel-rich show a good match with the dark blue areas. Images were recorded at a resolution of 256 scan lines with 256 points per line.

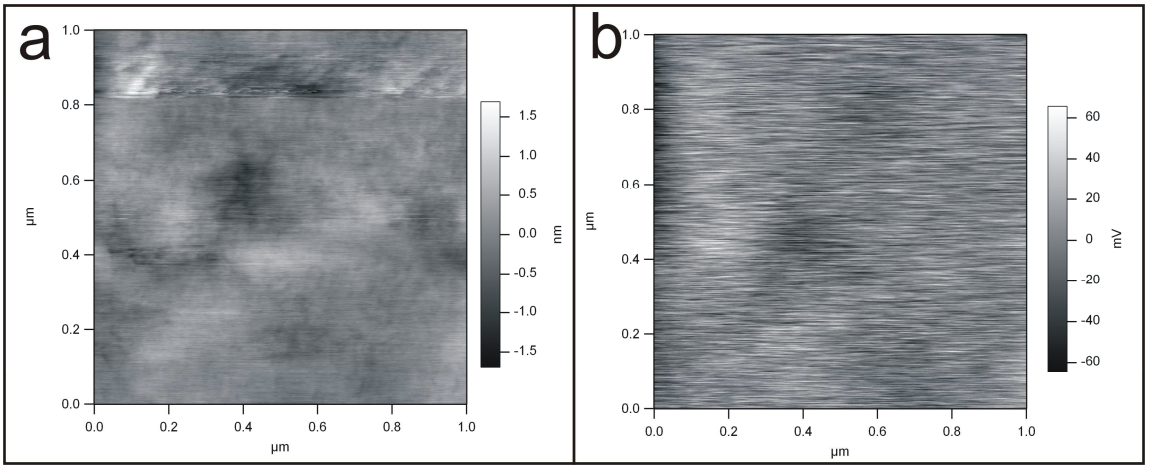

Figure 2.4. AFM images of the a) height and b) surface potential of APTMS functionalized glass. The height image has an RMS roughness of 288 ± 218 pm. The surface potential image has an average potential of +6 pV and an RMS roughness of 16 ± 12 mV. Images were recorded at a resolution of 512 scan lines with 512 points per line.

filling fashion. If one looks at the height trace image (Figure 2.3b), the layers are not easily differentiated, but the microgel-rich areas appear to correspond to the dark blue areas of the film. Clearly, the additional information provided by performing KPFM was invaluable for understanding the film's morphology.

A typical APTMS-functionalized glass slide was also characterized by KPFM (Figure 2.4) to confirm that the surface functionalization provides enough surface charge to create uniform particle sticking for the films studied in Chapters 5 and 6. The average surface charge is +6 pV with rms roughness of 16 ± 12 mV. Figure 2.4 shows that the 1-μm area on the functionalized cover slips covered by each particle has a net positive charge. The roughness of the surface charge, while significant, does not appear to be a factor that hinders particle sticking. It is reasonable to assume that the number of charges in the area under each particle is distributed evenly enough for each particle to have multiple sticking points such that the particle will not diffuse along or desorb from the surface. The height image also shows both that the surface is not rough enough to have impact the particle stickiness and that any surface defects are smaller than a particle with a footprint commensurate with the image size.

2.2 Quartz Crystal Microgravimetry

2.2.1 Introduction

Quartz crystal microgravimetry (QCM) is an electrochemical technique that employs a quartz crystal sandwiched between two metal electrodes.[19] The electrodes establish an alternating electric field across the crystal, causing a vibration at its resonant frequency. This oscillation is sensitive to changes in any mass added to the crystal and the frequency

changes accordingly. Because of its high sensitivity, QCM is ideal for studying small changes in film thickness or morphology of thin films.[20,21] QCM has been used extensively to study information about film dissolution and deposition, surface morphology changes, changes in viscoelasticity of polymer films, and mass changes in thin films caused by myriad chemical or electrochemical processes.[19,22] QCM is most appropriate for study of the morphology of polymer films at a solid-liquid interface, and it has been used in several of the studies presented in this thesis.

2.2.2 Theory

Quartz crystal microgravimetry employs acentric crystals (e.g. quartz, tourmaline, or Rochelle salt) that exhibit the *piezoelectric effect* discovered by the Curie brothers in 1880. Briefly, the piezoelectric effect occurs when stress is applied to an acentric crystal. The stress causes an electric potential forms across the crystal that is proportional to the associated strain. Thus, the *converse piezoelectric effect* states that if a voltage is applied across an acentric crystal, this crystal will exhibit a proportional mechanical strain; applying an alternating electric current will induce vibrations within the crystal. This phenomenon is the basis for QCM. To take advantage of the piezoelectric properties of quartz, QCM uses AT-cut quartz crystal formed by slicing through a quartz rod at an incident angle of 35° with respect to its long axis.

The vibrational motion of quartz establishes a transverse acoustic wave across the crystal such that an antinode of the wave is at the surface of the crystal. Thus any addition to the thickness will result in slight changes to the frequency of the crystal's vibration. These changes can all be expressed by the Sauerbrey equation:

$$\Delta f = -2f_0^2 \Delta m / A(\mu_q \rho_q)^{1/2} \quad (2.1)^{19}$$

where Δf is the measured frequency shift, f_0 the initial frequency of the quartz, Δm the mass change, A the piezoelectrically active area, ρ_q the density of the quartz, and μ_q the shear modulus. This equation however makes three assumptions about the added mass layer:

1. the mass layer is impedance matched to the crystal such that the system can be treated as a composite resonator,
2. the mass layer is firmly attached to the electrode such that there is no slippage between the electrode and the adjacent layer during the shear motion of the disk, and so the attached layer and the electrode move at the same velocity, and
3. the mass layer is uniformly distributed across the crystal surface. This assumption is important because the crystal sensitivity constant (C_f) decreases in a Gaussian-like fashion from the center of the crystal and becomes negligible at the edge of the electrode.[19]

Within the Sauerbrey regime, a quartz oscillator will exhibit harmonic motion similar to a pendulum or spring but with fewer losses in energy. These losses can be expressed in terms of a quality factor, Q, which is a measure of the ratio of peak energy stored to energy lost per cycle of the oscillation. The higher the value of Q, the less loss is occurring in the system. The Q factor can be calculated using Equation 2.2:

$$Q = \frac{1}{R_m}\sqrt{\frac{L_m}{C_m}} \quad (2.2)$$

where the quartz resonator is described by using an equivalent circuit representation (Chart 2.2).[19] The series, or motional, branch of the circuit consists of one each of inductive, capacitive, and resistive components linked in a series. The inductor, L_m, is related to the displaced mass during the oscillation. The capacitor, C_m, represents the energy stored during the oscillation. The resistor, R_m, represents the energy dissipation during the oscillation; changes in this component are attributable to internal friction, mechanical losses to the surrounding system, and acoustic losses to the environment. A capacitor in parallel with the motional branch, C_0, represents the static capacitance of the system.

Impedance analysis using a standard network analyzer allows numerical values to be determined for changes in the oscillation of a circuit due to changes in mass or

Chart 2.2. Equivalent circuit representation of a traditional quartz oscillator.

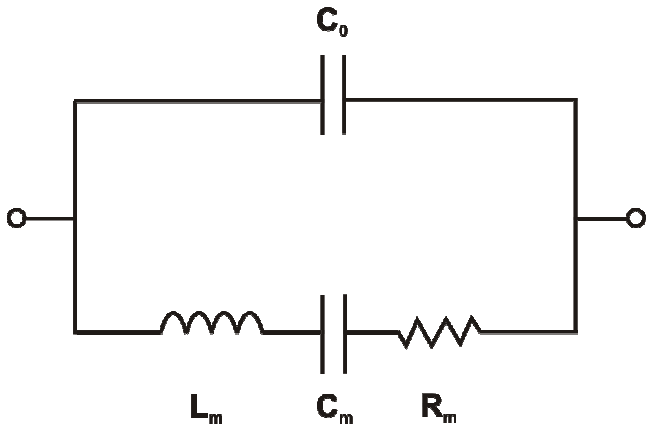

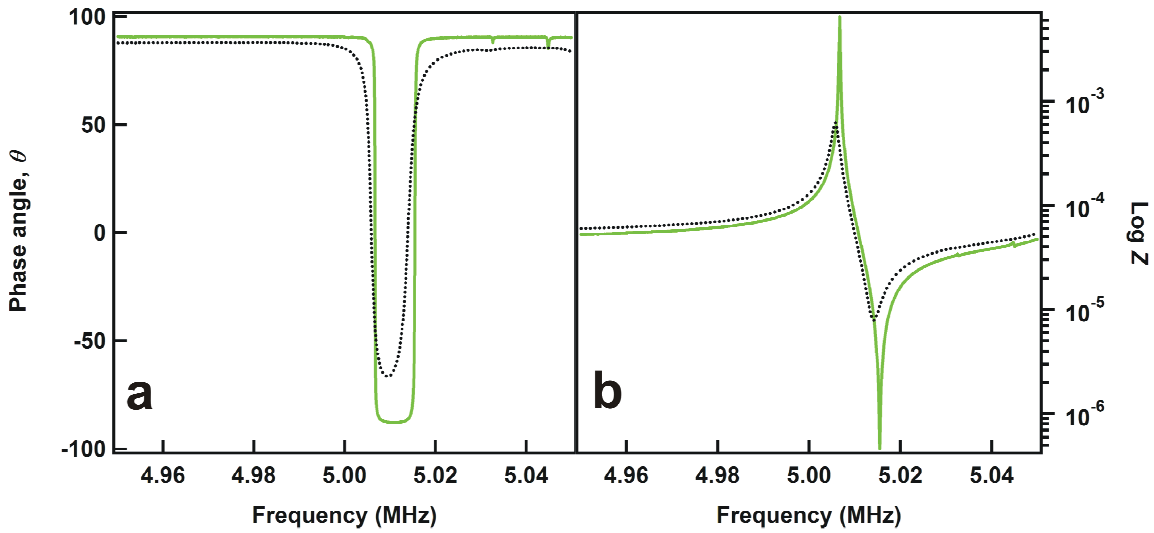

Figure 2.5. Plots of (a) θ (phase angle), and (b) Log Z (impedance) response of a clean quartz crystal in air (solid green line) and in water (dotted black line). The quality factor, Q, for the crystal in air was 31 484; Q for the crystal in water was 3 631.

viscoelasticity in the system. For a clean crystal in air $f_0 = f_r$, where the impedance reaches its minimum and the corresponding phase angle, θ, is 0. Changes in either the mass of the crystal or coupling of the crystal with a liquid will shift the value of f_r from f_0. Using the Sauerbrey equation (2.1), this Δf value can be converted to the numerical change in mass. However, for a complex system, such as a water-swollen polymer adsorbed to the electrode surface, changes in the viscoelasticity can convolute these changes, and so the films' density, viscosity, and elasticity must be reevaluated.[19,23] Nevertheless, if one assumes that the film behavior falls outside the linear mass-frequency relationship established by the Sauerbrey equation (2.1), the changes in

frequency can be qualitatively used to explain a film's morphological behavior, especially in conjunction with changes in the resistivity of the film (Chapter 4).

QCM measurements were made using a QCM200 system from Stanford Research Systems (Sunnyvale, CA).[24] This instrument allows for isolation of the motional resistance (R_m) and the resonant frequency (f_r) signals in real-time; the QCM200 system incorporates a method of C_0 capacitance nullification to allow for the measurement of the true values of R_m and f_r. The measurement of R_m is critical in the study of polymer films by QCM, as it is a direct measure of the acoustic damping of the polymer film. In other words, if the polymer film's acoustic impedance is significantly different from that of the quartz crystal, the film can act to dampen oscillation of the crystal. In some cases, this dampening can cause the frequency response of the QCM to be non-linear with respect to added mass, thereby rendering the QCM resonant frequency measurement relatively useless by itself.[19,25-27] The equivalent circuit for this instrument is shown in Chart 2.3.[24,28] This system requires that the static capacitance (C_0) be nulled with respect to both the motional capacitance (C_m) and motional inductance (L_m) every time the solution environment is changed. The QCM200 system is driven by an automatic gain control amplifier and terminated into a load resistor (R_L). The AGC amplifier is used to oscillate the circuit at a frequency where the phase shift will equal 0°. If C_0 is ignored, it will inject a leading current into the R_L to force the R_m to cancel the effect with a lagging current through the motional arm of the circuit, thereby keeping the phase shift equal to 0°. If C_0 is not nulled, the result is that the reactance of C_m and L_m is inductive and cannot be ignored. Further, if the R_m is large and cannot contribute a lagging current that is high

Chart 2.3. Equivalent circuit representation of the quartz oscillator as designed by SRS.[24]

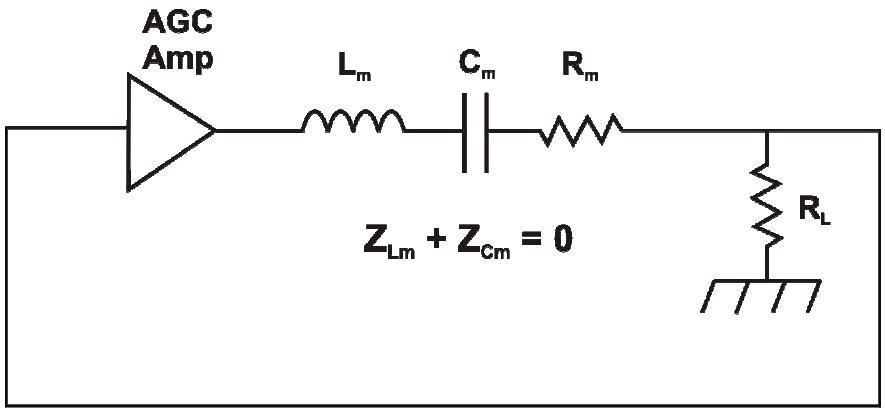

enough, then the circuit may cease oscillating. A varactor, C_v, is therefore used to cancel C_0. C_v is set equal to C_0 by finding the bias setting that minimizes the gain required to sustain oscillation.[24]

2.2.3 Experimental

Full impedance analysis of microgel films was first performed using a Hewlett-Packard E5100A Network Analyzer and 1-cm ~5 MHz quartz crystals with Au/Ti electrodes. Representative data for measurements performed by this method are shown in Figure 2.5. When used to analyze films, the resistance data obtained using this instrumentation gave an indication that the behavior of these films might be of interest (Figure 2.6), but the results were not reproducible. Further, though these resistance data were unusal, the other parameters of the film did not change in scale in the same fashion.

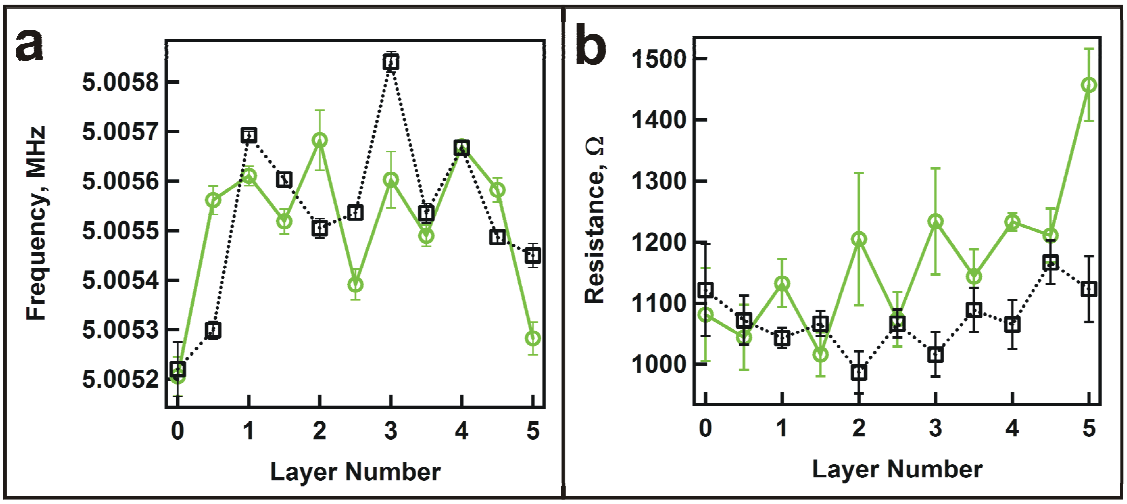

Figure 2.6. Data from the full impedance analysis experiments. Graphs show (a) frequency and (b) resistance for films. The solid, green line represents the film in pH 3.0 buffer and the black, dotted lines represent the films in pH 6.5 buffer.

Instability of the measurements was probably due to problems with the mounting system designed to couple the crystal with the network analyzer.

For the studies contained in Chapter 4, 1-inch ~5 MHz AT-cut quartz crystals with a "wrap-around" electrode configuration[24] were used. The exposed electrode area is ~1.37 cm^2 but the active oscillation is mostly restricted to the areas of overlap between the two circular pad electrodes (~0.40 cm^2).[24] This restriction gives an area mass sensitivity of 0.18 ng/cm^2, as calculated using the Sauerbrey equation (equation 2.3)[19,24],

$$\Delta f = -C_f \cdot \Delta m \tag{2.3}$$

where Δf is the measured frequency shift in Hz, C_f is the sensitivity factor for the quartz crystal (56.6 Hz $\mu g^{-1} cm^2$ for a 5 MHz crystal at room temperature), and Δm is the mass change due to deposited material per unit area.

Capacitance nullification was performed every time a new medium was exposed to the surface of the crystal. A short experiment was performed to test the effect of capacitance nullification (Figure 2.7). Briefly, this experiment used a 6.5 bilayer film (as constructed in Chapter 4). The film on the crystal was first exposed to a pH 3.0 buffer solution and the capacitance was nulled. Next, a pH 6.5 buffer was introduced into the flow cell, but the capacitance was not nulled. After several minutes, the capacitance was nulled. After several more minutes, the solution was changed back to pH 3.0 buffer and the capacitance was not nulled. After several minutes the capacitance was nulled; the experiment was terminated several minutes later. It is clear from the data that failing to

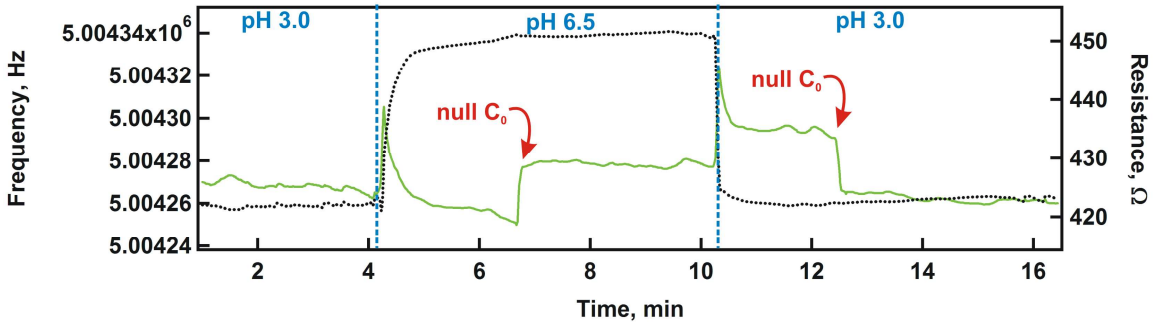

Figure 2.7. Plots of the data for the nulling experiment. The film under study was a 6.5 bilayer film constructed with pNIPAm-*co*-AAc negatively-charged microgels and 70 000 MW PAH as the polycation. The solid, green line represents the frequency data, the dotted black line represents the resistance data. Vertical dashed-blue lines demarcate when the medium surrounding the film was changed.

null the capacitance impacts the frequency response of the film. It does not appear to have as much impact on the resistance response, however.

Typical data from the QCM method are presented in Figure 2.8. This figure shows that in air, the crystal with the microgel film oscillates at a given frequency. When fluid is allowed to flow over the crystal, the frequency changes accordingly. If the pH of the fluid is changed, the pH-sensitive microgels on the electrode respond and the frequency and resistance change again. A detailed description and interpretation of film behavior by QCM is found in Chapter 4.

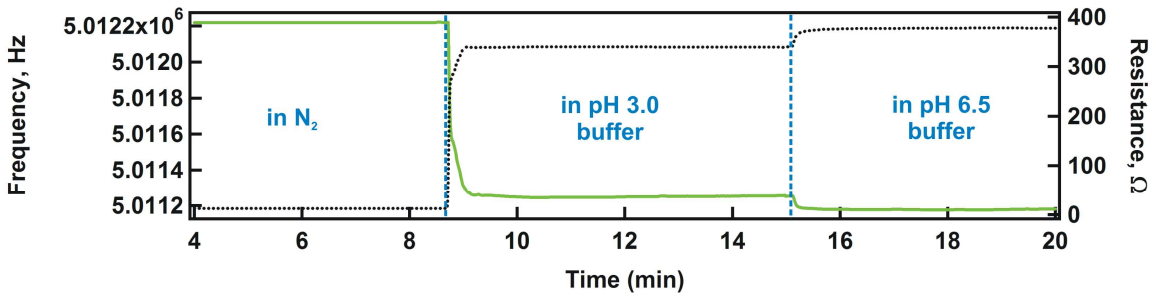

Figure 2.8. Plots of representative QCM data using the SRS QCM200. The data show the pH response of a 1.5 bilayer film. The solid, green line represents the frequency data, the dotted black line represents the resistance data. Vertical dashed –blue lines demarcate when the medium surrounding the film was changed. This response is reversible (not shown).

2.3 Surface Plasmon Resonance

2.3.1 Introduction

Surface Plasmon resonance (SPR) is complimentary to QCM because it measures changes in film thickness and morphology by using light as opposed to sound. Superficially, QCM provides a relatively simple set of data based on well-established principles and assumptions given by the Sauerbrey equation (Equation 2.1). Changes in the response of the QCM can be interpreted easily as variations in mass, film thickness, or film viscoelasticity. In contrast, SPR responses are most easily interpreted as changes in optical density or thickness, but quantification of SPR data requires quite a bit more modeling to directly interpret the data as changes in mass or finite thickness. The penetration depth of QCM is much larger than the penetration depth for SPR; even though SPR will continue to give information about changes in the bulk of films thicker than ~200 nm, QCM can still give information about the films' surface. By using the two techniques in conjunction, an easily interpretable set of data can give a full picture of film morphology as it relates to changes in thickness or viscoelasticity. SPR has been used and developed by many scientists who want sensitive techniques for biosensing[29,30] and polymer characterization.[31] Significant amounts of research have also gone into enhancement of surface plasmon resonance for sensing applications via use of metal nanoparticles, which also exhibit surface plasmon absorbances.[32-36]

2.3.2 Theory

Surface plasmon resonance spectroscopy[37,38] takes advantage of the coupling between electrons oscillating on a metal surface and a dielectric coupled to the metal surface.

These oscillating electrons are non-radiative surface plasmons, meaning that they describe fluctuations of surface electron density.[38] The plasmon is strongest at the metal/dielectric interface and decays exponentially and perpendicularly into the dielectric to a depth of ~100-200 nm. Generally, gold is used as the metal, and aqueous solutions are used for the dielectric, though the dielectric can be any substance coupled to the gold surface. For the studies in this thesis the dielectric will be microgel films. For SPR to be sensitive, the metal must be thin enough to allow for the penetration of the evanescent field. For gold, the optimum metal thickness is 45-50 nm.[34] The metal film is normally supported on a glass substrate which is coupled to a prism through which a light source in introduced to excite the plasmons. Surface plasmons cannot be directly excited by light, so they are instead excited by evanescent waves generated at the glass/metal interface via total internal reflection (TIR) of light through the prism (Scheme 2.3). The angle of incidence, θ_{sp}, can be determined by the equation,

$$\theta_{sp} = \sin^{-1}\left(\frac{k_{sp}}{n_g \cdot k_0}\right) \qquad (2.4)^{37}$$

where k_{sp} is the surface plasmon wave vector, k_0 is the wave vector of light in a vacuum (given by $k_0 = 2\pi/\lambda$, where λ is the wavelength of incident light in a vacuum) and n_g is the refractive index of the prism.[37] At this angle, a sharp decrease in the reflectance of the incident light beam occurs due to loss of energy to the evanescent waves. The evanescent wave penetrates the metal and excites the plasmon mode at the metal/dielectric interface. The angle, θ_{sp}, is sensitive to changes in the dielectric on the far side of the metal film

and will cause changes in the angular dependence of the reflection. For polymer films (Scheme 2.3), Equation 2.4 can be converted to:

$$\Delta\theta_{sp} = \frac{\Delta k_{sp}^{p}}{n_g k_o \cos\theta_{sp}} \qquad (2.5)^{37}$$

This equation indicates that the change in the plasmon angle can be related linearly to changes in polymer (or adsorbed layer) thickness through the term Δk_{sp}^{p}, which is

Scheme 2.3. Diagram of an SPR device for the study of polymer films.

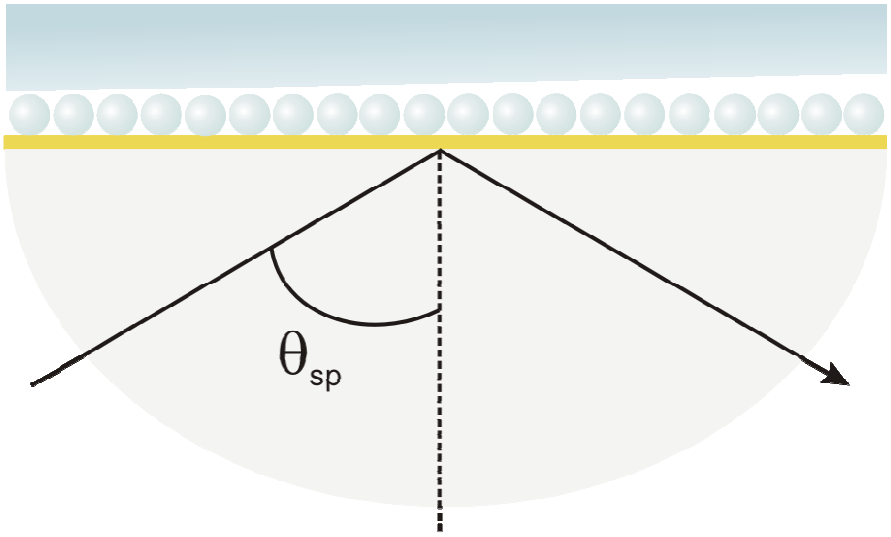

proportional to d_p, or the polymer layer thickness.[37] The sensitivity to changes in the thickness of a polymer film (d_p) is limited by the difference between the dielectric constant of the film and the dielectric constant of the surrounding solution. The dielectric constants of the measured media can be converted to refractive index (by Maxwell's relationship, $n = \sqrt{\varepsilon}$); thus, sensitivity to changes in the dielectric constant of the medium at the metal interface can be considered proportional to the changes in the optical density of the films.

SPR is generally performed using *p*-polarized, monochromatic light and the technique measures the response of reflected light over a range of many angles. However, a more facile approach to SPR involves the use of an incoherent, white light source at a fixed angle.[30,39-41] The same general principles apply, but one instead sees a change in the wavelength associated with the reflected light due to changes in the coupling of the evanescent wave with the dielectric on the far side of the metal film. While the traditional angular dependent measurements are more sensitive, and thus more useful for biological systems, especially when coupled with nanoparticle sensing,[32-34,42] the incoherent light technique is sensitive enough for study of changes in polymer films presented herein, and it makes use of more readily available, less expensive components.

2.3.3 Experimental

The SPR instrument used for the investigations contained herein was designed and built by this researcher from optical elements available commercially. A photograph of the instrument is shown in Figure 2.9. This instrument was equipped with a fiber-coupled white light source and a fiber-coupled photodiode array detector (Ocean Optics) for illumination and detection, respectively. Sample excitation and detection angles were

controlled by using a Newport Corp. motion controller (MM 3000) and rotation stages (495 CC) with 0.01° resolution. A program built in LabView was used to send commands to the motion controller, which adjusted the two motion stages to achieve the desired collection angle.

The optical elements of the instrument were arranged thus: the fiber-coupled white light source was set close to the prism to ensure that it was still collimated when it reached the air/prism interface at the incident angle. The light traveled through the prism and reflected off the gold film. When the reflected beam passed out of the prism, it was passed through a hemicylindrical lens to recollimate the light. The light then passed through a Glan Thompson polarizer to ensure that the measured response was given by *p*-polarized light. The light subsequently passed through a lens and aperture to focus as much of the light into the detector as possible. The focusing lens and aperture were adjusted as needed to optimize the measured response.

To perform SPR experiments, a 50-nm thick layer of gold was evaporated onto 3-mercaptopropyltrimethoxysilane (MPTMS)-functionalized glass cover slips by using a Denton Vacuum DV-502A thermal metal evaporator. MPTMS was attached to the substrates by exposing Ar plasma (Harrick Scientific plasma cleaner) cleaned glass to a 1% (v/v) ethanolic (200 proof ethanol) MPTMS solution for 2 h. This monolayer functions as a molecular adhesion layer, thus improving the binding of Au to the glass substrate without the need for Cr or Ti underlayers. To obtain SPR spectra, the uncoated side of the glass substrate was optically coupled to the bottom of a hemispherical prism using a drop of immersion oil and mounted onto a custom-made flow cell. White light

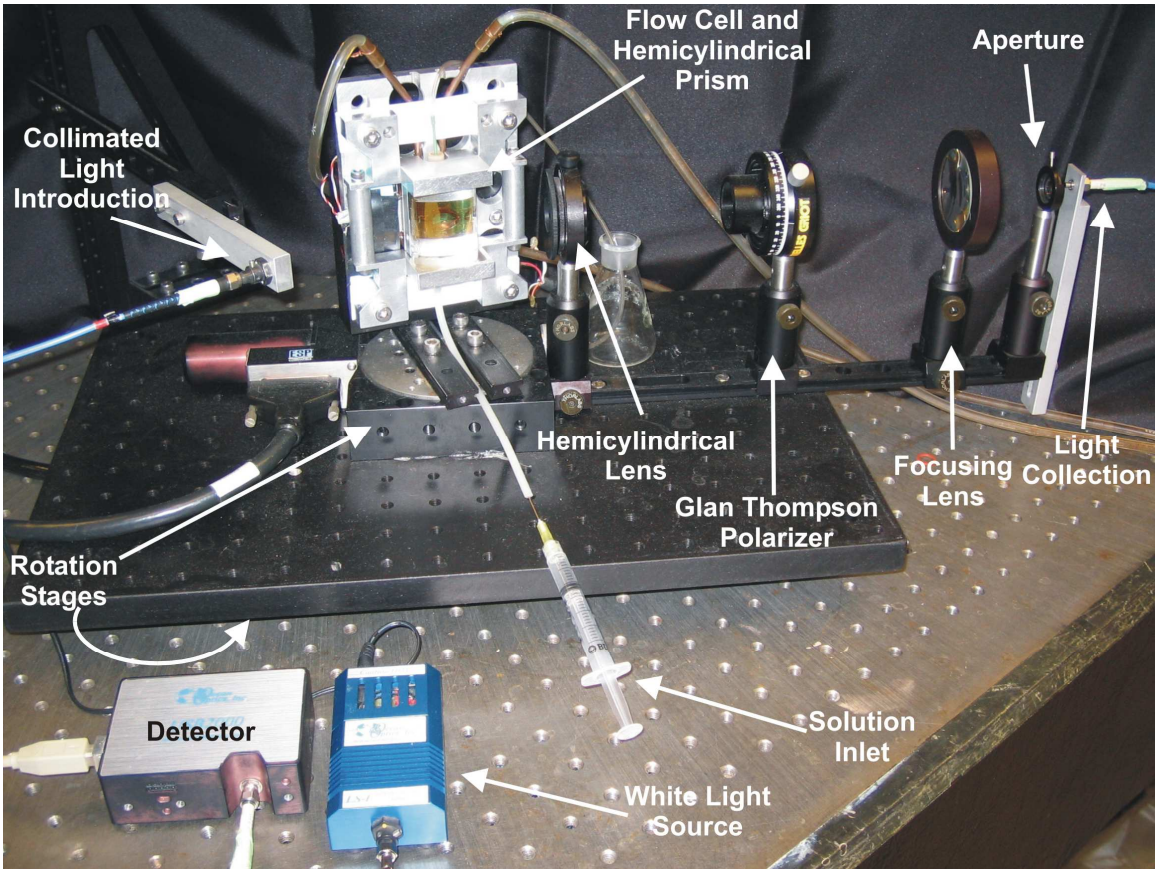

Figure 2.9. Photograph of the SPR instrument. Out of the range of this picture are the controller for the rotation stages and the computer used to drive the controller and collect the data.

was then introduced into the sample at an incident angle of 73°,[43] and the beam reflected from the sample was monitored as a function of wavelength.

The instrument used in these investigations produced the data as shown in Figure 2.10. By coupling a microgel film built on a gold-coated cover slip to a hemispherical prism, the instrument response can be measured as the pH of the surrounding solution is changed. The data show that when the pH is increased from pH 3.0 to pH 6.5, an

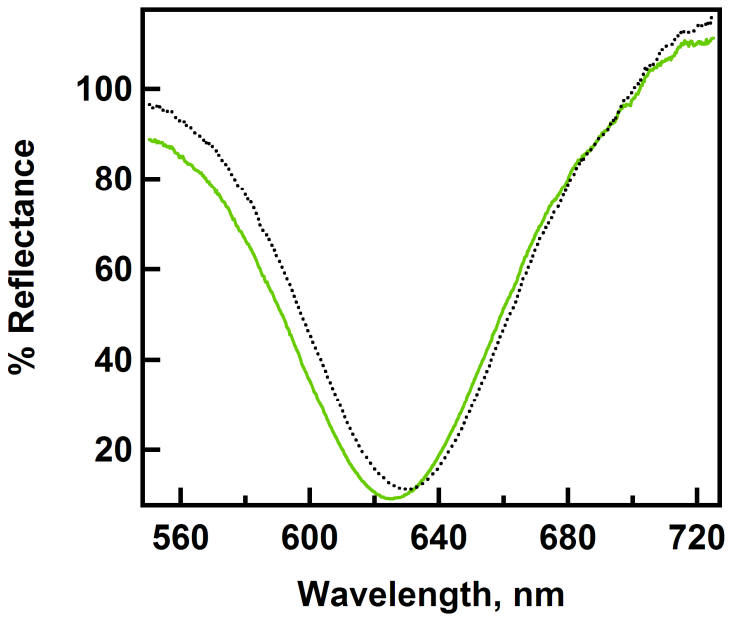

Figure 2.10. Representative surface plasmon resonance data of a 3 bilayer film in pH 3.0 buffer (green line) and pH 6.5 buffer (dotted black line). The associated wavelengths for the plasmon response are 625 nm and 630 nm at pH 3.0 and pH 6.5, respectively.

increase in the wavelength (red shift) is observed. Concomitantly, a small change in the reflectance is also observed. These data can be interpreted as evidence for an increase in the optical density of the microgel film by a simple change in the pH of the solution surrounding the film. A detailed account of its meaning with regard to microgel film morphology is given in Chapter 4.[44]

2.4 Conclusions

Used individually or in combination, the techniques of atomic force microscopy, quartz crystal microbalance, and surface plasmon resonance spectroscopy give detailed information about polymer films. For the research presented herein each was used according to the needs of the project.

References

1. Foster, A.; Hofer, W., *Scanning Probe Microscopy: Atomic Scale Engineering by Forces and Currents*. Springer: 2007.

2. Tsukruk, V. V., "Scanning probe microscopy of polymer surfaces." *Rubber Chem. Technol.* **1997,** 70, 430-467.

3. Butt, H. J.; Cappella, B.; Kappl, M., "Force measurements with the atomic force microscope: Technique, interpretation and applications." *Surf. Sci. Rep.* **2005,** 59, 1-152.

4. Garcia, R.; Perez, R., "Dynamic atomic force microscopy methods." *Surf. Sci. Rep.* **2002,** 47, 197-301.

5. Mermut, O.; Lefebvre, J.; Gray, D. G.; Barrett, C. J., "Structural and mechanical properties of polyelectrolyte multilayer films studied by AFM." *Macromolecules* **2003,** 36, 8819-8824.

6. Lowman, G. M.; Tokuhisa, H.; Lutkenhaus, J. L.; Hammond, P. T., "Novel Solid-State Polymer Electrolyte Consisting of a Porous Layer-by-Layer Polyelectrolyte Thin Film and Oligoethylene Glycol." *Langmuir* **2004,** 20, 9791-9795.

7. Johnson, C. A.; Lenhoff, A. M., "Adsorption of Charged Latex Particles on Mica Studied by Atomic Force Microscopy." *J. Colloid Interface Sci.* **1996,** 179, 587-599.

8. Bright, R. M.; Musick, M. D.; Natan, M. J., "Preparation and Characterization of Ag Colloid Monolayers." *Langmuir* **1998,** 14, 5695-5701.

9. FitzGerald, P. A.; Dupin, D.; Armes, S. P.; Wanless, E. J., "In situ observations of adsorbed microgel particles." *Soft Matter* **2007,** 3, 580-586.

10. Sorrell, C. D.; Lyon, L. A., "Deformation Controlled Assembly of Binary Microgel Thin Films." *Langmuir* **2008**, In press.

11. Coffey, D. C.; Reid, O. G.; Rodovsky, D. B.; Bartholomew, G. P.; Ginger, D. S., "Mapping local photocurrents in polymer/fullerene solar cells with photoconductive atomic force microscopy." *Nano Lett.* **2007,** 7, 738-744.

12. Coffey, D. C.; Ginger, D. S., "Time-resolved electrostatic force microscopy of polymer solar cells." *Nat. Mater.* **2006,** 5, 735-740.

13. Coffey, D. C.; Ginger, D. S., "Patterning phase separation in polymer films with dip-pen nanolithography." *J. Am. Chem. Soc.* **2005,** 127, 4564-4565.

14. Nonnenmacher, M.; Oboyle, M. P.; Wickramasinghe, H. K., "Kelvin Probe Force Microscopy." *Appl. Phys. Lett.* **1991,** 58, 2921-2923.

15. Jacobs, H. O.; Knapp, H. F.; Muller, S.; Stemmer, A., "Surface potential mapping: A qualitative material contrast in SPM." *Ultramicroscopy* **1997,** 69, 39-49.

16. Hohlbauch, S.; Cavazos, H.; Proksch, R., In *iDrive: Theory, Applications, Installation and Operation*, AR, Ed. 2007.

17. Buguin, A.; DuRoure, O.; Silberzan, P., "Active atomic force microscopy cantilevers for imaging in liquids." *Appl. Phys. Lett.* **2001,** 78, 2982-2984.

18. Jones, K., In *Kelvin Probe Force Microscopy*, AR, Ed. 2007.

19. Buttry, D. A.; Ward, M. D., "Measurement of Interfacial Processes at Electrode Surfaces with the Electrochemical Quartz Crystal Microbalance." *Chem. Rev.* **1992,** 92, 1355-1379.

20. Lasky, S. J.; Buttry, D. A., "Detection of Glucose Using Hexokinase." *ACS Symposium Series: Sensors Based on Biomolecules Immobilized on the Piezoelectric Quartz Crystal Microbalance* **1989,** 403, 237-246.

21. Kanazawa, K. K., "Mechanical behaviour of films on the quartz microbalance." *Faraday Discuss.* **1997,** 107, 77-90.

22. Muramatsu, H.; Kim, J. M.; Chang, S. M., "Quartz-crystal sensors for biosensing and chemical analysis." *Anal. Bioanal.Chem.* **2002,** 372, 314-321.

23. White, C. C.; Schrag, J. L., "Theoretical predictions for the mechanical response of a model quartz crystal microbalance to two viscoelastic media: A thin sample layer and surrounding bath medium." *J. Chem. Phys.* **1999,** 111, 11192-11206.

24. SRS, In *Operation and Service Manual: QCM200 Quartz Crystal Microbalance Digital Controller and QCM25 5 MHz Crystal Oscillator (Revision 2.1 (6/2005))*, 2004.

25. Ward, M. D.; Buttry, D. A., "In Situ Interfacial Mass Detection with Piezoelectric Transducers." *Science* **1990,** 249, 1000-1007.

26. Kanazawa, K. K.; Melroy, O. R., "The Quartz Resonator: Electrochemical Applications." *IBM J. Res. Develop.* **1993,** 37, 157-171.

27. Kipling, A. L.; Thompson, M., "Network Analysis Method Applied to Liquid-Phase Acoustic Wave Sensors." *Anal. Chem.* **1990,** 62, 1514-1519.

28. Arnau, A.; Sogorb, T.; Jiménez, Y., "Circuit for continuous motional series resonant frequency and motional resistance monitoring of quartz crystal resonators by parallel capacitance compensation." *Rev. Sci. Instrum.* **2002,** 73, 2724-2737.

29. Lee, H. J.; Goodrich, T. T.; Corn, R. M., "SPR Imaging Measurements of 1-D and 2-D DNA Microarrays Created From Microfluidic Channels on Gold Thin Films." *Anal. Chem.* **2001,** 73, 5525-5531.

30. Piehler, J.; Brecht, A.; Geckeler, K. E.; Gauglitz, G., "Surface modification for direct immunoprobes." *Biosens. Bioelectron.* **1996,** 11, 579-590.

31. Harmon, M. E.; Jakob, T. A. M.; Knoll, W.; Frank, C. W., "A Surface Plasmon Resonance Study of Volume Phase Transitions in N-Isopropylacrylamide Gel Films." *Macromolecules* **2002,** 35, 5999-6004.

32. Lyon, L. A.; Pena, D. J.; Natan, M. J., "Surface Plasmon Resonance of Au Colloid-Modified Au Films: Particle Size Dependence." *J. Phys. Chem. B* **1999,** 103, 5826-5831.

33. Lyon, L. A.; Holliway, W. D.; Natan, M. J., "An improved surface plasmon resonance imaging apparatus." *Rev. Sci. Instrum.* **1999,** 70, 2076-2081.

34. Natan, M. J.; Lyon, L. A., "Surface Plasmon Resonance Biosensing with Colloidal Au Amplification." *Metal Nanoparticles: Synthesis Characterization, and Applications* **2001**, 183-205.

35. Jain, P. K.; El-Sayed, M. A., "Surface plasmon coupling and its universal size scaling in metal nanostructures of complex geometry: Elongated particle pairs and nanosphere trimers." *J. Phys. Chem. C* **2008,** 112, 4954-4960.

36. Jain, P. K.; Huang, X.; El-Sayed, I. H.; El-Sayad, M. A., "Review of some interesting surface plasmon resonance-enhanced properties of noble metal nanoparticles and their applications to biosystems." *Plasmonics* **2007,** 2, 107-118.

37. Garland, P. B., "Optical evanescent wave methods for the study of biomolecular interactions." *Q. Rev. Biophys.* **1996,** 29, 91-117.

38. Raether, H., *Surface Plasmons on Smooth and Rough Surfaces and on Gratings*. Springer-Verlag: Berlin, 1988; p 136.

39. Lyon, L. A.; Musick, M. D.; Natan, M. J., "Colloidal Au-Enhanced Surface Plasmon Resonance Immunosensing." *Anal. Chem.* **1998,** 70, 5177-5183.

40. Serpe, M. J.; Lyon, L. A., "Optical and Acoustic Studies of pH-Dependent Swelling in Microgel Thin Films." *Chem. Mater.* **2004,** 16, 4373-4380.

41. Sorrell, C. D.; Lyon, L. A., "Bimodal Swelling Responses in Microgel Thin Films." *J. Phys. Chem. B* **2007,** 111, 4060-4066.

CHAPTER 3

MICROGEL SYNTHESIS AND CHARACTERIZATION

A bottom-up approach to thin film construction is employed to design a film that responds to a stimulus based on a small change in the microgel morphology. Because microgels are endlessly modifiable, these studies use a variety of microgels to study the structure-property relationships of microgel thin films. The details of particle synthesis and their characterization are described.

3.1 Microgel Synthesis

3.1.1 Introduction

Poly(*N*-isopropylacrylamide) (pNIPAm) is an environmentally sensitive polymer that undergoes an entropically-driven phase transition at a lower critical solution temperature (LCST) of ~31 °C in water.[1,2] Thermoresponsive polymers like pNIPAm are often called "smart" materials because they maintain their shapes after a phase transition.[1,2] At temperatures below the LCST, a hydrogel is solvent swollen, so solvent-chain interactions dominate; above the LCST the material deswells by expelling the solvent, so chain-chain interactions dominate.

For pNIPAm, a phase transition occurs because of changes in the hydrogen bonds between the solvent (i.e., water) and the amide groups in the polymer chains. At

Scheme 3.1. Environmentally responsive hydrogels.

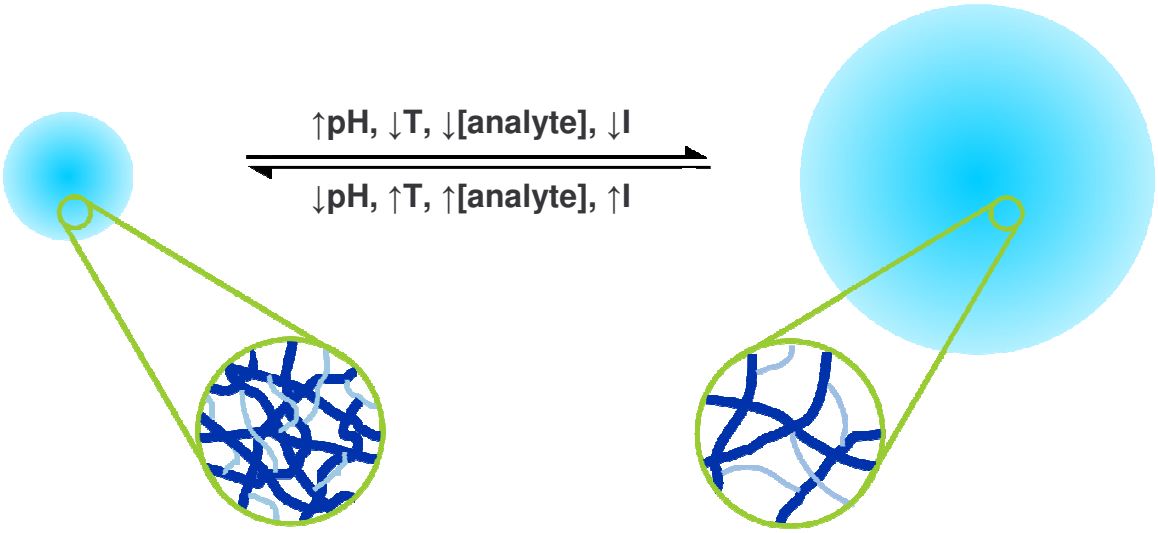

temperatures below the LCST, water molecules form hydrogen bonds with the amide groups of pNIPAm. Within the polymer, other water molecules form ordered clathrate-like structures around the nonpolar isopropyl moieties, which cannot form hydrogen bonds.[1-3] Clathrates are structures whereby one type of molecule forms an ordered crystalline structure to trap another molecule. The most commonly known types of these structures are found on the ocean floor where high pressure and low temperature create water crystals that trap molecules of methane. Thus, the clathrate-like formation of water around pNIPAm at low temperatures is a stable, ice-like structure within the confinement of the microgel system. At higher temperature these clathrate-like structures are unstable and they break apart, which allows hydrophobic interactions between isopropyl groups

Scheme 3.2. Configuration of pNIPAm in water.

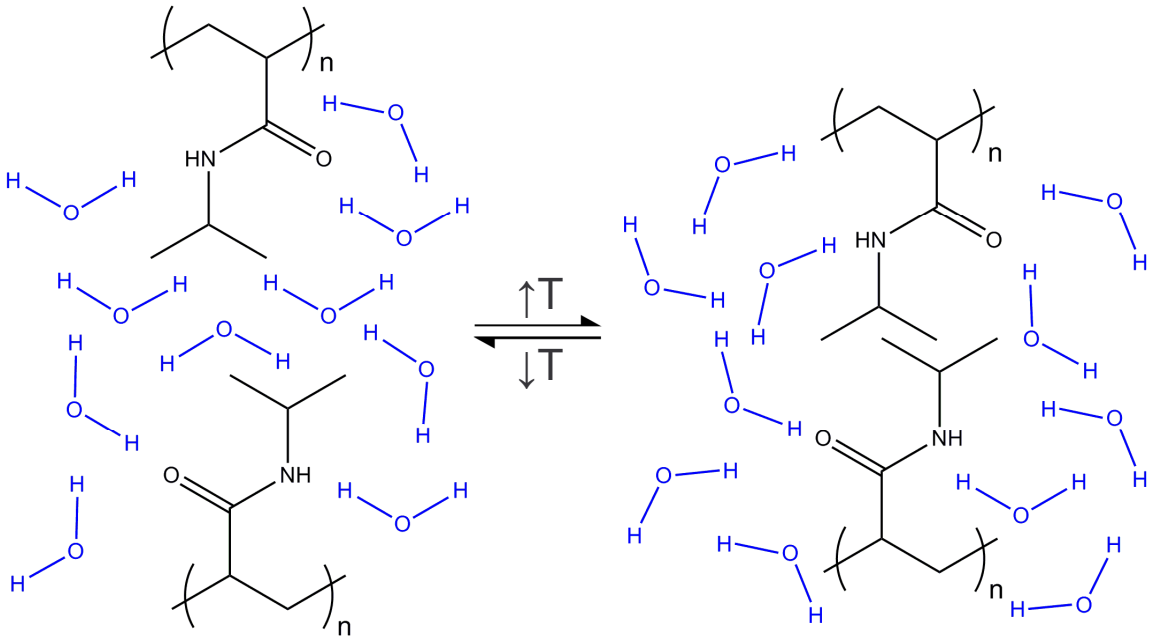

to dominate. If one considers the hydrogel in terms of the standard Gibb's free energy equation (3.1),

$$\Delta G^\circ = \Delta H^\circ - T\Delta S^\circ \tag{3.1}$$

each term contributes to ΔG° (standard Gibb's free energy) of the phase transition reaction as the temperature (T) increases. At temperatures below the LCST of the polymer, the ΔG° term is positive for the deswelling phase transition and the hydrogels are in a swollen state. The swollen state is due to the large positive contribution of enthalpy and the relatively low disorder in the system at the lower temperature. At this low temperature (T < LCST of the polymer), water spontaneously forms into clathrate-

like structures within the gel and remains stable.[1,2,4] As the temperature increases, the heat supplied to the system breaks the hydrogen bonds between the water and the polymer, which breaks up the clathrate structures. As a result, $\Delta H°$ for the transition is positive because the reaction is endothermic. The disorder in the system increases as the microgels begin to deswell due to loss of water and the formation of hydrophobic associations between the polymer chains. This ensures that the entropy ($\Delta S°$) for the phase transition is positive since the swollen state is not the most favorable conformation in solution at the elevated temperature. At the LCST, the higher temperature allows the $-T\Delta S°$ term to counter the positive $\Delta H°$ term for the deswelling reaction such that the value of $\Delta G°$ becomes essentially zero. As the temperature increases above the LCST, the temperature continues to increase resulting in a negative $\Delta G°$ such that the deswollen product is stable at the elevated temperature.[5]

The phase separation described above for pNIPAm at high temperatures is the reason that microgels can be synthesized as monodispersed, colloidally-stable, micron-sized hydrogels. The mechanism for the synthesis of microgels is a radical-initiated precipitation polymerization reaction that is carried out at a temperature above the LCST (Scheme 3.3). Because of the entropically-favored deswollen conformation of the polymer at these high temperatures, the growing polymer chains, which are oligoradicals, will collapse to form precursor particles. In the presence of a cross-linker, these nucleation sites will join with other oligoradicals and precursors to form particles that will grow until the monomer feed solution is exhausted, ultimately generating a microgel. When the reaction solution is cooled to room temperature, the microgels remain intact

Scheme 3.3. Schematic representation of microgel synthesis.

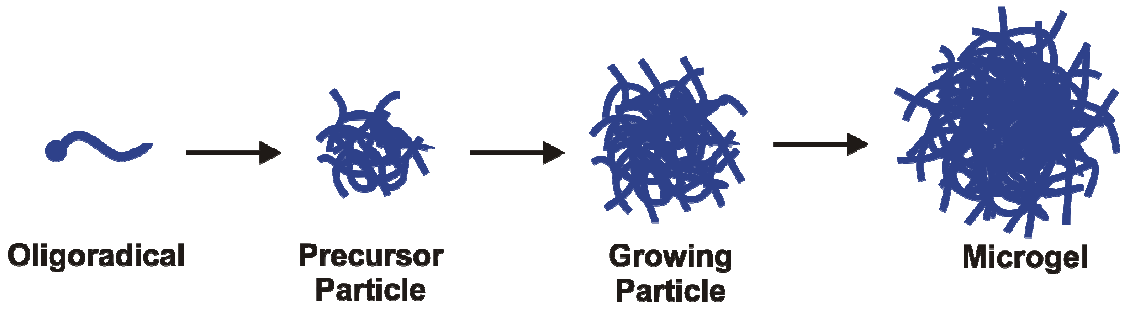

due to the presence of a cross-linker; these microgels have properties similar to those of a bulk hydrogel.

The use of a "seed-and-feed" synthesis scheme has been employed by several researchers to create a core/shell microgel.[6-13] For these syntheses, microgels are added to a fresh monomer feed solution and the reaction mixture is heated above the LCST of the microgels (Scheme 3.4). Like the general microgel synthesis, the collapsed particles act as nucleation sites for the synthesis of the growing oligoradicals, which will collapse onto the microgels to form a shell. Because the shell forms on a collapsed particle, the shell will sometimes compress the microgel core and the final size of the particle will actually be smaller than the core itself even though mass has been added to the core. The amount of monomer used will dictate how thick the shell is; the amount of cross-linker will dictate how easily the core reswells after the shell is added.[6] The addition of a shell to a microgel core boosts the ability to add functionality to the microgel surface without changing the microgel itself; the overall responsivity of the particle will be largely based on the properties of the core.

Scheme 3.4. Schematic representation of "seed-and-feed" core/shell microgel synthesis.

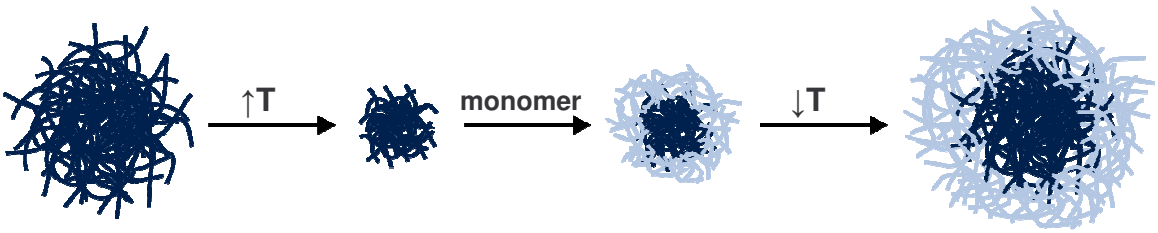

Addition of other monomers can also add functionality to the particles. To add a charged or hydrophilic group to the particles, or within the shell of a core/shell microgel itself, the use of a co-monomer is often employed. Acrylic acid (AAc) as a co- monomer gives the particle a negative charge in solutions having a pH greater than the pK_a value of the acid (4.2 for AAc). When the particles are in solution with a pH value less than 4.2, the acid groups are protonated and neutral. When the pH is raised above a value of 4.2, the acidic proton will be lost to the surrounding solution to give a particle with a net negative charge.

The particles swell as a result of Coulombic repulsions between the carboxylate groups. Thus, when these particles are in a solution with a pH value greater than 4.2, they do not undergo a phase change at the normal LCST because the carboxylate groups participate in Coulombic repulsions. The particles *will* eventually undergo a phase transition, but the LCST is shifted to a much higher temperature.

Acrylic acid also provides useful chemical handles for attaching additional functionality to the particle. For example, biotin or a fluorophore can be appended via a

carbodiimide coupling reaction. For these studies, the addition of an acidic *co*-monomer allows the particles to swell and deswell as a function of pH and renders them negatively charged for facile film fabrication on positively charged substrates.

A degradable cross-linker was employed for the studies described in Chapters 5 and 6. The cross-linker, *N,N'*-(dihydroxyethylene)bisacrylamide (DHEA), was employed because its 1,2-diol moiety is situated between the two acrylamide groups.[14] The carbon-carbon bond between the two alcohol groups can be cleaved by reaction with periodate ion (Scheme 3.5) during which the diol's carbinol groups are converted to formamide groups.[15] Using a core/shell construct where the core has only this degradable cross-linker can produce a hollow particle that could be used as a drug delivery device

Scheme 3.5. Reaction of the 1,2-diol group in the *N,N'*-(dihydroxyethylene)bisacrylamide (DHEA) cross-linker with sodium periodate.[15]

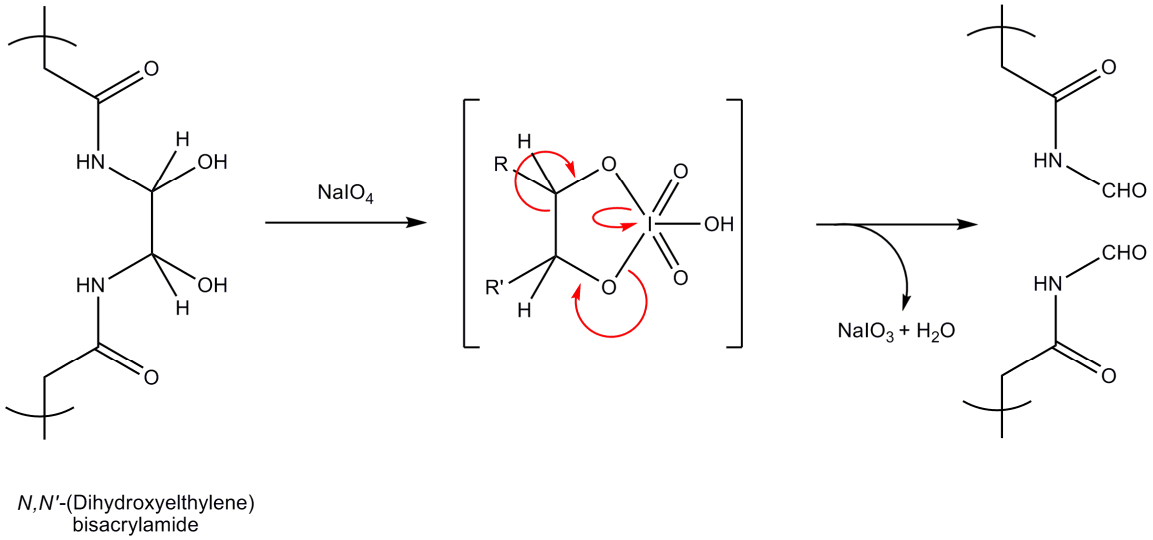

N,N'-(Dihydroxyelthylene) bisacrylamide

or nanoreactor. In a *co*-cross-linked system in which the cross-linker has been cleaved, these formamide groups can provide useful chemical handles for further functionalization of the microgel. But more importantly, the cleavage of the cross-linker in a *co*-cross-linked system can easily and significantly change the morphology of the microgel for use in thin film applications.

3.1.2 Methods

All microgel particles will be numbered separately in each chapter. The following naming convention will be used: core syntheses will be numbered consecutively by the type of synthesis performed and will appear in parentheses. For core/shell constructs, shell syntheses will also be numbered consecutively and that number will follow the core to which it was added (e.g. shell type **2** was added to core type **1** giving core/shell microgel product **(1)2**). Microgels were synthesized via aqueous free-radical precipitation polymerization as previously described.[12,16] Several types of microgels were synthesized for various purposes throughout this thesis. The exact amounts of the reagents are specified for each particle in the chapter in which the use of those particles appear. The general synthesis conditions are annotated here.

pNIPAm-based microgels. All microgels were synthesized using a total monomer concentration of 70 mM of NIPAm, co-monomer(s), and cross-linker(s). The ratios of NIPAm to cross-linker and co-monomer are specified in each chapter. In general, the NIPAm and cross-linker were dissolved in 99 mL of distilled, deionized water. The reaction mixture was transferred to a 250 mL three-necked round-bottomed flask equipped with a temperature probe, condenser, and nitrogen inlet. Nitrogen was bubbled

into the reaction solution while the mixture was heated to ~65-70 °C in a silicone oil bath. The temperature was regulated with a self-adjusting hotplate and temperature probe. Once the temperature stabilized, the nitrogen needle was pulled out of the mixture but the inlet was left in the flask to provide a blanket of nitrogen for the reaction. The initiator, generally 0.1 mmol APS, was dissolved separately in 1 mL of distilled, deionized water and added to the reaction mixture. If an acrylic acid *co*-monomer was used, it was added to the reaction mixture just before the initiator. After initiation, the polymerization was allowed to proceed for 4 hours at ~65-70 °C under a blanket of N_2.

"Seed-and-feed" core/shell microgels. To create a core/shell microgel, one of the core particles was selected for use in a seed-and-feed shell synthesis, as previously described.[9] Typically, ~40 mL of the reaction product suspension from above was diluted with ~59 mL of water. The shells were composed of 88% NIPAm, 2% BIS, and 10% AAc and were attached to the cores via aqueous free-radical precipitation polymerization as previously described,[9] using 40 mM total monomer concentration. To the microgel suspension were added the NIPAm and BIS monomers. The initiator, 0.1 mmol APS, was separately dissolved in 1 mL of distilled, deionized water. The reaction mixture was transferred into a 250 mL three-necked round-bottomed flask. Nitrogen was bubbled into the reaction while the mixture was heated to 65-70 °C. Once the temperature stabilized, the nitrogen needle was pulled out of the mixture but the inlet was left in the flask to provide a blanket of nitrogen for the reaction. The AAc was added to the reaction mixture followed by the APS solution, and the polymerization was allowed to proceed for 4 hours at 65-70 °C under a blanket of N_2.

Purification. All reactions were allowed to cool to room temperature and to stir overnight. Once cooled, the reactions were filtered via vacuum filtration through a #2 paper filter to remove any aggregated product. Aliquots of the resultant colloidal dispersions (~10 mL) were distributed into centrifuge tubes. The aliquots were purified by centrifugation using a relative centrifugal force (RCF) of 15 422 x *g* at 29 °C until a pellet was formed and the supernatant was no longer visibly turbid. The supernatant was removed and the pellet at the bottom of the tube was redispersed into water and vortexed. After 4-5 cycles of centrifugation and redispersion, the microgels were stored in a brown glass jar. If additional purification was required, the details are given in the chapter in which use of the particles is described.

3.2 Particle Characterization

To understand the characteristics of microstructured films and materials, one must first characterize the building blocks. Light scattering techniques represent one of the most powerful and informative ways to determine macromolecular mass and structure as well as other particle and polymer properties. It is also, incidentally, one of the few absolute methods for performing these measurements and is applicable over the broadest range of molecular weights.[17] Because of its sensitivity light scattering can resolve dimensions of an object to about $1/20^{th}$ of the incident wavelength. And when multi-angle static light scattering and size-exclusion chromatography are combined with refractometry, large polymer and heteropolymer molecular weights can be determined with ease.

3.2.1 Dynamic Light Scattering

All dynamic light scattering (DLS) data are presented in the chapters where of the particles is described. Dynamic light scattering has previously been used for determining mean particle size and particle size distributions,[18,19] and related microgel systems. The hydrodynamic radii (R_h) and diffusion coefficients (D) of the particles were determined by DLS (Protein Solutions, Inc.) prior to their use for thin-film fabrication. Briefly, a dilute microgel solution in buffer was added to a cuvette and inserted into the DLS cuvette holder, which is equipped with a Peltier device for sample temperature control. Laser light (783.9 nm) was introduced to the sample via a single-mode optical fiber, and scattered light was collected by a fiber-coupled avalanche photodiode detector at 90°. The random intensity fluctuations of the scattered radiation were used to calculate an autocorrelation decay, which could be related to the particle translational diffusion coefficient (Dynamics Software version 5.25.44). The average hydrodynamic radius was then calculated using the Stokes-Einstein equation. Some of the dynamic light scattering measurements for the particles described in Chapters 5 and 6 were performed using a DynaPro Plate Reader (Wyatt Technologies, Inc., Santa Barbara, CA). For each particle, the analysis was performed using samples made in ways similar to those made for DLS at 90°. The samples were individually-loaded into wells of a 384-well titer plate. Each sample was measured at a scattering angle of 158° using an incident laser light beam with a wavelength of 832.5 nm by taking 5 measurements consisting of 10 acquisitions each. The particle data were analyzed by using Dynamic software (version 6.9.2.9). Microgels were measured at 23 °C in the same buffers used for film assembly.

3.2.2 Static Light Scattering

The intensity of light scattered from the macromolecule depends on the polarizability of the molecule. The greater the polarizability, the more it will scatter light in all directions. The value *dn/dc* is a measure of polarizability. Macrolmolecules with sizes less than the wavelength of the incident light, can be considered as point scatterers because they will disperse the light with the same intensity in all directions. However, for macromolecules larger than the wavelength of the incident light, one must take into account the angles of the incident and scattered light as they will vary at different points on the molecule.[20] The size of a molecule can be determined by measuring the angular dependence of the scattered light intensity to yield a root mean square (rms) radius, which is a gauge of a particle's size based on its average weight around a center of mass. The rms radius often called the radius of gyration, R_g. Once the rms radius and the conformation of molecule are known (random coil, rod, etc.), the mass is also known. For an imperfectly monodispersed or polydispersed sample, the averaged rms radius, R_z, gives the best measure of the system as a whole, so the averaged molar mass, M_z, can be determined. When light scattering is combined with a separation technique such as asymmetric field flow fractionation (AFFF), the rms radius of each slice of data from a polydispersed sample can be established with ease.[17]

The determination of mass and radius by static light scattering is based on the theoretical foundation described by Bruno Zimm, which relates the scattering of light to the size of the molecule.[17] Zimm's theory states that in a monodispersed polymer system with volume, V, consisting of a concentration N of η segments, the probability of finding another within a distance r in a volume of $d\tau$ is

$$\eta N\rho(r)d\tau / V \tag{3.1}$$

The Rayleigh-Gans-Debye (RGD) approximation[17] states that when the impact of the particle on the incident beam is negligible, the excess Rayleigh ratio of the scattered light is related to the molecular weight of the molecule by

$$R_\theta = \frac{K^* \eta^2 N^2}{V^2} \int \rho(r) \exp(2\pi i s \frac{r}{\lambda d}) \tau \tag{3.2}$$

where θ is the angle between the incident and scattered rays, s is the vector difference between the unit vectors between the incident and scattered rays, and λ is the wavelength of the incident light in the solvent. The physical constant, K^*, is equal to $4\pi^2 (dn/dc)^2 n_0^2 / (N_a \lambda_0^4)$ where dn/dc is the refractive index increment of the solution (expressed in mL/g), n_0 is the refractive index of the solvent, and N_a is Avogadro's number. The concentration c (g/mL) is NM / VN_a where M is the molecular weight of the molecule. Thus, the measurement of size and molecular weight can be interpreted from the scattering ratio by[17]

$$\frac{R_\theta}{K^* c} = MP(\theta) - 2A_2 cM^2 P^2(\theta) \tag{3.3}$$

where A_2 is the second virial coefficient and $P(\theta)$ is the theoretically-derived form factor related to the radius gyration and is a function of the molecule's z-average size, shape, and structure. For particles larger than 100 nm in diameter, however, a Debye model is

often used to determine molecular weight and averaged radius from the data.[21] For this model, a polynomial is fit to the data to obtain the intercept and slope at zero angle. As the angle approaches zero, the form factor $P(\theta)$ approaches unity. The resulting equation is susceptible to round off errors as $A_2 \rightarrow 0$, so for the mass determinations by the ASTRA software, the following equation is employed:

$$M = \frac{2\left(\frac{R_0}{K^* c}\right)}{1+\sqrt{1-8A_2 c\left(\frac{R_0}{K^* c}\right)}} \tag{3.4}$$

If $A_2 \rightarrow 0$, then this equation simplifies to $M = \frac{R_0}{K^* c}$.[21] For soft particles in dilute solutions, the second virial coefficient can be considered negligible because the osmotic pressure of expansion of the molecules is zero at 25 °C and the particles should not be exerting any forces on each other. To obtain the rms radius, the following equation is used,

$$\left\langle r^2 \right\rangle = \frac{-3m_0\lambda^2}{16\pi M(1-4A_2 Mc)} \tag{3.5}$$

and R_z is determined from,

$$\left\langle r^2 \right\rangle_z = \frac{\sum\left(c_i M_i \left\langle r^2 \right\rangle_i\right)}{\sum\left(c_i M_i\right)} \tag{3.6}$$

where c_i, M_i, and $\langle r^2 \rangle_i$ are the mass concentration, molar mass, and rms radius of the *i*th slice of the eluted peak.[21]

Static light scattering data are presented in the chapters in which use of the particles is described. The averaged rms radius (R_z), molar masses (M_z), and number densities (N) of the particles were determined by multi-angle laser light scattering (MALLS, DAWN EOS, Wyatt Technologies, Inc.) prior to their use for thin-film fabrication. MALLS detection following asymmetric field flow fractionation (AFFF) was used to determine the z-average radii (R_z) for all particles.[22,23] The AFFF separation method uses a cross flow to separate the particles as a function of hydrodynamic volume. The cross flow acts to force larger particles against a cellulose membrane, while smaller particles elute to the MALLS detector faster. For all separations, an elution speed of 1.0 mL/min was used with a cross flow of 1.0 mL/min. The MALLS detector is equipped with a Peltier device to maintain a flow cell temperature of 25 °C and collects scattered light from 18 different fixed angles to determine the R_z of the particles. When MALLS is used in conjunction with a dRI detector, which measures the changes in refractive index as the sample passes through the detector, the z-averaged molar mass (M_z) can also be determined if the solution concentration and *dn/dc* of the material are known (*vide infra*). ASTRA 5.3.2.15 software was used to determine R_z and M_z values using the Debye fit method.[21] The particle size and molar mass were determined using a known concentration of particles in 10 mM PBS buffer (25 mM ionic strength).

3.2.3 Refractometry for *dn/dc* determination

Experimental. Differential refractive index measurements (dRI, OptiLab rEX, Wyatt Technologies, Inc.) were used to establish *dn/dc* and to determine the molar mass of each

particle. This analysis was performed using the Optilab rEX differential refractive index detector in batch mode. Calibration using dilutions of a sodium chloride solution from 0.1 mg/mL to 15.0 mg/mL was performed according to the guidelines provided with the instrument. The calibration was performed once at the beginning and once at the end of all sample analyses, and also after analysis of every five samples to check for calibration stability as recommended by the manufacturer. To determine the *dn/dc* value of the particles, at least 5 10-mL dilutions of each type of particle were made in distilled, deionized water with step-wise concentration ranges between 2.5 x 10^{-6} g/mL and 3.75 x 10^{-4} g/mL from stock solutions of known concentration. All samples were prepared in new, clean glass vials. In preparation, each vial was rinsed sequentially with deionized water, absolute ethanol, and HPLC-grade acetone, and then allowed to dry upside-down on a low-lint drying surface overnight. The lids for the vials were rinsed with water and ethanol only and allowed to dry overnight.

To perform the analysis, a baseline was established using filtered, distilled, deionized water. Each of the samples was introduced into the dRI detector using a 10-mL syringe placed on an in-line mechanical syringe pump set at a flow rate of ~0.45 mL/min. Each dilution was loaded into a new, clean 10-mL syringe. The water was introduced as the baseline and allowed to run for ~5 minutes. Then, starting with the lowest concentration sample for each type of particle, the samples were introduced sequentially by switching out the pre-loaded syringes. Each dilution was allowed to run for ~5 minutes before it was switched with the solution of the next higher concentration. After all of the concentration samples were introduced into the instrument, the baseline was reestablished with filtered, distilled, deionized water. The software provided with the instrument

plotted the data and calculated the *dn/dc* ratio from the slope of the graph of the data (Figure 3.1). The *dn/dc* value was plugged into the template when each sample was analyzed with MALLS to calculate the sample's molecular weight (*vide supra*).

Results. The values for *dn/dc* were determined for the microgel systems presented in Chapters 5 and 6. For the studies presented in Chapter 5, two types of core/shell microgels were synthesized. The difference between the two structures was the use of a degradable cross-linker, DHEA, in the core of one and a non-degradable cross-linker, BIS, in the core of the other. The microgels in Chapter 5 were subjected to *dn/dc* analysis for the simple purpose of determining M_z and, from that, number density in solution.

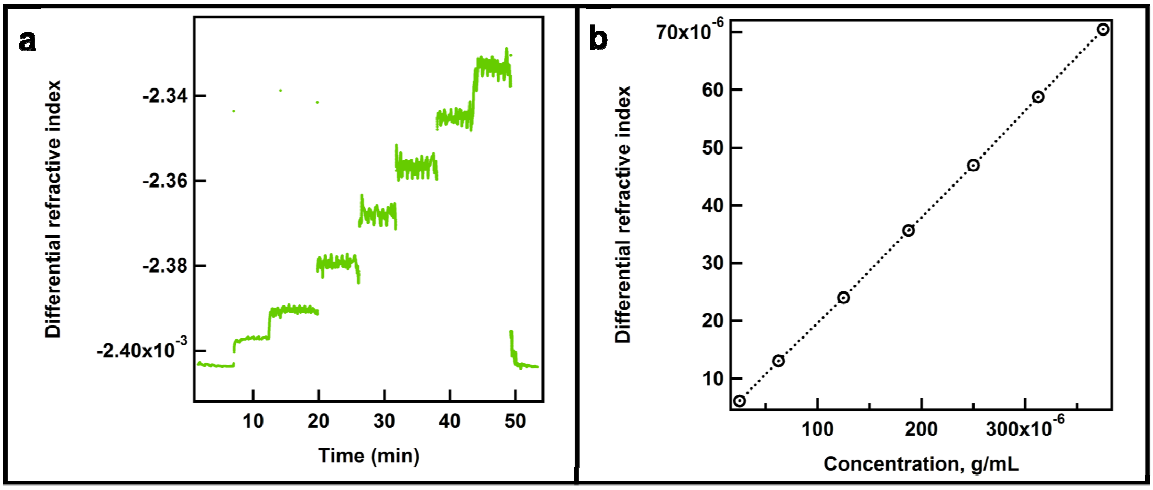

Figure 3.1. Graphs showing a) raw data, and b) differential refractive index as a function of concentration for a core/shell microgel with a BIS non-degradable cross-linker. The linear regression equation for (b) is y = 0.18375x + 1.305e-06, with R^2 = 0.9999.

For these analyses, a series of seven dilutions was made for each particle type in the concentration range of $2.50x10^{-5}$ g/mL to $3.75x10^{-4}$ g/mL. The *dn/dc* value for the core/shell microgel with a non-degradable BIS cross-linked core was 0.1836 (±0.0009) mL/g. The *dn/dc* for the core/shell microgel with a degradable DHEA cross-linked core was 0.1780 (±0.0007) mL/g.

For the studies presented in Chapter 6, ten types of *co*-cross-linked microgels were synthesized. The microgels all had a 9:1 ratio of NIPAm to AAc monomers and 2.5 mol% BIS crosslinker. The total mol% of the co-monomers was decreased to accommodate the increasing mol% of DHEA; the percentage range for DHEA concentration was 0-7.5mol%. The *dn/dc* values for the microgels synthesized for the

Table 3.1. Tabulated results of the *dn/dc* values for *co*-cross-linked microgels.

Synthesis number	Mol% DHEA[1]	Concentration range for analysis (g/mL)[2]	*dn/dc* (mL/g)
1	0	$2.5x10^{-5}$ – $2.5x10^{-4}$	0.1990 (±0.0040)
2	0.125	$2.5x10^{-5}$ – $2.5x10^{-4}$	0.1990 (±0.0025)
3	0.25	$2.5x10^{-5}$ – $2.5x10^{-4}$	0.2018 (±0.0033)
4	0.5	$2.5x10^{-5}$ – $2.5x10^{-4}$	0.1928 (±0.0030)
5	0.875	$2.5x10^{-5}$ – $2.5x10^{-4}$	0.1860 (±0.0007)
6	1.25	$2.5x10^{-5}$ – $2.5x10^{-4}$	0.1811 (±0.0072)
7	1.875	$2.5x10^{-5}$ – $2.5x10^{-4}$	0.2002 (±0.0162)
8	2.5	$5.0x10^{-6}$ – $6.25x10^{-5}$	0.1595 (±0.0054)
9	5	$5.0x10^{-6}$ – $6.25x10^{-5}$	0.1473 (±0.0035)
10	7.5	$5.0x10^{-6}$ – $6.25x10^{-5}$	0.1446 (±0.0131)

[1]Mol% of DHEA used in the monomer feed solution during synthesis.
[2]Five dilutions were made within this range from a stock of 0.0025 g/mL.

studies presented in Chapter 6 are outlined in Table 3.1. These values were determined to analyze each particle type for M_z so that, in conjunction with other data, the quantity of DHEA cross-links incorporated during the synthesis could be determined.

Discussion. As stated above, the *dn/dc* value is a measure of the polarizability of the macromolecule. It is a term that relates the refractive index increment with a molecular concentration.[17] A molecule with a charge or different cross-linkers will have a different polarizability factor and thus, for any new particle composition, the *dn/dc* must be determined. It is important to consider the measurement wavelength when determining *dn/dc* because as the wavelength increases, the *dn/dc* decreases proportionally. The *dn/dc* used to calculate molar masses from light scattering data must be measured at the same wavelength as that for the scattering data. Molecular weight is also a factor in determination of the *dn/dc* value. Up to a certain molar mass the *dn/dc* increases with increasing M_z, but its value will eventually plateau. The solvent will also affect *dn/dc*. With these parameters in mind, it is interesting to take a look at the *dn/dc* values of different kinds of microgels used in these studies.

For the core/shell particles presented in Chapter 5, it was important to know the molecular weights and number densities of the particles in the system so that approximate film compositions could be determined. The two particles have similar *dn/dc* values, but different molecular weights and composition.

For the *co*-cross-linked particles presented in Chapter 6, up to the point where the two cross-linkers are equal in their assumed molar representation within the macromolecule, the *dc/dc* value for a NIPAm-*co*-AAc with BIS-*co*-DHEA cross-linker system falls in the range 0.18-0.20 mL/g. The average of the *dn/dc* values from syntheses **1**-**7** is 0.1943 ±

0.0080 mL/g. The determinations of *dn/dc* values for syntheses **8**-**10** were performed well below the suggested concentrations for *dn/dc* determination. The lower values for these particles are most likely due to the high signal to noise ratio at those concentrations. Performing the *dn/dc* determination for these particles at higher concentrations did not yield linear results. When the decreasing *dn/dc* data are combined with the detailed data of particle morphology presented in Chapter 6, it also suggests that there may have been incomplete incorporation of one or more of the co-monomers or cross-linkers. The generally accepted value of *dn/dc* for pNIPAm is 0.167 at 25 °C in water measured at 633 nm.[24,25] Since the *dn/dc* values are closer to the value for pNIPAm, the result indicates that NIPAm may be dictating the polarizability of the particle while the cross-linker has little effect. For acrylamide-acrylic acid co-polymers, however, the *dn/dc* value decreases with increasing acid-to-acrylamide ratios. Since these particles presumably also have significant amounts of DHEA in their structures, the DHEA molecule may instead be increasing its influence on the *dn/dc* value in a similar fashion. It may also simply indicate that the molar mass is low enough to affect *dn/dc*.

In general, the *dn/dc* values for pNIPAm microgels fall within the range 0.15-0.20 mL/g. The primary reason for determining *dn/dc* ratios for microgel particles is to calculate molar mass and number density. Given that the molecular weights of the particles are on the order of 10^9 g/mol, determination of molecular weights that are accurate to more than one significant figure is unreasonable. Thus, it is likely that molecular masses calculated by using *dn/dc* values for the primary monomer, in this case pNIPAm, would be just as accurate.

References

1. Heskins, M.; Guillet, J. E., "Solution properties of poly(N-isopropylacrylamide)." *J. Macromol. Sci., Chem.* **1968,** 2, 1441-55.

2. Schild, H. G., "Poly(N-isopropylacrylamide): experiment, theory and application." *Prog. Polym. Sci.* **1992,** 17, 163-249.

3. Chandler, D., "Interfaces and the driving force of hydrophobic assembly." *Nature* **2005,** 437, 640-647.

4. Winnik, F. M.; Ottaviani, M. F.; Bossman, S. H.; Pan, W. S.; Garciagaribay, M.; Turro, N. J., "Phase-Separation of poly(N-Isopropylacrylamide) in Water - A Spectroscopic Study of a Polymer Tagged with a Fluorescent Dye and a Spin-Label." *J. Phys. Chem.* **1993,** 97, 12998-13005.

5. Rice, C. V., "Phase-transition thermodynamics of N-isopropylacrylamide hydrogels." *Biomacromolecules* **2006,** 7, 2923-2925.

6. Berndt, I.; Pedersen, J. S.; Lindner, P.; Richtering, W., "Influence of Shell Thickness and Cross-Link Density on the Structure of Temperature-Sensitive Poly-N-Isopropylacrylamide-Poly-N-Isopropylmethacrylamide Core-Shell Microgels Investigated by Small-Angle Neutron Scattering." *Langmuir* **2006,** 22, 459-468.

7. Berndt, I.; Pedersen, J. S.; Richtering, W., "Structure of Multiresponsive "Intelligent" Core-Shell Microgels." *J. Am. Chem. Soc.* **2005,** 127, 9372-9373.

8. Berndt, I.; Popescu, C.; Wortmann, F.-J.; Richtering, W., "Mechanics versus thermodynamics: swelling in multiple-temperature-sensitive core-shell microgels." *Angew. Chem., Int. Ed.* **2006,** 45, 1081-1085.

9. Jones, C. D.; Baker, C.; Lyon, L. A., "Synthesis and characterization of environmentally responsive core-shell hydrogel nanoparticles." *Mater. Res. Soc. Symp. Proc.* **2001,** 662, NN1 4/1-NN1 4/6.

10. Jones, C. D.; Lyon, L. A., "Synthesis and Characterization of Multiresponsive Core-Shell Microgels." *Macromolecules* **2000,** 33, 8301-8306.

11. Jones, C. D.; Lyon, L. A., "Dependence of Shell Thickness on Core Compression in Acrylic Acid Modified Poly(N-isopropylacrylamide) Core/Shell Microgels." *Langmuir* **2003,** 19, 4544-4547.

12. Jones, C. D.; Lyon, L. A., "Shell-Restricted Swelling and Core Compression in Poly(N-isopropylacrylamide) Core-Shell Microgels." *Macromolecules* **2003,** 36, 1988-1993.

13. McGrath, J. G.; Lyon, L. A., "Thermoresponsive core/shell nanocomposites of poly-nisopropylacrylamide: Hard core optical devices." *Abstracts of Papers of the American Chemical Society* **2005,** 229, U734-U734.

14. Nayak, S.; Gan, D.; Serpe, M. J.; Lyon, L. A., "Hollow thermoresponsive microgels." *Small* **2005,** 1, 416-421.

15. Sorrell, T. N., *Organic Chemistry*. Second Edition ed.; University Science Books: Sausalito, CA, 2006.

16. Gan, D.; Lyon, L. A., "Tunable Swelling Kinetics in Core-Shell Hydrogel Nanoparticles." *J. Am. Chem. Soc.* **2001,** 123, 7511-7517.

17. Wyatt, P. J., "Light scattering and the absolute characterization of macromolecules." *Anal. Chim. Acta* **1993,** 272, 1-40.

18. Pecora, R., *Dynamic Light Scattering: Applications of Photon Correlation Spectroscopy*. Plenum Press: New York, 1985.

19. White, R. J., "FFF-MALS - A new tool for the characterisation of polymers and particles." *Polym. Int.* **1997,** 43, 373-379.

20. Wyatt Technologies, I., In *Light Scattering University: DAWN Course Manual*, Wyatt Technologies, Inc.: Santa Barbara, CA, 2004.

21. Wyatt Technologies, I., *ASTRA V User's Guide Version 5.1* **2004**.

22. Blackburn, W. H.; Lyon, L. A., "Size-controlled synthesis of monodisperse core/shell nanogels." *Colloid Polym. Sci.* **2008,** 286, 563-569.

23. McGrath, J. G.; Bock, R. D.; Cathcart, J. M.; Lyon, L. A., "Self-Assembly of "Paint-On" Colloidal Crystals Using Poly(styrene-co-N-isopropylacrylamide) Spheres." *Chem. Mater.* **2007,** 19, 1584-1591.

24. Gao, J.; Wu, C., "The "Coil-to-Globule" Transition of Poly(N-Isopropylacrylamide) on the Surface of a Surfactant-Free Polystyrene Nanoparticle." *Macromolecules* **1997,** 30, 6873-6976.

25. Arleth, L.; Xia, X.; Hjelm, R. P.; Wu, J.; Hu, Z., "Volume Transition and Internal Structures of Small Poly(N-isopropylacrylamide) Microgels." *J. Polym. Sci., Part B: Polym. Phys.* **2005,** 43, 849-860.

CHAPTER 4

BIMODAL SWELLING RESPONSES IN MICROGEL THIN FILMS

4.1 Introduction

For the past 15 years, polyelectrolyte based assembly of thin films has been used to design many materials with myriad functions. Thin films have tremendous utility for use in biomedical devices, sensors, and optical materials.[1] Using a layer-by-layer technique to construct thin films allows greater control over the structure and function of the films. Because of the tremendous variability that is available in the concentration of components, chemical composition, and physical properties of the film building blocks, the surface of thin film construction has only been just scratched.[2]

One can conceptualize microgel films by means of a "bricks and mortar" analogy. In general, microstructured films using materials like hydrogels are built from the substrate in the same way that a brick wall is built from the ground up. In these films, the micron-sized components represent the bricks, which can largely dictate the functionality and behavior of the film. The mortar can be any number of materials that interacts with the bricks in a polyvalent fashion, such as a linear, complimentarily charged polyelectrolyte. The construction of micro- and nanostructured thin films has been largely achieved through various means such as the Langmuir-Blodgett[7,8] and layer-by-layer techniques.[6,9] Several studies have investigated ways to construct thin films on unconventional substrates such as hydrophobic surfaces[10] and through spatially-controlled means like

micropatterning,[11] or by creating films using pH tunable polyelectrolytes to control deposition.[12] From there, considerable research has gone into developing multilayer films that function as electrodes,[13] non-fouling surfaces,[14] tunable controlled-release substrates,[15-18] and materials for lightweight and flexible display applications.[19,20]

This chapter reports on the construction of polyelectrolyte thin films using negatively charged, spherical hydrogel particles and positively charged linear polymer chains. A detailed understanding of the pH-induced morphological changes occurring in these films was gained by using a range of optical, acoustic, and microscopic characterization tools.[3] The results suggest that films with unusual bimodal swelling responses can be obtained from simple fabrication methods (Scheme 1).

4.2 Experimental Section

Materials. All reagents were purchased from Sigma-Aldrich unless otherwise specified. The monomer *N*-isopropylacrylamide (NIPAm) was recrystallized from hexanes (J.T. Baker) and dried under vacuum prior to use. The cross-linker *N*,*N*'-methylenebis(acrylamide) (BIS), sodium dodecyl sulfate (SDS), and ammonium persulfate (APS) were used as received. Poly(allylamine hydrochloride) (PAH), MW 15 000 Da and MW 70 000 Da, was used as received. Formic acid, 88%, was purchased from J. T. Baker and used as received. Buffer components 2-[*N*-morpholino]-ethanesulfonic acid hydrate (MES) and sodium chloride were used as received. The Au surface modification reagent 2-mercaptoethylamine (MEA) was used as received and stored at 4 °C. Polished quartz crystals (5.0 MHz, AT-cut) were purchased from Stanford

Scheme 4.1. Schematic depiction of the bimodal swelling model.

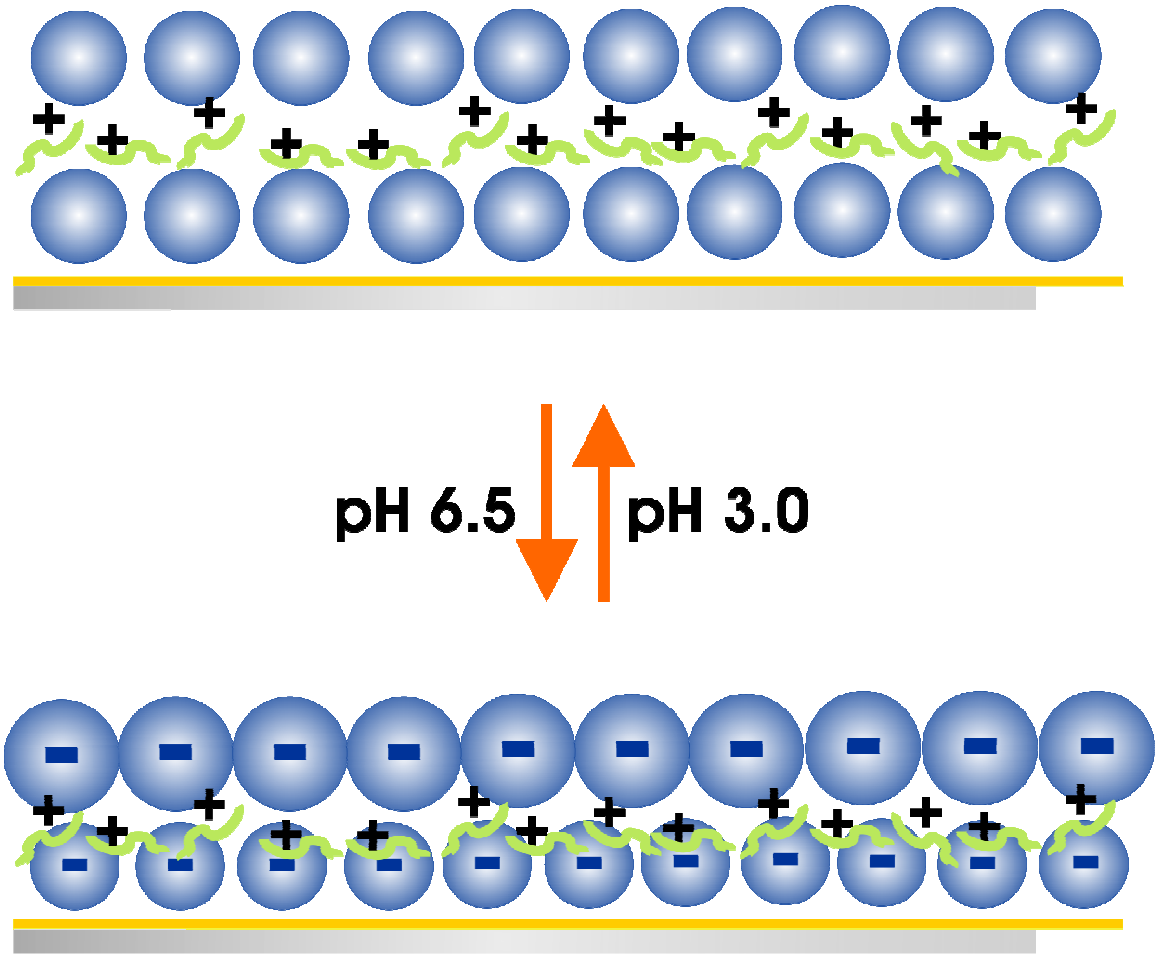

Research Systems (Sunnyvale, CA). Au (99.999% pure) was obtained from Alfa Aesar. Glass substrates were 24 × 24 mm Fisher Finest brand cover glass from Fisher Scientific. Ethanol (95% and absolute) was used for various purposes in this investigation. Water used in this investigation was house distilled, then deionized to a resistance of at least 18 MΩ (Barnstead Thermolyne E-Pure system), and then filtered through a 0.2 μm filter.

Microgel Synthesis. The same batch of microgels was used throughout this investigation. The microgels were composed of 88% NIPAm, 2% BIS, and 10% AAc and were synthesized via aqueous free-radical precipitation polymerization as previously described,[3,4] using 70 mM total monomer concentration. The polymerization feed was composed of 0.7000 g (6.186 mmol) NIPAm, 0.0221 g (0.1433 mmol) BIS, 0.0386 g (0.1338 mmol) SDS, and 48 μL (0.6994 mmol) AAc dissolved in 99 mL deionized water. The initiator, 0.0386 g (0.1429 mmol) APS, was separately dissolved in 1 mL of deionized water. The reaction was allowed to proceed for 4 hours at 70 ± 2 °C under N_2. The resultant colloidal dispersion was filtered and the microgels were purified by 2 weeks of dialysis in 10 000 MWCO dialysis tubing. The solution was further purified by centrifugation using a relative centrifugal force (RCF) of 15 422 x *g* at 29 °C for 2 hours. The white pellet at the bottom of the tube was redispersed into pH 3.0 buffer by vortexing. After 3 cycles of centrifugation and redispersion the microgels were centrifuged one final time and redispersed into distilled, deionized water.

Quartz Crystal Microgravimetry Measurements and Thin Film Deposition. Before polyelectrolyte deposition, the Au electrodes on 5-MHz polished quartz crystals were rendered positively charged by adsorbing a cationic alkanethiol (MEA) to the surface.[4] In this case, the substrates were immersed in a 1.0 mM ethanolic MEA solution (200 proof

ethanol) for 24 h. Following MEA functionalization, the substrates were rinsed and stored in ethanol and were used within 7 days. Prior to alternate layer deposition, the substrates were rinsed with deionized (DI) H_2O and dried under a stream of N_2 gas. To assemble the thin film atop this layer the substrate was securely attached to a glass coverslip via double-sided tape contacting the nonmetalized regions of the crystal. This assembly was then placed on the vacuum chuck of a spin coater (Specialty Coating Systems, model P6700), and spun at 3000 rpm. Ten drops of DI H_2O were added to the metallized region of the crystal. Following that, twenty-five drops of an aqueous, pH 6.5, 10% (v/v) microgel solution were added to the metallized region of the crystal. The substrate was allowed to spin for ~15 s following microgel addition. The spinning substrate was then rinsed with ten drops of DI water and allowed to spin for an additional ~30 s. The quartz crystal can be removed from the tape holding it to the glass substrate at any time to allow QCM measurements. After microgels were added, the crystal was placed into a 45 °C oven and dried overnight. The crystal was removed from the oven and situated in the QCM flow cell (volume of ~0.15 mL). Nitrogen gas was flowed over the crystal for ~30 minutes to equilibrate the crystal to room temperature. The resistance and frequency were then measured under a stream of N_2 until the response was stable for 5-10 minutes. Then pH 3.0 formate buffer, 10 mM ionic strength, was introduced into the flow cell chamber for ~5 minutes. The pH 3.0 buffer was switched off and a pH 6.5 MES buffer, 10 mM ionic strength, was flowed into the cell for ~5 minutes. The pH was switched from 3.0 to 6.5 three times each and measurements of R_m and f_r were made for each switch. The crystal was then removed and placed back onto the vacuum chuck and a layer of PAH, pH 6.5, 0.0526 monoM (mol monomer/L) was added in the same manner as described

above for particle deposition. The crystal was returned to the flow cell and the pH-dependent response of the film was measured again. This procedure was repeated until 5 microgel/PAH bilayers were deposited onto and measured with the QCM crystal.

Surface Plasmon Resonance Spectroscopy. Surface plasmon resonance spectra were obtained using by the instrument (described in Chapter 2). Gold-coated (50 nm) cover slips were exposed to a 1 mM, ethanolic MEA solution for 24 h to render the gold surface positively charged. Films were built onto the substrates using the scLbL technique. Buffers of pH 3.0 and 6.5 were injected into the flow cell in the same sequence as for the QCM measurements described above.

Photon Correlation Spectroscopy. The pH dependent hydrodynamic radii of the pNIPAm-*co*-AAc microgels were determined by photon correlation spectroscopy (PCS; Protein Solutions, Inc.) prior to their use for thin-film fabrication. The microgels were measured in the same pH 3.0 and pH 6.5 buffers used for the QCM experiments to determine the size of the microgels at 23 °C.

Ellipsometry. Substrates and samples were created for ellipsometry measurements in the same manner as the substrates and samples for SPR measurements. Measurements were taken by using a M-2000V spectroscopic ellipsometer from J. A. Woollam (Lincoln, NE). The data were analyzed using the Cauchy Model in the WVASE32® software provided with the instrument.

Atomic Force Microscopy. AFM data were taken both in air and in fluid in AC mode on an Asylum Research MFP3D. Spring constants were calculated using the thermal method. Imaging and analysis was performed using the Asylum Research MFP3D

software running in IgorPro (WaveMetrics, Inc., Lake Oswego, OR) that was provided with the instrument.

For images of the film coverage in air, an Olympus AC240 cantilever was used (k=2 N/m, f_0=71 kHz). In fluid the longer of the two cantilevers on the Olympus TR 800 was used (k=0.14 N/m, f_0=24 kHz in air, 6.5 kHz in fluid). To prepare AFM samples, 3-aminopropyltrimethoxysilane (APTMS) was attached to the substrates by exposing Ar plasma-cleaned glass for 2 h to a 1% (v/v) solution of APTMS in absolute ethanol. These substrates were then used for scLbL deposition, as described above.

For film thickness determination in air, an Olympus AC160 cantilever was used (k=42 N/m, f_0=300 kHz). In fluid the shorter of the two cantilevers on the Olympus TR 400PB was used (k=0.09 N/m, f_0=32 kHz in air, 6.5 kHz in fluid). To create the AFM samples for film thickness determination, gold substrates were prepared as for surface plasmon resonance spectroscopy (described above). Film samples for 0.5-, 2.5-, and 4.5-bilayer films, where microgels form the top layer, were prepared by scLbL deposition. A blank gold slide was scratched with a clean, new razor blade to create a line visible by the camera built into the AFM head. The absolute thickness of the gold surface was determined by imaging an area 90 μm x 90 μm that spanned the entirety of the scratch (resolution of 512 x 512 pixels for each image). The polymer samples were scratched and imaged in a similar way. Each sample was exposed to pH 3.0 and 6.5 buffers, and liquid imaging was performed for each (resolution of 256 x 256 pixels for each image). To determine the thickness for each film under each condition, the software provided with the AFM was used to process the image and perform an averaged line analysis over 100 lines for each image. A point along the averaged line inside the scratch (A) and a point on

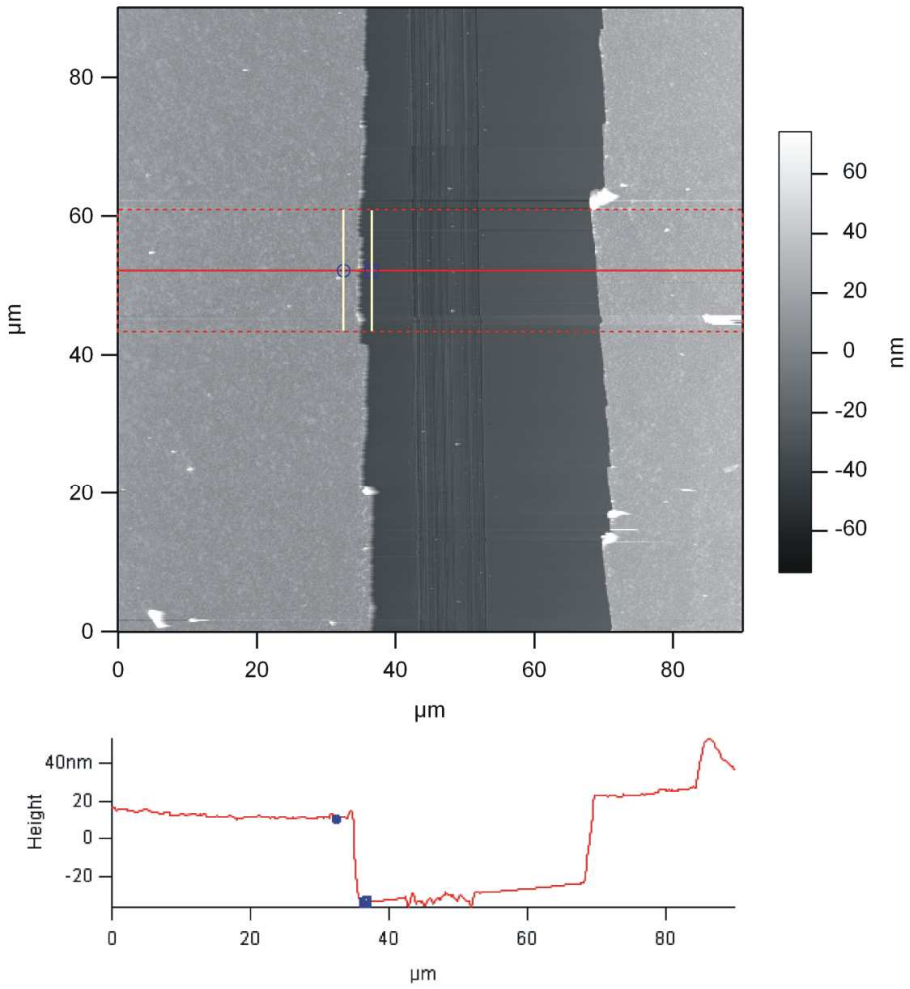

Figure 4.1. AFM image showing film thickness analysis. Image is a 512 x 512 resolution image of a dry 4.5-layer film on gold. The bright areas are the polymer film on gold, and the dark area is the scratch made by the razor blade. The horizontal dashed red lines indicate the boundary of the 100 lines over which the data was averaged. The horizontal solid red line is an average of those 100 lines and is represented by the average line profile shown below the image. The points represented by the cursors (circle and square) on the graph are an average of the height at those pixels on each of the 100 lines (vertical white lines). For this analysis, the height difference was used to represent the overall thickness of the film (gold + polymer film).

the film surface (B) were selected, and A was subtracted from B to get an absolute thickness of the (Au + polymer) film for each sample (Figure 4.1). Then the value for the thickness of the gold layer was subtracted from the thickness of each total film to calculate the absolute thickness of each polymer film.

4.3 Results

Thin films of pNIPAm-*co*-AAc (AAc) microgels, diameter ~220 nm in pH 3.0 buffer, and poly(allylamine hydrochloride) (PAH), 15 000 Da MW or 70 000 Da MW, were assembled using a spin-coating layer-by-layer (scLbL) technique.

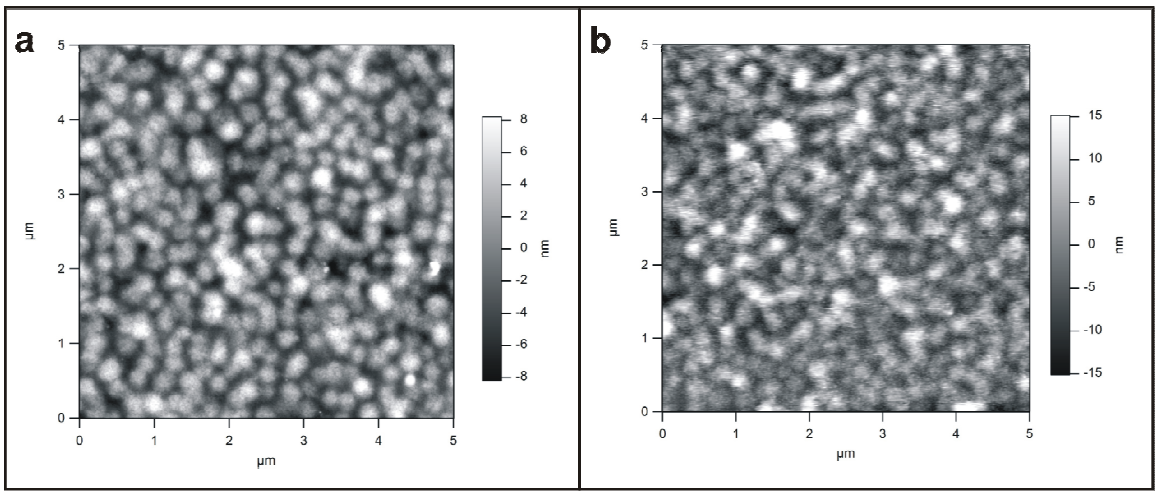

Figure 4.2. Film characterization images. (a) An AFM image of a dry 3.5-bilayer film where microgels form the top layer. Axes are 5 µm. (b) An AFM image of the same 3.5-layer film hydrated (in pH 3.0 buffer). Axes are 5 µm.

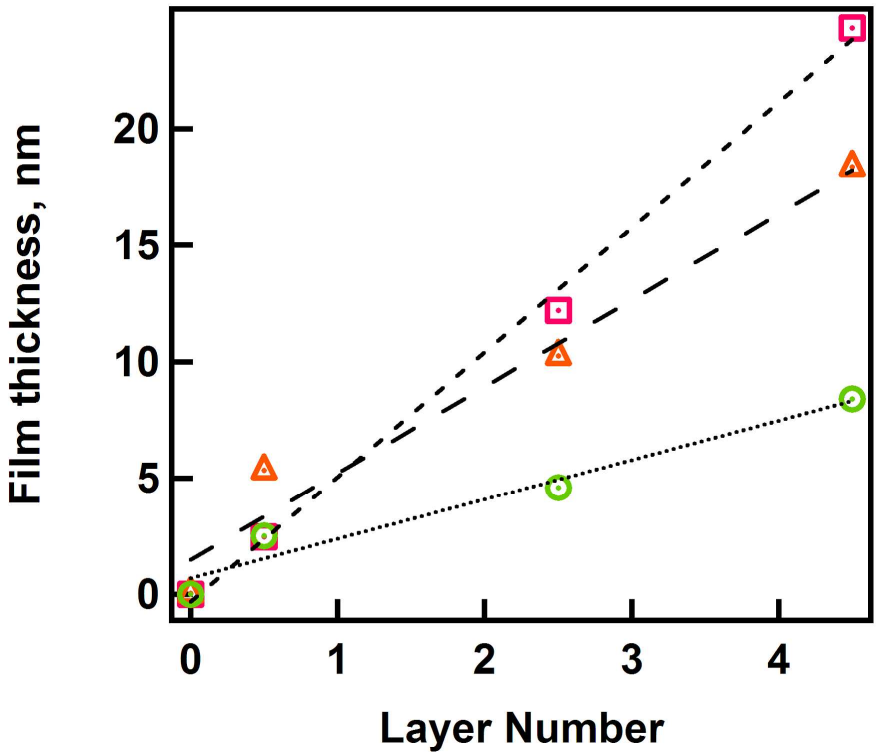

Figure 4.3. AFM thickness data show an increase in the film thickness with increasing layer number. The linear regression equations are: thickness in air (dotted line + green circles) is y = 1.6932x + 0.7047, with R^2 = 0.9594; thickness in pH 3.0 buffer (short-dashed line + pink squares) is y = 5.3627x - 0.3107, with R^2= 0.9969; and thickness in pH 6.5 buffer (long-dashed line + orange triangles) is y = 3.7199x + 1.4829, with R^2 = 0.965.

Initial characterizations of the film composition and build-up for films using 15 000 MW PAH as the cationic glue between the microgel layers were performed with atomic force microscopy (AFM; Figures 4.2 and 4.3), surface plasmon resonance (SPR; Figure 4.4), and ellipsometry (Figure 4.5). Figures 4.2a and 4.2b show AFM micrographs (topography) of a multilayer film in air and pH 3.0 buffer, respectively. This particular film is 3.5-bilayers thick (3 PAH/4 microgel depositions), with microgels being the last (topmost) layer deposited. Both images show a fairly continuous film of microgels, suggesting uniform deposition during spin coating. Film thickness measurements were also made by using AFM (Figure 4.3) on dry films, as well as on films swollen in pH 3.0 and pH 6.5 buffers for films where microgels form the top layer; these data indicate that film thickness increases linearly with layer number. If one looks closely at the data for films in liquid, one sees that the film is thicker when the pH values is 3.0 than pH 6.5, with the exception of the 0.5-bilayer film (microgels only). The films appear to be much thinner than one would expect, considering that the microgels by PCS are ~220 nm in diameter at pH 3.0. The data show that the dried films are only about 8.3 nm thick for a 4.5-bilayer film. When the films are imaged in liquid, the same 4.5-bilayer film is about 24.3 nm thick at pH 3.0 and about 18.3 nm thick at pH 6.5. Similarly, in-situ (pH 3.0 and 6.5) SPR data as a function of layer number show a linear increase in plasmon resonance wavelength (Figure 4.4). These data all suggest that the spin coating method is valid and effective for building up uniform multilayers in a controlled and reproducible fashion. Ellipsometry measurements show a linear increase in film thickness (Figure 4.5). The SPR results also indicate that the “optical thickness” of the films increases when the pH of the surrounding fluid was changed from pH 3.0 to pH 6.5 (Figures 4.6, 4.7, and 4.8).

Specifically, a red shift of the wavelength of the plasmon resonance is observed with an increase in pH. This behavior is independent of the composition of the top layer of the film.

The thickness for the films appear to be greater when measured by this method as compared to the AFM measurements; however, further manipulation of the data using the software provided with the instrument diminished each measured thickness to zero.

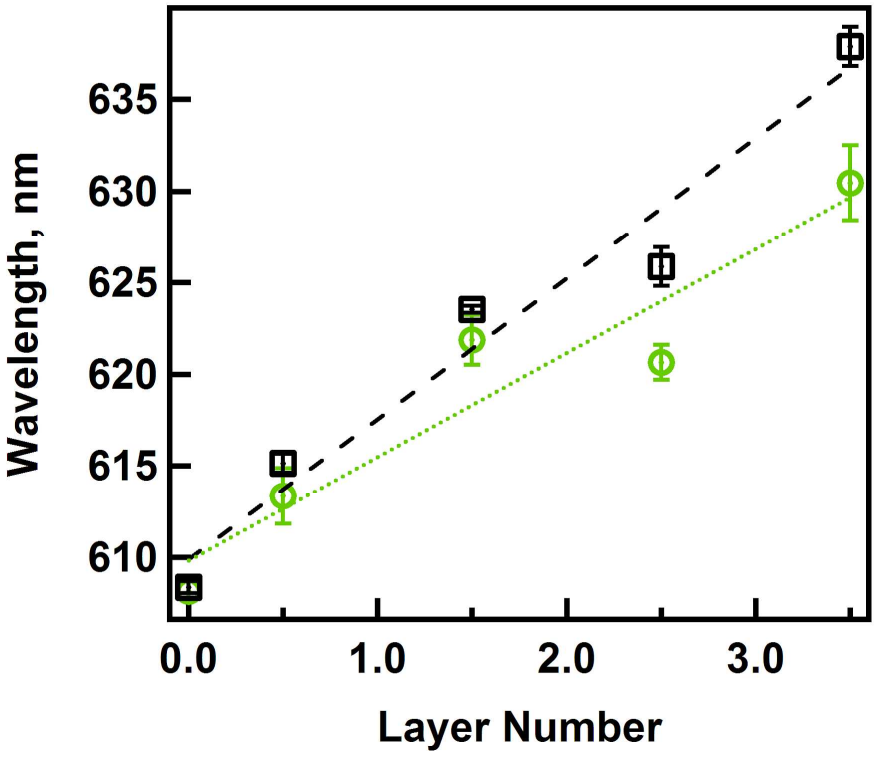

Figure 4.4. Surface plasmon resonance data shows an increase in plasmon wavelength with increasing layer number. The light green circles represent the film in pH 3.0 buffer; the linear regression for the pH 3.0 data (green dotted line) is y = 5.6771x + 609.81, with R^2 = 0.9052. The black squares represent the film in pH 6.5 buffer; the linear regression for the pH 6.5 data (black dashed line) is y = 7.6656x + 609.9, with R^2 = 0.9594.

QCM measurements illustrate that for a film with microgels on top (Figures 4.9a, 4.9c, 4.9e and Figures 4.10a, 4.10c, and 4.10e), the frequency and resistance values change in opposite directions when the pH is increased from 3.0 to 6.5. Overall, the microgel-terminated films composed of 0.5 to 4.5 PAH/microgel bilayers which were studied in all cases showed that the motional resistance of the QCM increases and the frequency decreases as the pH is increased from 3.0 to 6.5. However, if films where 15 000 MW PAH forms the top layer are measured, there are marked differences in the pH response between films that are 1- or 2-bilayers thick and films that are 3- to 5-bilayers thick.. For films that are 1- or 2-bilayers thick (Figures 4.9b), the QCM resistance responses to the pH change (resistance increases at pH 6.5) are similar to those observed for a film where microgels form the top layer. However, the frequency *increases* at that pH in contrast with a frequency decrease observed for the microgel monolayer. For films that are 3- to 5-bilayers thick (Figures 4.9d and 4.9f) the frequency increases when the pH is increased to 6.5, whereas the motional resistance shows a small decrease at that pH. Interpretations of these results are presented in the following section.

A set of experiments using SPR and QCM was also performed using 70 000 MW PAH as the polycationic glue between the microgel layers. The SPR data show the same trend as the results described above for films using 15 000 MW PAH. At pH 6.5 the optical density of the material increases and is manifested as a red-shift in the spectral data. The response is reversible over several cycles (Figures 4.6, 4.7, and 4.8). The QCM data is also similar, but the inversion of the resistance response does not occur until the fifth bilayer is added. Figure 4.10 shows layer data for 3-, 4-, and 5-bilayers. The

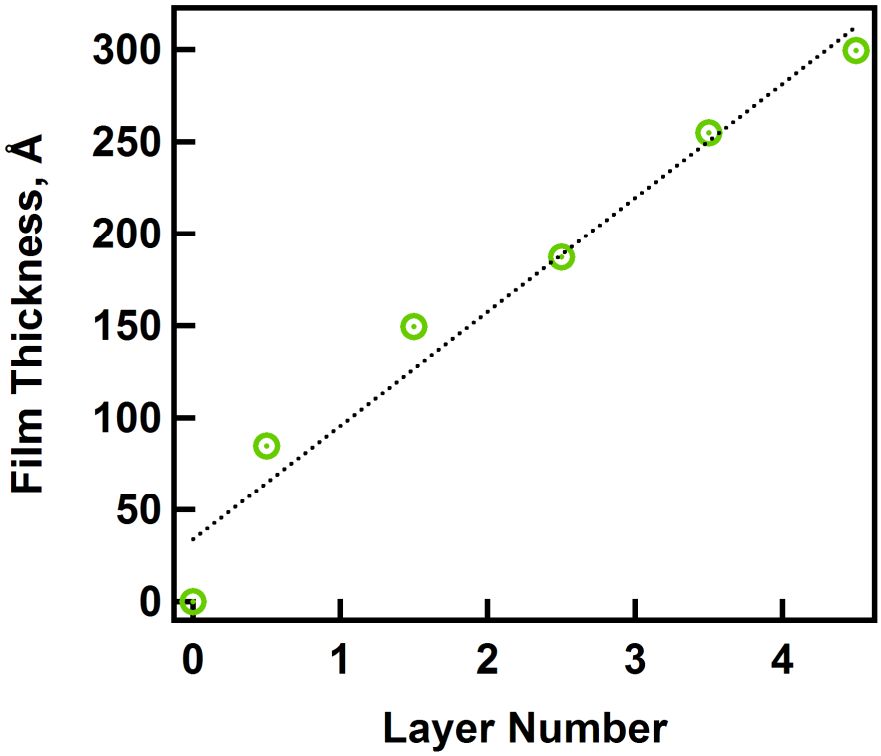

Figure 4.5. Ellipsometry data showing a linear increase in film thickness (green circles). The linear regression for the data is $y = 61.9x + 33.7$, with $R^2 = 0.9627$.

inversion of the resistance is not as clearly demarcated between layers as it is in films composed with 15 000 MW PAH as the fourth bilayer, which shows a null delta R in response to changes in pH (Figure 4.10d).

4.4 Discussion

The AFM data compiled in Figure 4.3 were surprising. The thicknesses of the films reveal two phenomena: (a) films at pH 6.5 are thinner than the films at pH 3.0, and (b) overall the films are much thinner than expected. The pH dependent phenomenon will be discussed below in conjunction with the SPR and QCM data. The overall thickness results will be addressed here. As stated in the results section, the microgels that these films are composed of have an R_h of ~220 nm in pH 3.0 buffer (by PCS). The lateral particle dimensions observed in the AFM topography images suggest that this size measurement is accurate. However, from the small heights of the films, it is clear that the scLbL technique flattens the microgels causing a strong adhesion to and spreading on the gold surface. Thus, the films may have properties that are strongly divergent from the behavior of particles in solution, as they will be perturbed by both the substrate and the surrounding film (PAH/microgel) matrix.

Given the measured thicknesses of the films, consider now the SPR results. In the SPR technique, the evanescent field decays exponentially from the gold surface as it penetrates a sample. The penetration depth of the SPR evanescent wave in these studies is ~200 nm. At the film thicknesses used in these studies, the evanescent wave will span the entire film, so the SPR response will represent the average behavior of the film. Even so,

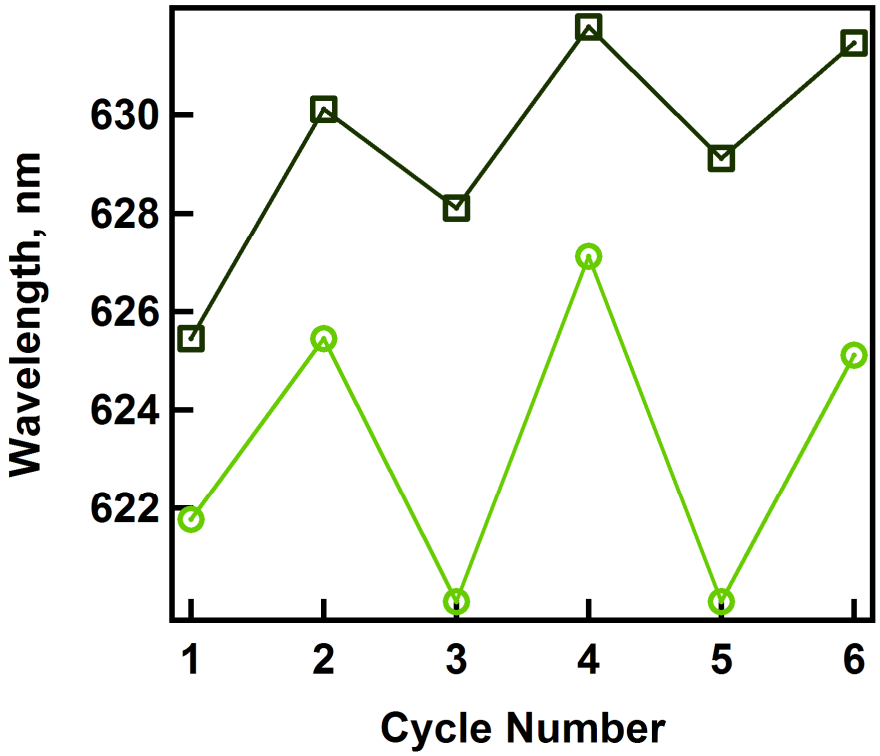

Figure 4.6. SPR data for 2.5- and 3-layer films shows the change in the plasmon wavelength as the pH is switched. Each of the SPR experiments involved switching the pH of the fluid in the flow cell from pH 3.0 to pH 6.5. Cycles 1, 3, and 5 represent data for pH 3.0 buffer. Cycles 2, 4, and 6 represent data for pH 6.5 buffer. The light green circles represent a 2.5-bilayer film where microgels form the top layer. The black squares represent a 3-bilayer film where PAH forms the top layer.

we assume that the greatest part of that response will represent the part of the film closest to the gold surface where the plasmon field is the strongest. In contrast, a previous study reported the use of PAH and pNIPAm-*co*-AAc microgels to create much thicker films, where this assumption is not valid. As described below, the findings here are similar to those reported previously for SPR.[5]

The data shown in Figures 4.4, 4.6, 4.7, and 4.8 reveal two things. First, the optical thickness, which is a convolution of the geometric thickness and the film refractive index,

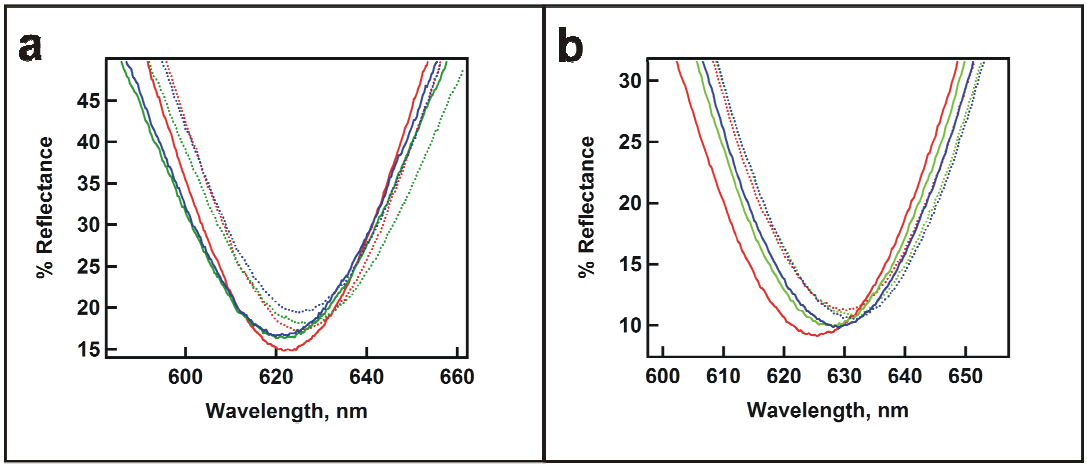

Figure 4.7. Wavelength-resolved SPR curves for films constructed using 15 000 MW PAH where (a) microgels form the top layer (2.5 layers); (b) PAH forms the top layer (3 layers). Dotted curves represent data obtained at pH 6.5 and solid curves represent data obtained at pH 3.0. Each of the SPR experiments involved switching the pH of the fluid in the flow cell from pH 3.0 to pH 6.5. Cycles 1, 3, and 5 represent data for pH 3.0 buffer. Cycles 2, 4, and 6 represent data for pH 6.5 buffer. Red curves represent data for cycles 1 and 2, green curves represent data for cycles 3 and 4, and blue curves represent data for cycles 5 and 6.

increases with layer number, as expected. Second, the optical thickness increases as the pH is changed from 3.0 to 6.5 (Figures 4.6 and 4.8-inset). This result apparently contradicts the AFM results that show a thickness *decrease* at pH 6.5 (Figure 4.3). Thus, the conclusion is that the film refractive index increases at pH 6.5, which contributes more to the increase in optical thickness than the counterbalancing decrease in film thickness.[6,7] Furthermore, there is an increase in PAH-based cross-linking of the microgel film at pH 6.5, and a concomitant deswelling at that pH, as described previously.[5] These effects arise from greater deprotonation of the AAc units in the microgels (pK_a = 4.25) and a subsequent increase in the association between the anionic polymer chains in the microgels and the cationic PAH.[5] The increase in cross-linking leads to deswelling of the particle by condensation of the polymer network and an associated increase in the refractive index. Kuckling and Frank have observed similar effects in photo-cross-linked hydrogel films.[16-19]

The SPR data for films constructed with 70 000 MW PAH was only taken for films where the particles formed the top layer (Figure 4.8), but they show similar trends. As the pH is switched from 3.0 to 6.5, there is a concomitant red shift in the plasmon absorbance, which indicates that the film becomes more optically dense. It is equally likely in these cases that the top layer of the film has little impact on the overall plasmon response observed, similar to results for the films constructed with 15 000 MW PAH.

Because of the apparent dependence on the identity of the top layer of the film, the QCM data present a more complicated picture. As stated above, the SPR results indicate that an increase in pH is accompanied by an increase in film density (refractive index).

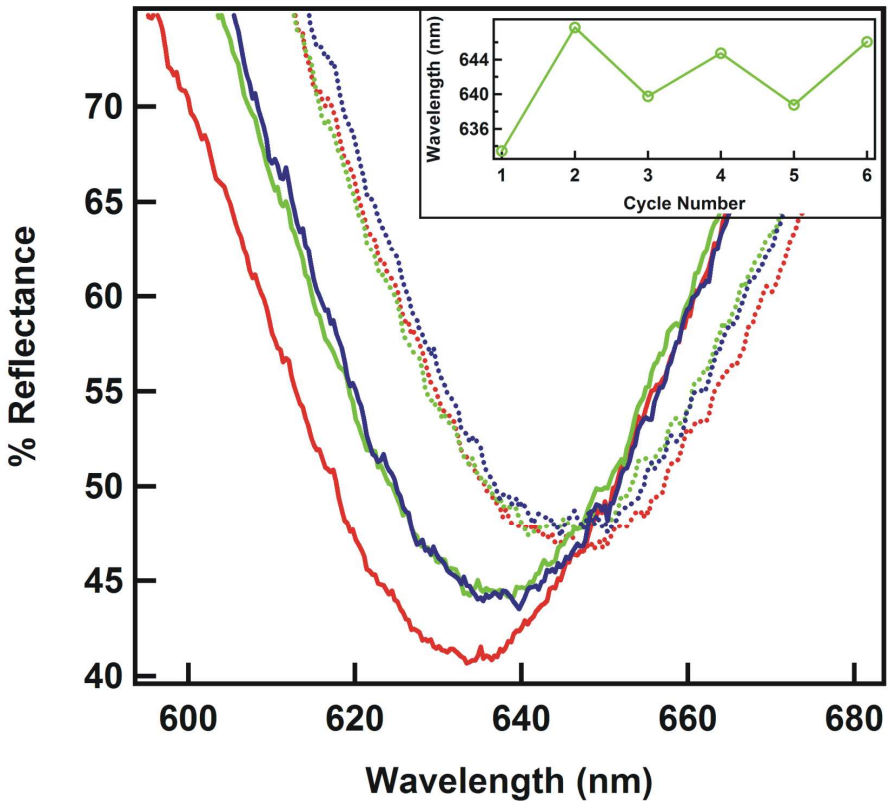

Figure 4.8. Wavelength resolved SPR curves for a 4.5 layer films constructed with 70 000 MW PAH. Dotted lines represent data obtained at pH 6.5 and solid curves represent data obtained at pH 3.0. The inset shows the change in the plasmon wavelength as the pH is switched. Each of the SPR experiments involved switching the pH of the fluid in the flow cell from pH 3.0 to pH 6.5. Cycles 1, 3, and 5 represent data for pH 3.0 buffer. Cycles 2, 4, and 6 represent data for pH 6.5 buffer. Red curves represent data for cycles 1 and 2, green curves represent data for cycles 3 and 4, and blue curves represent data for cycles 5 and 6.

To understand the more complicated QCM data, one should first look at the behavior of the films constructed with 15 000 MW PAH starting with a single microgel layer (0.5-bilayer). If PAH cross-linking is indeed critical to the behavior of the film, one would expect that a particle monolayer would behave similarly to free particles in solution, albeit perturbed somewhat by the presence of the substrate. The data in Figure 4.9a show that this is indeed the case. When the pH is raised to 6.5, the QCM shows a decrease in frequency (increase in mass due to water ingress) due to microgel swelling; the swelling arises from deprotonation of the AAc groups, which increases the Coulombic repulsion between the polymer chains in the microgel.[5,8,9] A concomitant increase in resistance is also observed. Because the resonant (or motional) resistance is a measure of acoustic dampening or film "softness"[10-13] it is not surprising that it should increase upon particle swelling. The AFM measurements shown in Figure 4.3 corroborate this behavior by showing that the thickness of the monolayer is greater in pH 6.5 liquid than in pH 3.0 liquid. However, when PAH is added to the microgel monolayer to create a 1-bilayer film, a small loss in mass (increase in frequency) is observed at pH 6.5, whereas the resistance still shows a small increase (i.e. dampening response, see Figure 4.9b) upon switching from pH 3.0 to 6.5. The same is true for a 2-bilayer film (data shown in Table 4.1) and for films constructed with 70 000 MW PAH that are 1- to 3-bilayers thick (Table 4.2 and Figures 4.10a and 4.10b). This phenomenon presumably arises from the presence of acid groups that are not coupled with PAH. These microgels will swell slightly when the pH increases from pH 3.0 to pH 6.5 and perhaps contribute to a small increase in motional resistance due to acoustic dampening. The majority of the film appears to

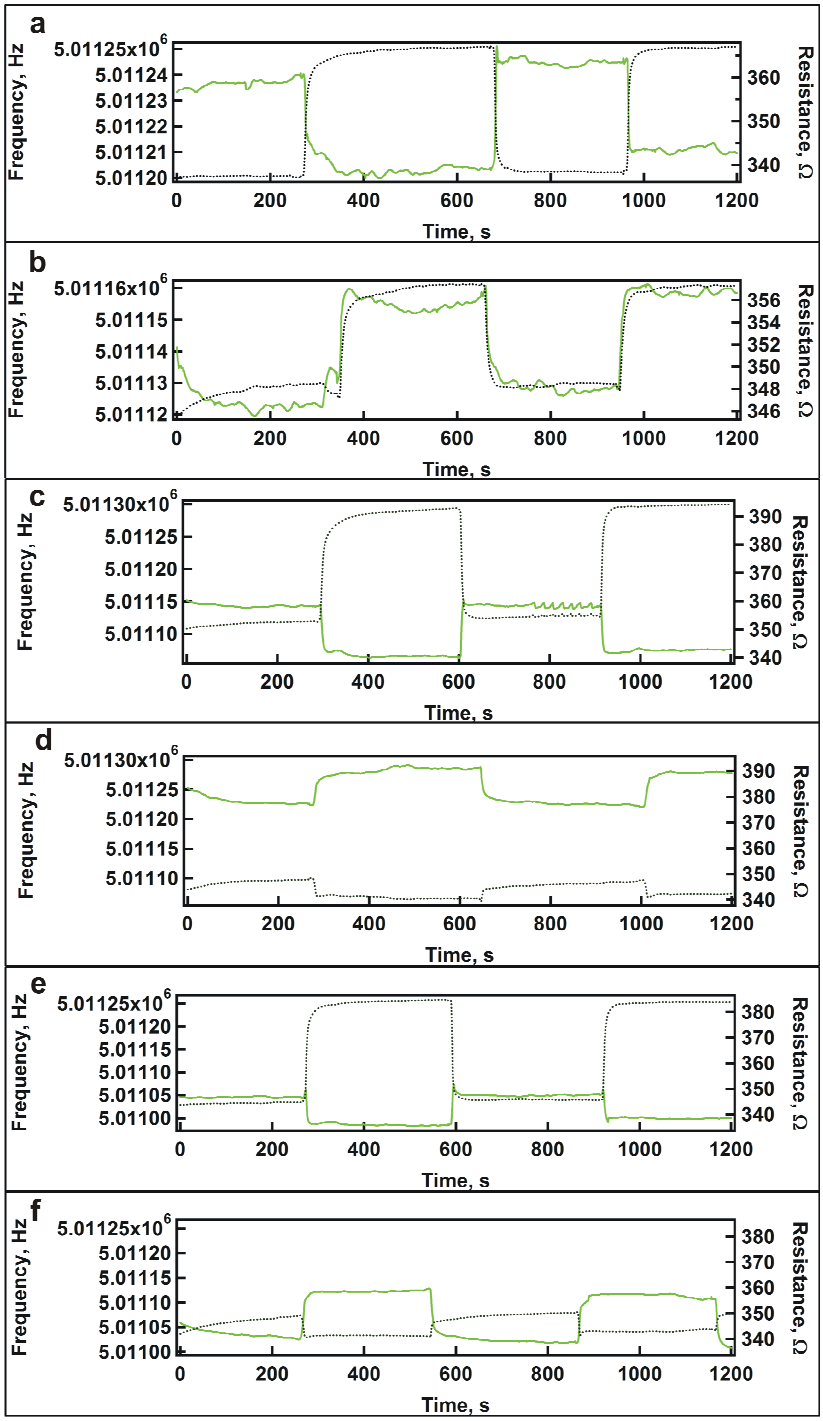

Figure 4.9. QCM time course data for films constructed with 15 000 MW PAH: (a) 0.5-bilayer film (microgel monolayer); (b) 1-bilayer film where PAH forms the top layer; (c) 2.5-bilayer film; (d) 3-bilayer film; (e) 4.5-bilayer film; (f) 5-bilayer film. For all QCM data, the pH starts out at pH 3.0. The light green curve line is the frequency versus time measurements. The black dotted curve represents the resistance vs. time measurements.

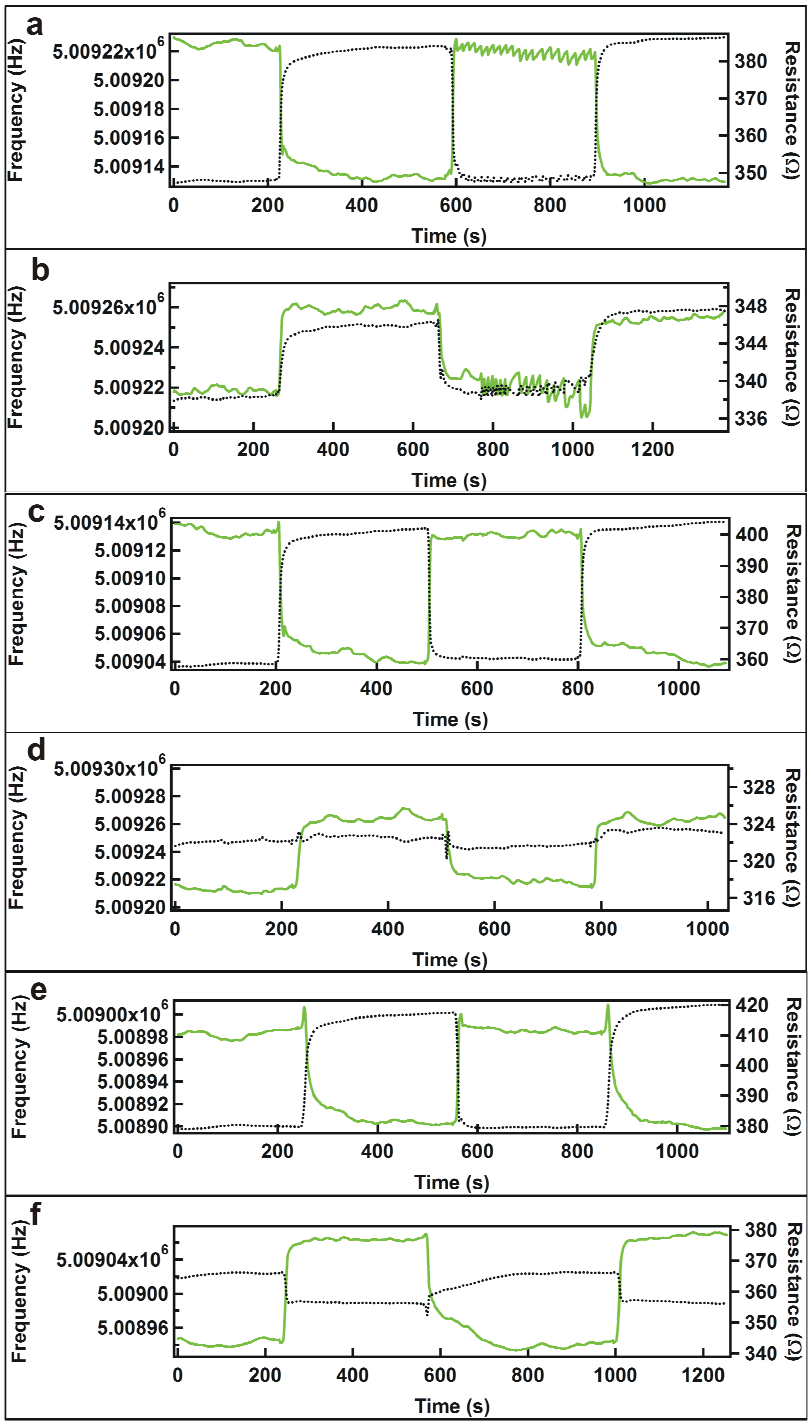

Figure 4.10. QCM time course data for films constructed with 70 000 MW PAH: (a) 2.5-bilayer film; (b) 3-bilayer film where PAH forms the top layer; (c) 3.5-bilayer film; (d) 4-bilayer film; (e) 4.5-bilayer film; (f) 5-bilayer film. For all QCM data, the pH starts out at pH 3.0. The light green solid curve is the frequency versus time measurements. The black dotted curve represents the resistance vs. time measurements.

deswell, however, as evidenced by the overall decrease in film mass and the decrease in film thickness, as measured by AFM.

For a 2.5-layer film, the increase in QCM resistance observed when the pH is increased from 3.0 to 6.5 indicates that the film becomes more dampening (Figure 4.9c). A corresponding *decrease* in frequency is observed at pH 6.5, which suggests an increase in mass at that pH. However, when PAH is added to form a 3-bilayer film, the QCM response changes (Figure 4.9d); an increase in frequency (decrease in film mass) upon raising the pH to 6.5 is observed. This arises from a decrease in the water content of the film due to an increase in the PAH:AAc cross-linking density. This increase in film mass is accompanied by a *decrease* in QCM resistance; the resistance decreases as the film becomes denser and therefore closer in acoustic impedance to the underlying quartz. Conversely, in pH 3.0 solution, the 3-bilayer film swells, resulting in a mass increase (frequency decrease) and an increase in resistance (acoustic dampening). Films comprised of 3.5- to 5-bilayers continue to show the same trends as the 2.5- and 3-bilayer films: upon switching to pH 6.5 a film in which microgels form the top layer swells and increases in resistance, whereas a film in which PAH forms the top layer deswells and becomes more rigid (see Table 1). The trend continues through 5-bilayer films, as shown in Figure 4.9e and 4.9f.

The QCM data representing the films made with 70 000 MW PAH tell a slightly different story. The films composed of 4 layers of particles, 3.5- and 4-bilayer films, behave differently from any films made with 15 000 MW PAH. The 3.5- bilayer film is similar to any film where particles form the top layer; however, when the PAH is added

Table 4.1. Frequency (*f*), resistance (*R*), and calculated change in mass (*m*) for films constructed with 15 000 MW PAH.

Particles on top				PAH on top			
Layer #	ΔR[1] (Ω)	Δf[2] (Hz)	Δm[3] (μg)	Layer #	ΔR[1] (Ω)	Δf[2] (Hz)	Δm[3] (μg)
0.5	28.888	-34.0	0.240	1	9.248	29.7	-0.210
1.5	38.800	-60.5	0.428	2	5.905	37.0	-0.261
2.5	39.832	-73.5	0.519	3	-4.592	55.5	-0.393
3.5	31.794	-14.2	0.100	4	-11.419	85.0	-0.601
4.5	38.896	-56.4	0.399	5	-6.375	96.1	-0.679

Table 4.2. Frequency (*f*), resistance (*R*), and calculated change in mass (*m*) for films constructed with 70 000 MW PAH.

Particles on top				PAH on top			
Layer #	ΔR[1] (Ω)	Δf[2] (Hz)	Δm[3] (μg)	Layer #	ΔR[1] (Ω)	Δf[2] (Hz)	Δm[3] (μg)
0.5	26.335	-48.9	0.346	1	6.313	32.7	-0.231
1.5	57.745	-105.5	0.745	2	6.108	65.4	-0.462
2.5	37.119	-87.9	0.621	3	8.024	32.7	-0.231
3.5	42.237	-89.4	0.632	4	0.822	52.0	-0.368
4.5	39.143	-78.0	0.551	5	-8.795	119.4	-0.843

[1]ΔR is the change in resistance found by subtracting the average resistance at pH 6.5 from the average resistance a pH 3.0.
[2]Δf is the change in frequency found by subtracting the average frequency at pH 6.5 from the average frequency at pH 3.0.
[3]Δm is from calculations using the Sauerbrey equation ($\Delta f = -C_f \cdot \Delta m$, where C_f = 56.6 Hz $\mu g^{-1} cm^2$ for a 5 MHz crystal).

the resistance response is null. There is some perturbation when the solution pH is switched, but there is no change in *R*. These data indicate that the number of effective cross-links formed between the particles exactly compensates the PAH and the particles' desire to swell and become more resistive. When the film reaches 5-bilayers, the bimodal behavior mirrors the response shown by the films made with 15 000 MW PAH at 3-bilayers and higher. One can presume, given the data shown for the films constructed with 15 000 MW PAH (Figure 4.9), that films constructed with 70 000 MW PAH (Figure 4.10) will continue to exhibit the bimodal behavior as the layer number is increased beyond 5-bilayers. Because the bimodal behavior is exhibited only clearly at higher film thicknesses, the data for films constructed with 70 000 MW PAH further indicate that there is some molecular weight dependence with regard to the effective cross-link density and its effect on film properties.

The SPR measurements of all film structures (regardless of the top layer's identity) display an increase in optical density over the same pH range (Figures 4.6 and 4.8). These results, which appear to contradict the QCM results that reveal a film structure-dependent response, can be rationalized by invoking a bimodal swelling mechanism, as depicted in Scheme 4.1. In this scheme, the film undergoes two opposite swelling responses to the pH change. The underlying polymer layers (those below the top microgel layer) become denser at pH 6.5 due to the increase in the PAH:AAc cross-linking interactions. However, the top microgel layer is presumably only pinned to the film by PAH:AAc interactions at the "bottom" of those microgels. Those particles are not condensed or cross-linked with PAH because the next PAH layer has not been deposited. Therefore, the topmost

microgel layer is able to *swell* at pH 6.5 due to deprotonation and subsequent Coulombic repulsion between the AAc groups.[3,13,20]

The QCM frequency data for all PAH-terminated films (full bilayers) show that the *total loss of mass* observed during film deswelling (as the pH is increased from 3.0 to 6.5) increases with film thickness (see Table 4.1 and 4.2). Since the amount of water expelled increases with film thickness, these results indicate that the effect is additive and that the amount of water egress is a function of film volume, as expected. For films where microgels form the top layer, the data indicate that all films increase in mass (frequency decrease) when the pH is increased from 3.0 to 6.5 (the films swell). Conversely, the AFM measurements indicate that the all films with particles on top become thinner at pH 6.5. However, because the frequency changes are accompanied by large increases in resonant resistance, it can no longer be assumed that the films behave within in the Sauerbrey (linear mass-frequency) regime.[6-9] Thus, the frequency changes may not be linearly proportional to film mass. In addition, the measured frequency changes for the x.5-bilayer films (and the associated calculated mass changes) do not show trend with film thickness, suggesting that they may not be representative of the actual mass changes occurring in the films.

These data further suggest that swelling of the top microgel layer is apparently accompanied by a solvent ingress that strongly perturbs the behavior of the QCM crystal. The increase in the QCM resistance, which is an indicator of an increase in acoustic dampening, arises from the increase in Coulombic swelling of the microgels at the film/solution interface. In other words, the poor impedance matching of the swollen microgels to the underlying polymer multilayer (and also the quartz) results in a strongly

dampening material. When the pH is switched back to pH 3.0, the film's PAH:AAc cross-linking density decreases in the bulk of the film causing it to swell (see Figure 4.9d, for example), whereas the microgels in the top layer deswell due to AAc protonation. In essence, this film construct is a "bimaterial" film, where the two materials have opposite pH dependent swelling responses. The QCM is very sensitive to any swelling changes that increase the acoustic dampening and therefore responds strongly to the identity of the topmost layer of the film, which couples the resonator to the surrounding fluid (water). A film composed of complete bilayers (PAH+microgel) produces an assembly that behaves more or less homogeneously, as suggested by the agreement between the SPR and QCM results. However, when the last layer is incomplete (microgels only, no PAH), the bimodal swelling response is observed.

4.5 Conclusions

A combination of probe microscopy, optical, and acoustic methods was used to characterize the build-up of thin films composed of microgels and linear polycations. This combination of techniques has also elucidated the interactions and unusual morphology of the films with respect to pH responsivity. Based on QCM experiments, it was shown that when microgel particles form the top layer, the film responds to changes in pH in a way that is similar to particles in free solution. However, the SPR data tell a different story, namely that the film underneath the particle layer becomes more highly cross-linked when the pH is increased above the pK_a value. When PAH forms the top layer, a homogeneous film behavior is observed using both SPR and QCM. There also appears to be some dependence on the molecular weight of the polycation as to how thick

the film needs to be to exhibit sensitivity to these differences. These observations suggest that the chemical composition can cause the films to act as bi-material or as homogeneous films when exposed to different pH conditions. Thus, these films represent materials of relatively simple design that display a fairly complex responsivity to external stimuli. Such films may be of interest for use in the area of soft actuators.

References

1. Dai, L., "Polymer nanostructures." *Encyclopedia of Nanoscience and Nanotechnology* **2004,** 8, 763-790.

2. Decher, G., "Fuzzy Nanoassemblies: Toward Layered Polymeric Multicomposites." *Science* **1997,** 277, 1232-1237.

3. Sorrell, C. D.; Lyon, L. A., "Bimodal Swelling Responses in Microgel Thin Films." *J. Phys. Chem. B* **2007,** 111, 4060-4066.

4. Pale-Grosdemange, C.; Simon, E. S.; Prime, K. L.; Whitesides, G. M., "Formation of self-assembled monolayers by chemisorption of derivatives of oligo(ethylene glycol) of structure HS(CH2)11(OCH2CH2)mOH on gold." *J. Am. Chem. Soc.* **1991,** 113, 12-20.

5. Serpe, M. J.; Lyon, L. A., "Optical and Acoustic Studies of pH-Dependent Swelling in Microgel Thin Films." *Chem. Mater.* **2004,** 16, 4373-4380.

6. Garland, P. B., "Optical evanescent wave methods for the study of biomolecular interactions." *Q. Rev. Biophys.* **1996,** 29, 91-117.

7. Raether, H., *Surface Plasmons on Smooth and Rough Surfaces and on Gratings*. Springer-Verlag: Berlin, 1988; p 136.

8. Gan, D.; Lyon, L. A., "Tunable Swelling Kinetics in Core-Shell Hydrogel Nanoparticles." *J. Am. Chem. Soc.* **2001,** 123, 7511-7517.

9. Morris, G. E.; Vincent, B.; Snowden, M. J., "Adsorption of Lead Ion onto N-Isopropylacrylamide and Acrylic Acid Copolymer Microgels." *J. Colloid Interface Sci.* **1997,** 190, 198-205.

10. Ward, M. D.; Buttry, D. A., "In Situ Interfacial Mass Detection with Piezoelectric Transducers." *Science* **1990,** 249, 1000-1007.

11. Buttry, D. A.; Ward, M. D., "Measurement of Interfacial Processes at Electrode Surfaces with the Electrochemical Quartz Crystal Microbalance." *Chem. Rev.* **1992,** 92, 1355-1379.

12. Kanazawa, K. K.; Melroy, O. R., "The Quartz Resonator: Electrochemical Applications." *IBM J. Res. Develop.* **1993,** 37, 157-171.

13. Kipling, A. L.; Thompson, M., "Network Analysis Method Applied to Liquid-Phase Acoustic Wave Sensors." *Anal. Chem.* **1990,** 62, 1514-1519.

CHAPTER 5

DEFORMATION CONTROLLED FABRICATION OF BINARY MICROGEL THIN FILMS

5.1 Introduction

A simple approach to multicomponent thin film fabrication involves the use of adsorption kinetics to create films from a binary mixture of particles. With prior knowledge of a particle's solution properties, one can easily predict the number of each particle type that will be adsorbed based on the jamming limit determined by the random sequential adsorption (RSA) model.[1-6] The basic model for RSA in *d* dimensions states that:

a) the objects are placed at random in *d*-dimensional volume,

b) there is no overlapping of the objects,

c) there is no lateral surface diffusion following adsorption, and

d) there is no desorption from the system, so that when the jamming limit is reached the process ceases.[2]

Based on this model, many simulations have been performed of hard disks adsorbing at a surface and the surface coverage (θ) of the jamming limit is principally agreed to be $\theta = 0.547$.[1,2] Schaaf and Talbot have determined that for proteins the jamming limit is slightly higher at $\theta = 0.5531$.[5] They also investigated a two component case of small (r_s) and large (r_l) disks where $r_s << r_l$. In these studies, they showed that the larger disks are prevented

from reaching a point where their asymptotic kinetics are applicable and the smaller particles will continue to fill in until they reach a jamming limit that corresponds to 0.547 of the available space.[1] A similar set of studies was performed by Meakin and Jullien[6] who calculated surface coverage from a range of mixtures consisting of disk size ratios (R) of r_l to r_s from 1.125 to 8 and feed stock fractions of the smaller disks, f, from 0.016 to 0.875. They showed that in a binary system of hard disks where R is greater than 1.5, the total surface coverage, θ, is dependent on how many units of the smaller component are fed to the surface; and furthermore, when the larger disk dominates the feed stock, the total surface area covered is higher than the 2-d jamming limit of 0.547. They calculate that as $f \rightarrow 0$, θ_T is 0.7945. This analysis assumes that the large disks will fill the system to their jamming limit and the smaller disks will fill the interstices to the jamming limit of 0.547 within the remaining space, which gives a θ_s value of 0.2478.

Random sequential adsorption of polymer microparticles has also been studied experimentally, largely using hard sphere polystyrene particles.[7-9] These studies have shown that the calculated models for hard disks and spheres translates easily to a physical hard sphere experiment. In this investigation, we are interested in the simultaneous adsorption of two disparate "soft" building blocks in the assembly of a microgel monolayer film in two dimensions. Even though published theory and experimental results indicate that these studies should result in statistically predictable films, the use of a soft material injects additional considerations. Specifically, how do we treat the adsorption of two particles with nearly identical solution diffusion coefficients, but very different surface footprints and hence differential blocking behavior? The

Scheme 5.1. Schematic depiction of film formation and AFM characterization

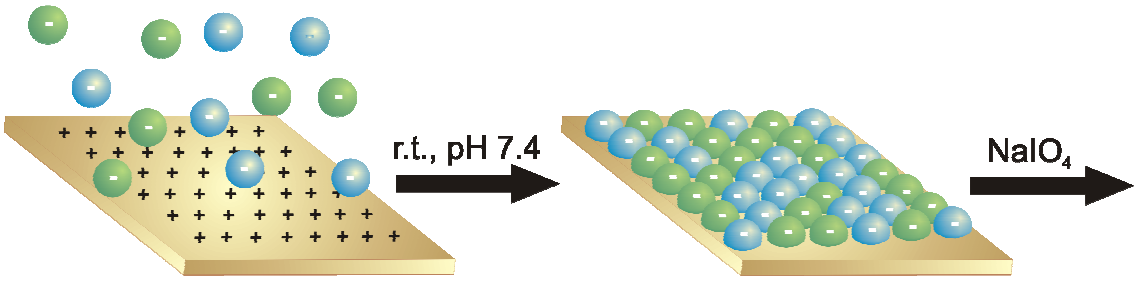

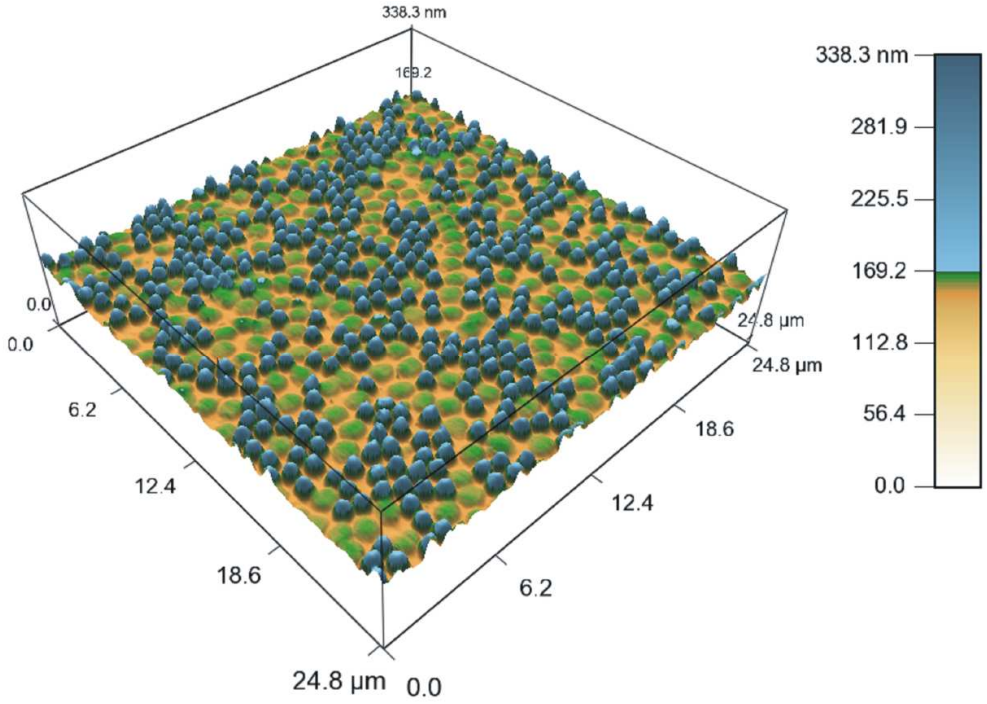

questions that now arise are a) how are the two microgels represented in the film, and b) is their representation in the film predictable by simply applying the known values of the RSA model?

Polymer thin films have tremendous utility for applications in biomedical devices,[10] sensors,[11] and optical materials.[12]Specifically, polyelectrolyte based assembly of thin films has become an extremely popular method for polymer thin film construction during the past 15 years.[13,14] Because of the remarkable versatility in film structure that is available using this method, a significant amount of work remains to be done in this area.[15] This chapter examines the apparently simple problem of polyelectrolyte microgel adsorption to a planar substrate from binary microgel dispersions. The results show that unlike hard spheres, soft particulate building blocks can strongly influence film assembly through simple differences in deformation following surface adsorption (Scheme 5.1).

For these studies, two types of core/shell microgel particles with similar diffusion properties in solution – but different core cross-linking chemistries and softness – were used to create thin films.[16] Both microgel types have anionic shells to enable adsorption to a cationic substrate, with one of the microgels having a degradable hydrogel core, while the other has a non-degradable core. Atomic force microscopy combined with image analysis was used to quantitatively analyze the binary microgel thin films, and then the results were compared to predictions made using the RSA model. The degradable core component was originally included in one of the particle types to allow unambiguous discrimination using AFM between the two (identically sized) particles. As seen below, this added degree of complexity turned out to be unnecessary due to the dramatic differences between the two particle-surface interaction modes observed.

Nonetheless, these studies are important in our efforts to gain predictive power over the assembly of multicomponent microgel thin films for applications in biomaterial coatings, as we have described previously.[17,18] Using hollow or degradable core/shell particles further increases the utility of the microgel thin films for potential applications in drug encapsulation and release,[19,20] as well as to add chemical handles for surface chemoligation.

5.2 Experimental Section

Reagents were purchased from Sigma-Aldrich unless otherwise specified. The monomer *N*-isopropylacrylamide (NIPAm) was recrystallized from hexanes (J.T. Baker) and dried under vacuum prior to use. The cross-linkers *N,N'*-methylenebis(acrylamide) (BIS) and *N,N'*-dihydroxyethylene-bis-acrylamide (DHEA), co-monomer acrylic acid (AAc), and initiator ammonium persulfate (APS) were used as received. Buffer components sodium dihydrogen phosphate monohydrate (Fisher Scientific), maleic acid, formic acid, acetic acid, 3-(*N*-morpholino)propanesulfonic acid (MOPS), sodium chloride (Mallinckrodt), and sodium hydroxide (Fisher Scientific), and sodium periodate (Acros) were used as received. The surface modification reagent 3-aminopropyltrimethoxysilane (APTMS, United Technologies, Inc.) was used as received. Glass substrates were 24 × 24 mm VWR cover glass and were obtained from VWR International. Ethanol (95% and absolute) was used as received. Water used was house distilled, then deionized to a resistance of at least 18 MΩ (Barnstead Thermolyne E-Pure system), and then filtered through a 0.2 μm filter.

5.2.1 Microgel Synthesis

pNIPAm microgels with BIS cross-links **(1)**. Microgel cores were synthesized via aqueous free-radical precipitation polymerization as previously described,[21-23] using 70 mM total monomer concentration. Core particles with non-degradable (BIS) cross-links had a molar composition of 98% NIPAm and 2% BIS. The polymerization feed was composed of 0.7765 g (6.862 mmol) NIPAm and 0.0309 g (0.2 mmol) BIS dissolved in 99 mL deionized water. The initiator, 0.0229 g (0.1 mmol) APS, was separately dissolved in 1 mL deionized water. The polymerization was allowed to proceed for 4 h at 65 ± 2 °C to give microgel product **1**.

pNIPAm microgels with DHEA cross-links **(2).** The other core particle comprised 95% NIPAm and 5% DHEA (molar percentage). The polymerization feed was composed of 0.7528 g (6.652 mmol) NIPAm and 0.0711 g (0.3552 mmol) DHEA dissolved in 99 mL deionized water. The synthesis was initiated with 0.0228 g (0.1 mmol) APS in 1 mL of deionized water and carried to completion under the same conditions described above to yield microgel product **2**.

pNIPAm-co-AAc shell with BIS cross-links (**3**). Each of the core particles was used in a seed-and-feed shell synthesis, as previously described.[22] Approximately 40 mL of the reaction product suspension (BIS cores or DHEA cores) from above was diluted with ~59 mL of water. The shells were composed of 88% NIPAm, 2% BIS, and 10% AAc and were attached to the cores via aqueous free-radical precipitation polymerization as previously described,[22] using a 40 mM total monomer concentration. For shell syntheses using microgel core **1** as the seed, the polymerization feed was composed of 0.3991 g (3.527 mmol) NIPAm, 0.0134 g (0.0869 mmol) BIS, and 26 μL (0.3789 mmol) AAc

dissolved in the 99 mL core microgel dispersion. The initiator, 0.0235 g (0.103 mmol) APS, was separately dissolved in 1 mL deionized water. The reaction was heated to 65 ± 2 °C and allowed to proceed for 4 hours to give microgel product **(1)3**. The same synthesis was repeated for the microgel core **2** using 0.3988 g (3.524 mmol) NIPAm, 0.0137 g (0. 0889 mmol) BIS, 26 μL (0.3789 mmol) AAc, and 0.0231 g (0.101 mmol) APS to give microgel product **(2)3**.

After applying the standard purification methods (Chapter 3), the lyophilized white powders were weighed and resuspended in distilled, deionized water to a concentration of 0.0025 g/mL.

5.2.2 Light Scattering Analysis

Dynamic light scattering (DLS) has been used as a tool for determining mean particle size and particle size distributions[24,25] and has been used for similar microgel systems. The hydrodynamic radii (R_h) and diffusion coefficients (D) of the particles were determined by DLS (Protein Solutions, Inc.) prior to their use for thin-film fabrication. Briefly, a dilute microgel solution in pH 7.4 PBS buffer (20 mM, 100 mM ionic strength) was added to a cuvette and inserted into the DLS cuvette holder. The microgels were measured at 23 °C in the same pH 7.4 PBS buffer (20 mM, 100 mM ionic strength) used for film assembly.

Additional dynamic light scattering measurements at a scattering angle of 158° were taken using a DynaPro Plate Reader (Wyatt Technologies, Inc., Santa Barbara, CA). For each particle, analysis was performed using samples at pH 7.4 as above by taking five measurements of ten acquisitions each.

Table 5.1. Particle properties for microgel products **(1)3** and **(2)3**

Microgel	Hydrodynamic radius, R_h (nm)[1*]	Radius of gyration, R_g (nm)[2]	Radius on surface, R_s (nm)[3]	Diffusion, coefficient, D (cm^2/s)[1]	Electrophoretic Mobility (μm·cm/V·s)[4]	Molar mass, M_z (g/mol)[2]	Number density, N (#/mL)[2]
(1)3	348 ± 67	223 ± 21	489	6.58e-9	-0.913 (±0.0508)	1.7e+9 (±0.08e+9)	8.9e+11
(2)3	360 ± 86	229 ± 27	619	6.35e-9	-0.879 (±0.0280)	3.9e+8 (±0.6e+8)	3.9e+12

[1]Determined by dynamic light scattering at 90°.
[2]Determined by static light scattering.
[3]Determined by atomic force microscopy image analysis.
[4]Determined by electrophoretic light scattering.
[*]DLS at 158° gives a R_h of 366 nm (p.d. = 9.4%) for **(1)3** and 379 nm (p.d. = 16.4%) for **(2)3**. Sizing using particle tracking gives a
D_h of 730 ± 20 nm for **(1)3** and 748 ± 87 nm for **(2)3**.

A NanoSight LM20 particle tracking analysis system (NanoSight, Ltd., Salisbury, U.K.) was also used for particle analysis to provide additional confirmation of the solution diffusion coefficients. The LM20 is a laser light scattering instrument wherein the particles are tracked by optical microscopy to yield maps of particle position vs. time, which can then be used to determine particle diffusion coefficients. The samples from the DLS plate reader were directly injected into the LM20 sample holder and 3 movies of each particle solution were taken and analyzed to obtain hydrodynamic diameter (D_h).

The radii of gyration (R_g), molar masses (M_z), and number densities (n) of the particles were determined by multi-angle laser light scattering (MALLS, DAWN EOS, Wyatt Technologies, Inc.) and differential refractive index measurements (dRI, OptiLab rEX, Wyatt Technologies, Inc.) prior to their use for thin-film fabrication. MALLS detection following asymmetric field flow fractionation (AFFF) was used to determine the z-average radii (R_z) for all particles.[26,27] For all separations, a cross flow of 1.0 mL/min was used. The MALLS detector is equipped with a Peltier device to maintain a flow cell temperature of 25 °C, and it collects scattered light from 18 different fixed angles to determine the R_z of the particles. ASTRA 5.3.1.15 software was used to determine R_z and M_z values with the Debye fit method.[28] The particle size and molar mass were determined using a known concentration of particles in pH 7.0 10 mM PBS buffer (20 mM ionic strength): for the BIS core/shell particles the concentration was 6.25 x 10^{-5} g/mL; for the DHEA core/shell particles the concentration was 1.25 x 10^{-4} g/mL. The *dn/dc* for each type of particle was determined in distilled, deionized water by using a set of seven dilutions with a concentration range of 2.5 x 10^{-5} g/mL to 3.75 x 10^{-4} g/mL.

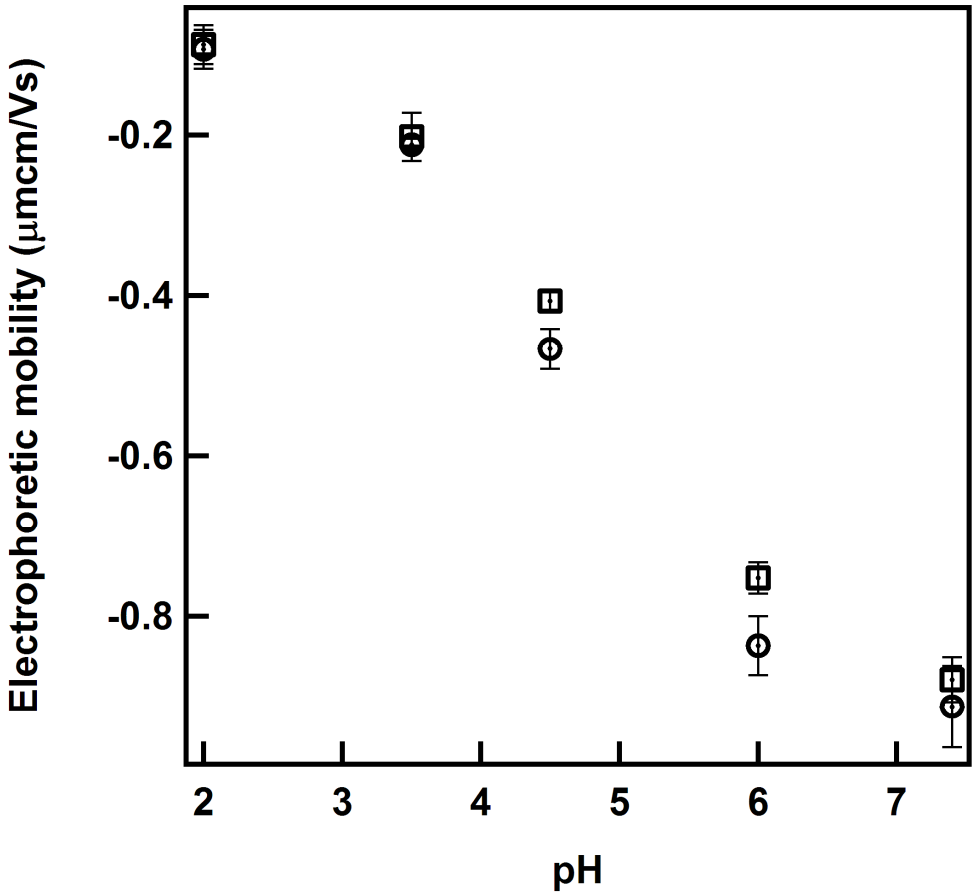

Figure 5.1. Analysis of particle electrophoretic mobility as a function of pH. Circles represent microgel **(1)3**, squares represent microgel **(2)3**. Error bars represent the standard deviation from 3 measurements per sample.

The samples for *dn/dc* determination were prepared according to the guidelines set out in the OptiLab rEX hardware manual.

The electrophoretic mobility for each particle was determined by using a Malvern Instruments Zetasizer. Samples were prepared by diluting 50 μL of each 0.0025 g/mL particle stock solution in pH 2.0 maleate buffer, pH 3.5 formate buffer, pH 4.5 acetate buffer, pH 6.0 MES buffer, and pH 7.4 MOPS buffer (10 mM buffer component concentration, 10 mM ionic strength). The values for each particle represent an average of three measurements consisting of 20 acquisitions per measurement.

5.2.3 Film Preparation

Glass coverslips (24 mm x 24 mm) were cleaned using Ar plasma (Harrick Plasma, Ithaca, NY) for ~15 minutes. Each cleaned slide was functionalized by exposure to a 1% solution of 3-aminopropyltrimethoxysilane (APTMS) in absolute ethanol for ~2 h.[29] The functionalized slides were rinsed with ethanol (95%), and then stored for up to one week in absolute ethanol. Before use, each slide was rinsed with ethanol and dried under a stream of N_2. The slides were cut to ~1 cm x 0.5 cm rectangles using a glass-cutting stylus. A description of the surface characterization of APTMS functionalized surfaces is provided in Chapter 2.

For the experiments designed to determine the jamming limit, the 0.0025 g/mL stock solution of microgel **(1)3** was diluted 1:10 in pH 7.4 buffer. The 0.0025 g/mL microgel **(2)3** stock solution was first diluted by taking 1 mL of the stock and adding 1.15 mL of nanopure water to ensure that the number density of the dispersion (determined from MALLS) was the same as the microgel **(1)3** solution. The microgel **(2)3** stock dilution was then diluted further 1:10 in pH 7.4 buffers. The buffers used were prepared to be pH

7.4 with 1 mM MOPS (1 mM ionic strength), 10 mM MOPS (10 mM ionic strength), and 10 mM PBS (50, 100, and 200 mM ionic strength). One cut cover slip was placed into each solution for 48 hours. The samples were gently rinsed with water and dried under a slow stream of N_2.

For the binary adsorption experiments (depicted in Scheme 5.1), the 0.0025 g/mL stock solution of microgel **(1)3** was diluted 1:5 in pH 7.4 PBS buffer (20 mM, 100 mM ionic strength). The 0.0025 g/mL microgel **(2)3** stock solution was first diluted by taking 1 mL of the stock and adding 1.15 mL of distilled, deionized water to ensure that the number density of the dispersion (determined from MALLS) was the same as the microgel **(1)3** solution. The microgel **(2)3** stock dilution was then diluted further 1:5 in pH 7.4 PBS. For the binary adsorption experiments, ratios (1:0, 9:1, 7.5:2.5, 1:1, 2.5:7.5, 1:9, and 0:1) of these two solutions were mixed in 1 mL volumes in a plastic 48-well plate (Greiner Bio-One Cellstar, No. 677 180). One cut cover slip was placed into each mixture for ~1.5 h. The slides were dipped into 1 mL of buffer and then placed into a 10 μM solution of $NaIO_4$ in buffer (created by diluting 10 μL of a stock solution of 1 mM $NaIO_4$ into 0.99 mL of pH 7.4 PBS) overnight.

Addition of $NaIO_4$ to the films leads to controlled degradation of the particle core in microgel **(2)3** by cleavage of the 1,2-glycol bond in DHEA.[30] The product of the reaction comprises two aldehyde groups from the diol, and the resulting polymer chains are free to partition out of the shell. The slides were then soaked in 1 mL of pH 7.4 PBS for ~2 hours. A control slide using a 1:1 mixture of particles was made but not subjected to periodate degradation. It was was exposed to pH 7.4 PBS solutions for the same periods

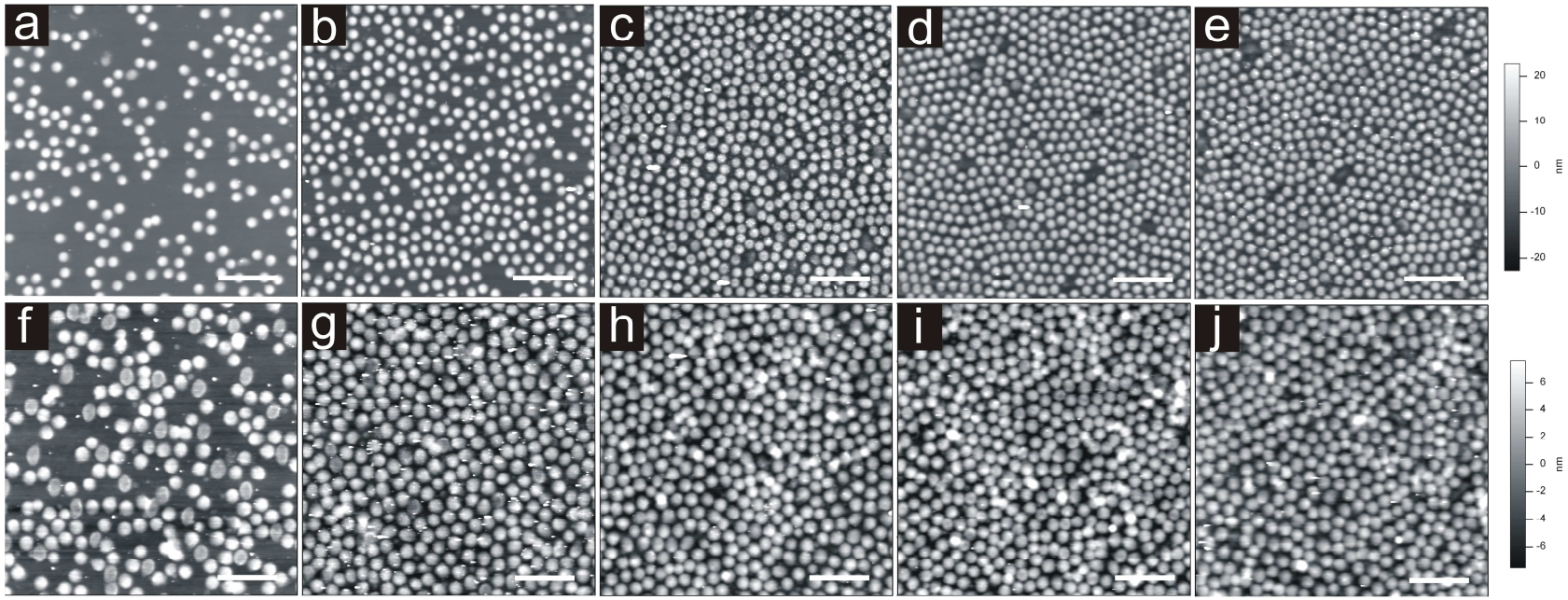

Figure 5.2. AFM images of the jamming experiment samples for microgel **(1)3** (images a-e) and microgel **(2)3** (images f-j). From left to right, the ionic strength of film preparation solutions was 1 mM, 10 mM, 50 mM, 100 mM, and 200 mM. Scale bars are 5 μm.

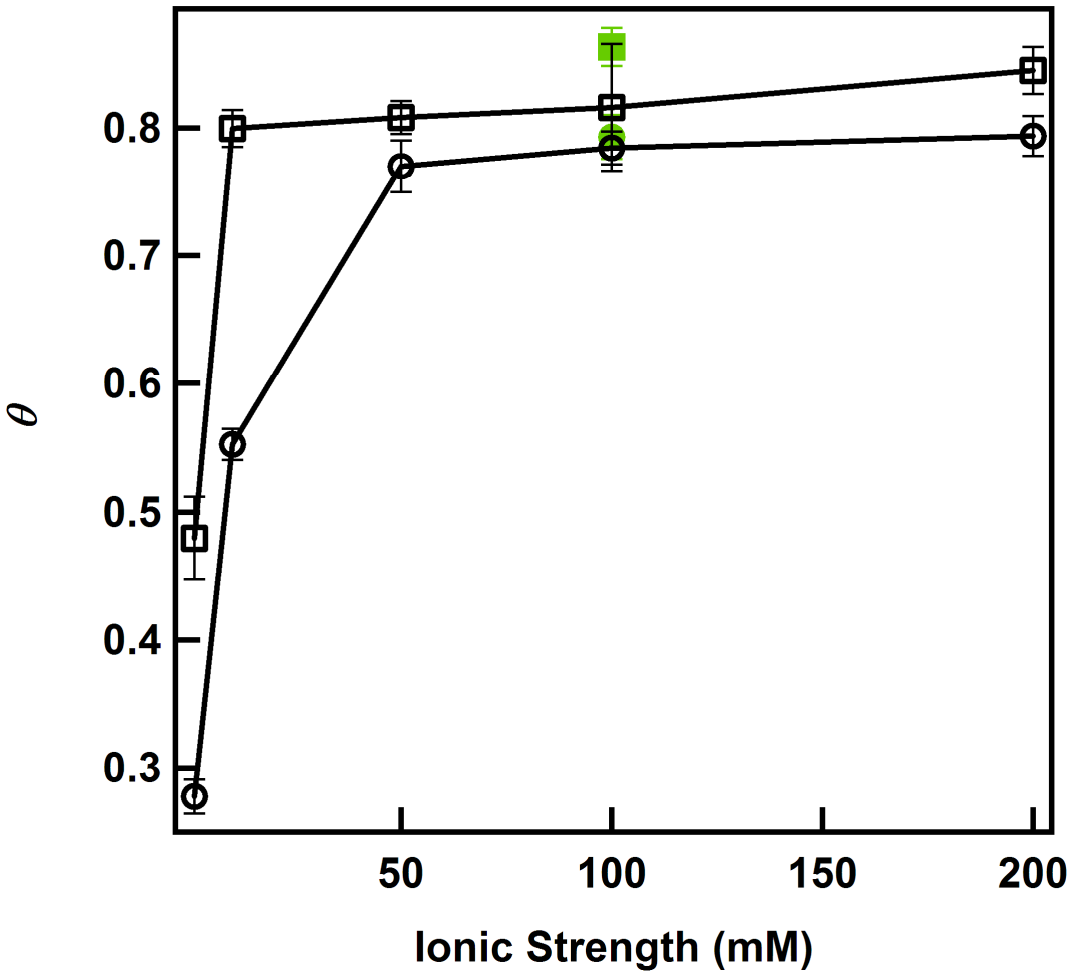

Figure 5.3. Graph of the surface coverage (θ) jamming limit as a function of ionic strength. The circles represent microgel **(1)3** and the squares represent microgel **(2)3**. Error bars represent the standard deviation of the average value obtained from five images. The solid green symbols represent the surface coverage values from the single component samples ($f = 0$ or 1) for each particle type obtained in the associated "binary" adsorption experiments.

of time, however. The slides were gently rinsed with water and dried under a slow stream of N_2.

5.2.4 Atomic Force Microscopy Measurements

AFM data were taken in air in AC mode on an Asylum Research MFP-3D instrument (Santa Barbara, CA). Imaging and analysis were performed using the Asylum Research MFP-3D software running in the IgorPro environment (WaveMetrics, Inc., Lake Oswego, OR).

Nanoworld FM-10 Pointprobe cantilevers were used (k = 2.8 N/m, f_0 = 75 kHz) to image the films. To prepare AFM samples, the film-coated substrates (dried as described above) were attached by adhesion to a standard microscope slide using Leitsilber 200 Silver Paint (Ted Pella, Inc., Redding, CA). Each image was 25 μm x 25 μm. Five images of each film were taken at different locations of the film surface to allow statistically meaningful particle counting.

A statistical analysis of the particles in each image was done by using a particle count in conjuction with the particle-size calculator developed for the MFP-3D software by Stefan Vinzelberg (Atomic Force F&E GmbH, an AR affiliate). The particle count and size calculations are based on a mask created in the image analysis module in the MFP-3D software provided with the instrument. The microgel **(1)3** (non-degraded) particles displayed sufficient contrast in height mode from the rest of the sample to be subjected to this analysis. The microgel **(2)3** (degraded) particles were counted manually. Surface area calculations were performed using the masking and image analysis capabilities built into the MFP-3D software and were applied in the same way to each image.

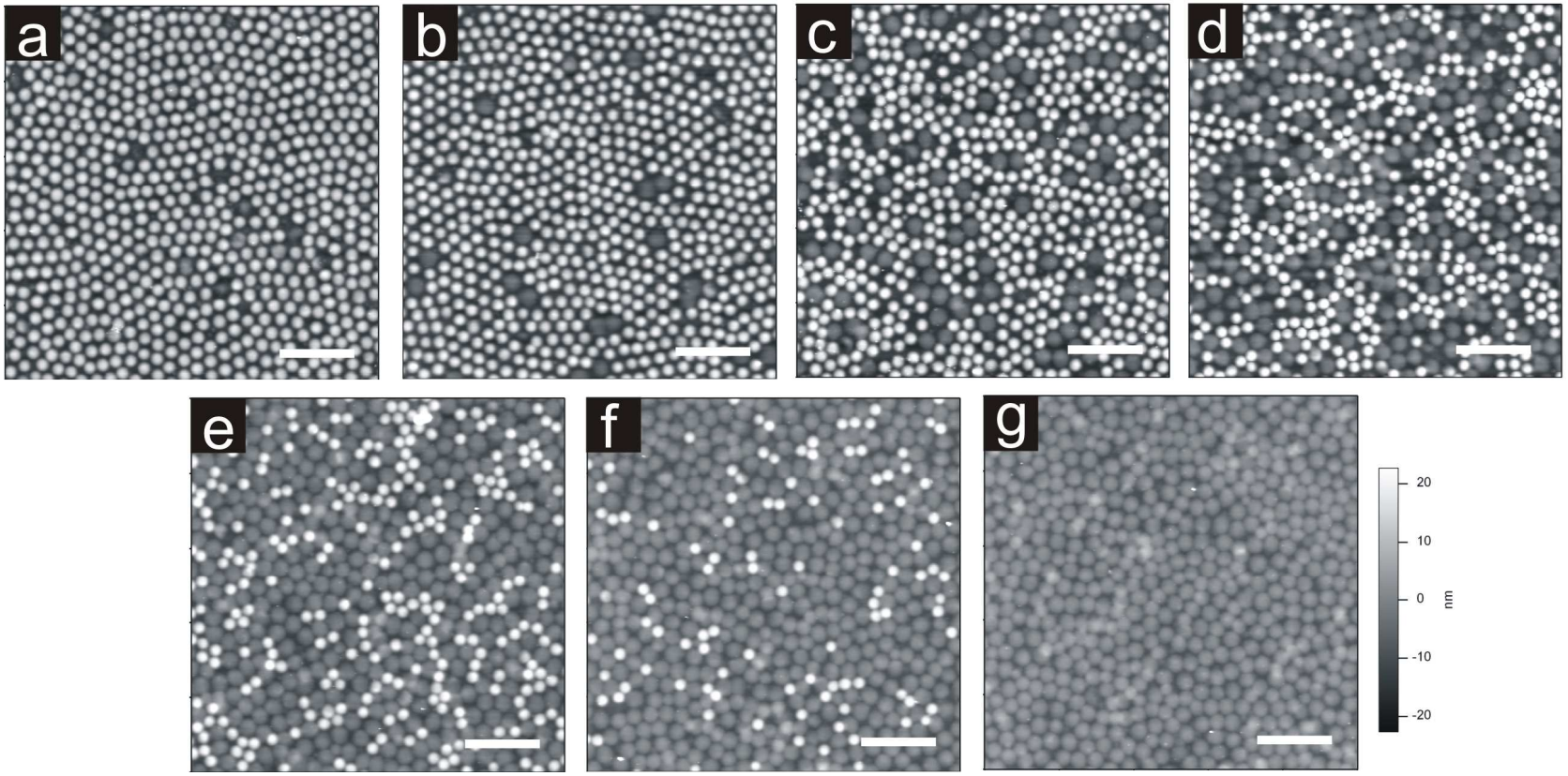

Figure 5.4. AFM images of binary microgel monolayer films. Films represented are formed from mixtures of microgels **(1)3** and **(2)3** in the following ratios: a) 1:0, b) 9:1, c) 7.5:2.5, d) 1:1, e) 2.5:7.5, f) 1:9, and g) 0:1. All images are 25 μm x 25 μm. Scale bars are 5 μm. The z-scale bar has a range of 45 nm and is the same for all of the images.

5.3 Results

The particle properties as determined by dynamic and static light scattering and atomic force microscopy are outlined in Table 5.1. Light scattering measurements show that the particles are similar in size and diffusion coefficients. Microgel **(1)3** had a hydrodynamic radius ~350 nm compared to that of **(2)3,** which was ~360 nm. Note that each light scattering technique produces slightly different values, presumably due to differences in the experimental conditions (e.g. scattering angle) and analysis methods (e.g. real-space vs. reciprocal space determination). Nonetheless, the relative differences between the two populations are consistent and the sizes of each fall within the polydispersity of the other, indicating that a mixture of these particles can be treated as a single component system where the ratio (R) of the relative sizes of **(1)3** to **(2)3** was ~1. At pH 7.4, the particles' diffusion coefficients (D) were ~6.6e-9 cm^2/s and ~6.4e-9 cm^2/s, and their electrophoretic mobilities were -0.913 and -0.879 μm·cm/V·s, respectively. Given these particle sizes together with an image size of 625 μm^2, approximately 850-900 particles should be present in each image if one assumes a particle footprint commensurate with a non-deformed cross-section and a jamming limit of 0.547 for a single component system. Because there is no real difference between these particles in solution, there is little reason to believe that one will clearly dominate over the other based on their solution diffusion properties. It is therefore also reasonable to assume that the film composition can be directly predicted from solution composition. All films were analyzed by AFM. A representative image for each film formed from binary mixtures of particles is shown in Figure 2.4. All of the images show good film coverage and one can

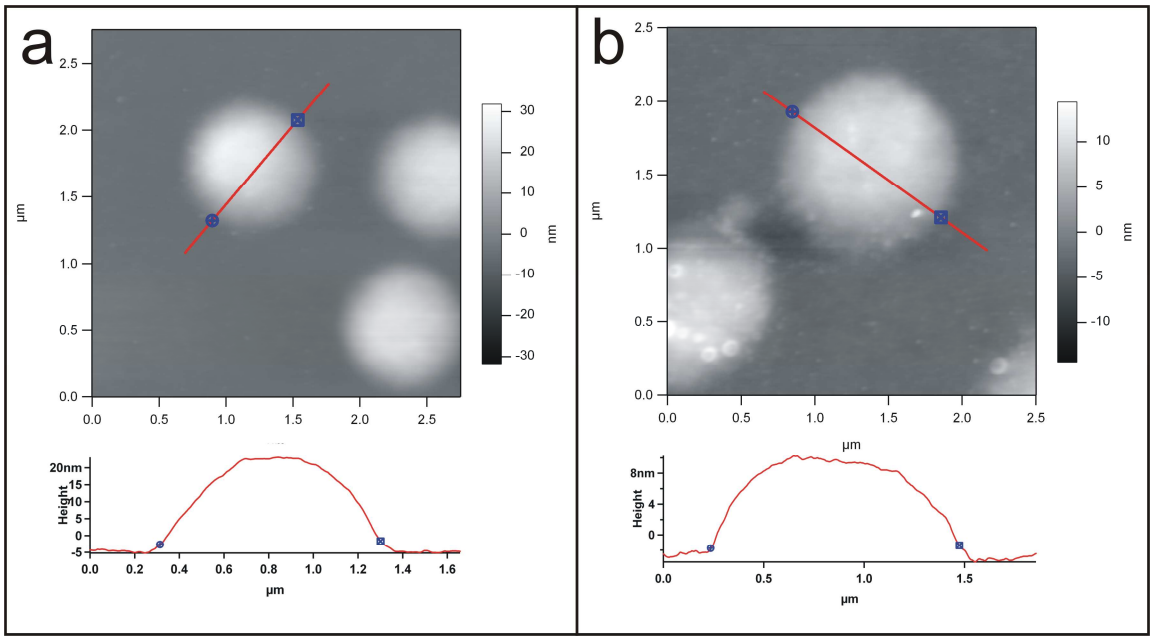

Figure 5.5. Size analysis for a) microgel **(1)3** and b) microgel **(2)3** by AFM. Compared to line analyses in all images, the sizes are consistent with the surface area calculations. A close-up is shown here to emphasize the size difference of the two particles. There will be some inaccuracy in the measured size because of tip convolution artifacts; all of the data have the same bias since the same tip geometries were used throughout, including the data analyses.

Table 5.2. Film composition results determined by atomic force microscopy

f, **(1)3** to **(2)3** in solution	# average **(1)3**	# average **(2)3**	θ **(1)3**	θ **(2)3**	Percent of total θ **(1)3**	Percent of total θ **(2)3**
1.0	669	0	0.781	0	100	0
0.9	649	19	0.757	0.073	91.2	8.77
0.75	551	86	0.644	0.184	77.7	22.3
0.5	429	204	0.501	0.359	58.3	41.7
0.25	243	356	0.284	0.569	33.3	66.7
0.1	107	443	0.124	0.703	15.0	85.0
0	0	556	0	0.863	0	100

clearly see a contrast between the two types of particles. It is apparent from the images that particle populations in the films are skewed to microgel **(1)3** and that the two populations of particles are significantly different from each other once they have adhered to the interface. Figure 5.4 also indicates that some of the particles, particularly those at lower values of *f*, will deform to pack more closely at the interface. In all films (except in the case having 100% of each particle type) microgel **(1)3** has a greater number of particles than expected based on its percentage in solution. The particle counts shown in Table 5.2 confirm this. This result is more clearly illustrated in Figure 5.8, which shows that the total numbers of particles are significantly lower than predicted. Figure 5.8 also reveals that the overall numbers of particles increases as the fraction, *f*, of **(1)3** increases. This is not surprising since the footprint of that particle is smaller and

more particles fit in the image area, in effect keeping the total surface coverage relatively constant for all values of *f*.

If we consider film composition and surface coverage and use the film obtained from the 1:1 dispersion as an example, the number of surface particles for **(1)3** is 429 on average, while the **(2)3** portion of the film only has 203 particles on average. This means that 67.8% of the total number of particles in the film comprise microgel **(1)3**, which is almost 18% higher than the expected 50%. However, if one instead looks at the *percent surface coverage* for each film, Figures 5.6b and 5.6c show that the actual percent surface coverage for each population more closely matches the prediction that the solution composition will dictate the film composition. In the 1:1 film case, the surface coverage is high at 58.2% for **(1)3**, but is more closely correlated with the expected value of 50%. This result means that even though microgel **(1)3** is represented in higher numbers, **(2)3** takes up more space on the surface per particle (Table 5.1 and Figure 5.5). There is a small decrease in surface coverage which is commensurate with the smaller footprint of **(1)3**. Figure 5.6a closely mirrors data for binary disk adsorption presented by Meakin and Jullien, where regardless of the relative disk sizes, the surface coverage is biased to the smaller disk, with the two disks occupying the same relative surface coverages at $f \approx 0.35$.[6] However, unlike their studies, in our work the jamming limit for the binary system does not decrease to meet the single component jamming limit (0.547) as $f \rightarrow 1$ because our particles spread once they interact with the surface.

The data in Figure 5.3 (images shown in Figure 5.2) confirm that the particles do reach the jamming limit under the given experimental conditions. These data also show

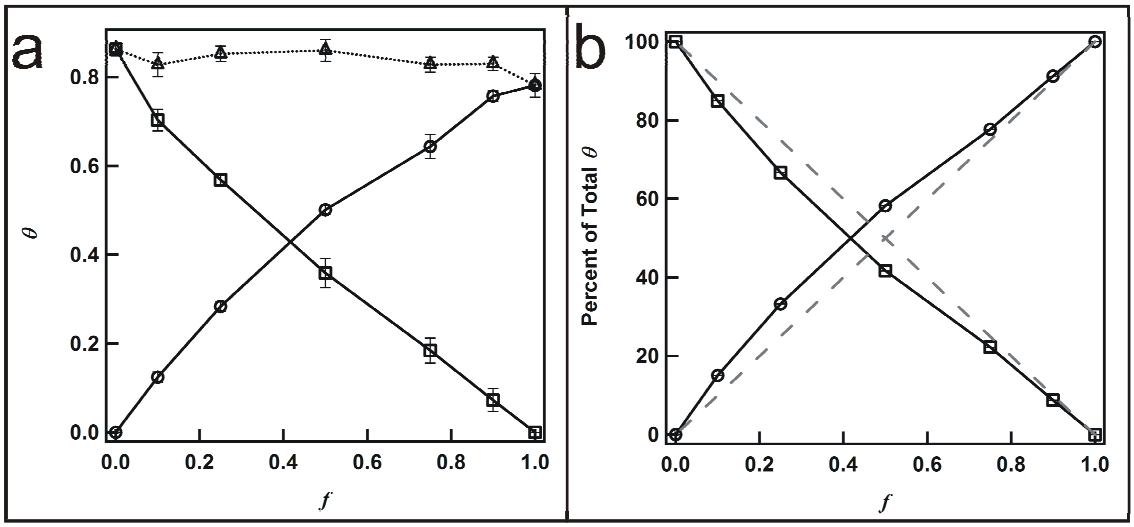

Figure 5.6. Surface coverage of each particle in the films. Solid curves with circles represent microgel **(1)3**, solid curves with squares represent microgel **(2)3**, dotted curves with triangles represent total values. a) surface coverage, θ, plotted against the adsorption solution composition, f; and b) percent surface coverage relative to the total surface coverage. The dashed curves are the predicted results based on the original solution composition and ignoring blocking effects. Error bars represent the standard deviation of the average values obtained from five images.

that the two particles have similar jamming limits and that the experimental surface coverage correlates with the surface coverage in the jamming experiment (Figure 5.6b). The jamming limit for microgel **(1)3** is lower than that for **(2)3**, but both jamming limits hover around ~0.8. The total surface coverage for the binary films decreases within this range as $f \rightarrow 1$, as depicted in Figure 5.6a.

Figure 5.7 compares a non-degraded binary film to a periodate degraded binary film. Both films were created from a 1:1 solution of the two microgels under study. Microgel **(2)3** looks significantly different from microgel **(1)3** regardless of the degradation of the DHEA cross-links. This difference in appearance is also indicated by the difference in the radial size (i.e. footprint) of the particles on the surface (R_s) as shown in Table 5.1. Nonetheless, the height profiles shown in Figure 5.7 clearly illustrate that a degradation process is indeed taking place, as the height profile of microgel **(2)3** significantly changes in relation to microgel **(1)3** following the periodate ion treatment.

5.4 Discussion

The most striking result that the experimental results do not match the predictions of the single-component RSA model, but more closely mirror the binary RSA model. These results lead to the conclusion that the single largest contributing factor is the difference in the deformability of the particles and their binary behavior at an interface, which is contrary to their monomodal behavior in solution. The difference between the surface and solution morphology is observable in several aspects of the data, as discussed below.

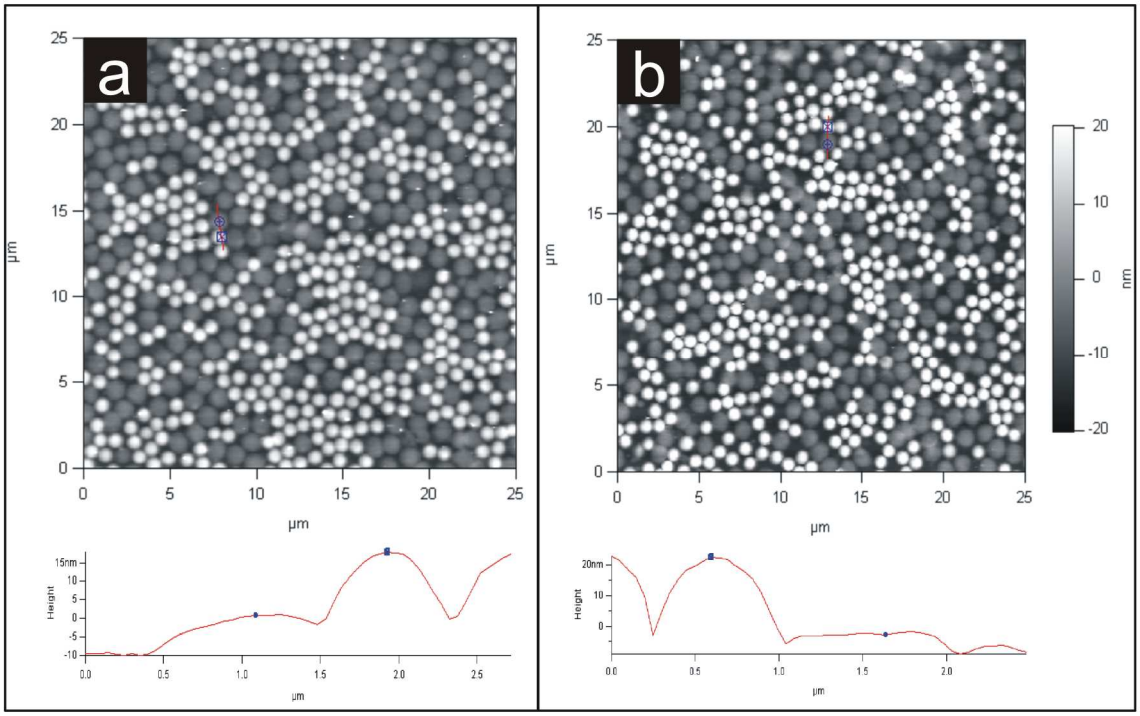

Figure 5.7. Representative line profiles for (a) a non-degraded film and (b) a degraded film. Insets show representative line profiles. AFM image analysis gave Δz = 17.9 ± 2.2 nm in (a) and Δz = 25.9 ± 1.6 nm in (b) for the height difference between microgels **(1)3** and **(2)3**. Fifteen measurements were taken in each image to determine the mean height difference and standard deviation. Scale bars are 5 µm for the full-size images and 1 µm for the insets. The z-scale bar has a range of 45 nm and is the same for all images.

In general, the overall low particle numbers arise from the increased radius of the particles at the interface compared to the radius in solution. Our initial calculation assumed that the surface footprint should be identical to the particle cross-section in solution. However, if the particle size increases when the particles adsorb on the surface, the particles would take up more space on the surface than predicted, thereby decreasing the total particle number density. Additionally, the particles are negatively charged at pH 7.4. Coulombic repulsions between the particles, which would increase their spacings and reduce the number of particles reaching the surface,[31] are also not taken into account in the single-component model.[2] At the high ionic strength of the experiments, this repulsive force is reduced because the ions in solution provide more shielding to the charged acrylic acid groups on the particles, thereby allowing them to come closer to their neighbors than at lower ionic strengths (Figures 5.2 and 5.3). Therefore, while particle deformability is a factor in the differences between our results and naïve predictions, it is unlikely that Coulombic repulsion plays a large role in these differences due to the relatively high ionic strength used in our experiments.

As shown in Table 5.1, the two microgel types studied here are similar in their sizes and diffusion coefficients, but the molar mass data indicate that the particles are significantly different in terms of their density and/or morphology. The molar mass for **(2)3** is approximately half of the molar mass for **(1)3**, indicating that the polymer density in the particle is significantly lower for microgel **(2)3**. Viewed another way, for identical wt% solutions, the particle number density for **(2)3** is 3.9×10^{12} particles/mL, which is four times the particle number density for **(1)3** (8.9×10^{11} particles/mL). The differences

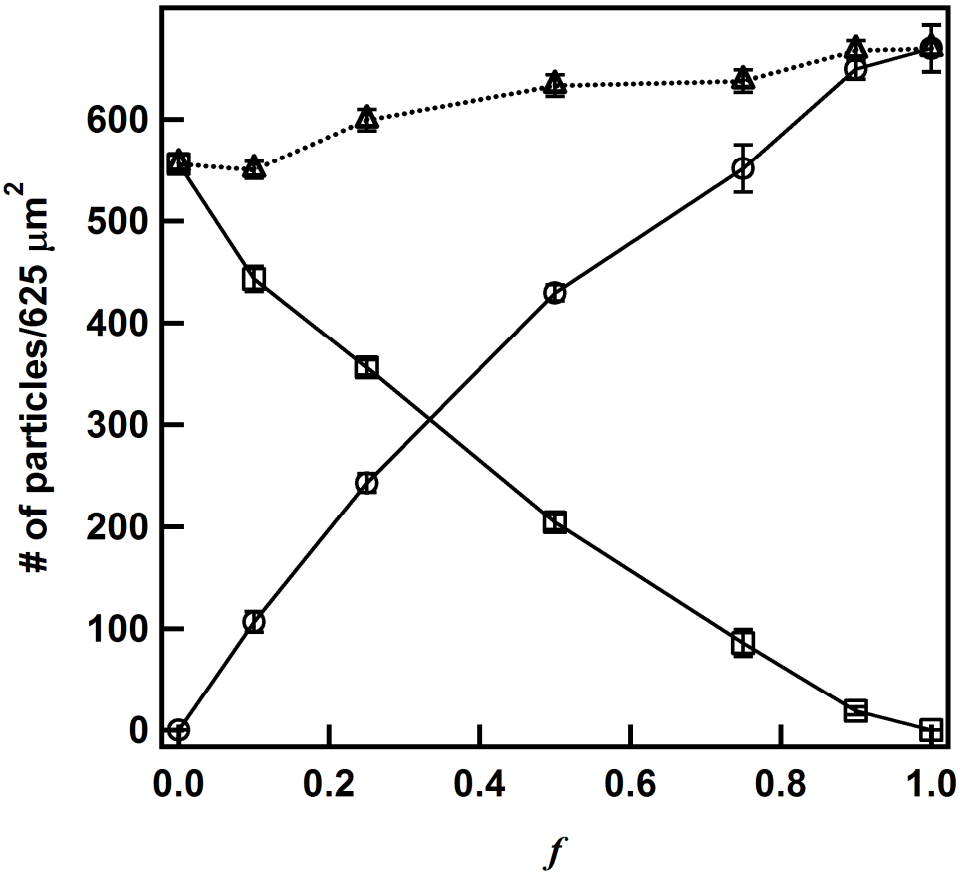

Figure 5.8. Number of each particle represented in the films. Solid curves with circles represent microgel **(1)3**, solid curves with squares represent microgel **(2)3**, dotted lines with triangles represent total values. Particle population is plotted against the adsorption solution composition, *f*. Error bars represent the standard deviation of the average values obtained from five images.

in the rates of incorporation[32] of the two cross-linkers used in the core syntheses could account for these disparities. These differences in particle internal structure evidently lead to microgels with similar solution properties, but different surface interaction properties. These differences did not, at the shell addition step, have an added effect of giving the particles different electrophoretic mobilities, which are the same for both particles over a range of pH values (Figure 5.1). The identical surface charges for the microgels suggest that these particles will have identical sticking probabilities at the pH under investigation.

The mechanical differences in surface interaction are most evident in the differences between particle footprints for the two populations, which in turn strongly influences the resultant film structure. For example, in the formation of a binary microgel film via random sequential adsorption, if the two particles had equal probabilities of reaching the surface and sticking, then at low surface coverage one should observe equal *numbers* of each particle in the film. This trend is confirmed by the images obtained when determining the jamming limit (Figure 5.2); the images of particle films prepared at 1 mM ionic strength give similar particle number coverage values. As the adsorption increases to higher *surface coverage amounts*, the available open surface for interaction will eventually become smaller than the footprint of the more deformable (larger footprint) particle. This influence will therefore bias the adsorption to the smaller footprint (denser) particles as predicted in hard disk RSA models.[1,6] This result is also demonstrated with the jamming data in Figure 5.3 (images shown in Figure 5.2). At 1 mM ionic strength, though their numbers are similar, the surface coverage is significantly higher for **(2)3**. Thus, as the **(2)3** microgels spread on the surface, smaller spaces are available for adsorption and are therefore sequentially filled by **(1)3**, which spreads less

due to its higher polymer density. These conditions lead to blocking effects that are similar to those predicted by the binary disk RSA models,[1,6] suggesting that the blocking behavior is a direct function of the differential particle footprints and has less to do with the relative diffusion coefficients of the particles. This result was also predicted by Meakin and Jullien,[6] who illustrated that the effect of blocking was largely *independent* of R (the particle size ratio) and therefore independent of the relative rates with which the particles reached the surface.

Finally, contrary to the models' predictions, the total surface coverage occupied by soft particles such as the microgels used herein is significantly higher than for a hard disk or hard sphere system. Due to the softness of particle **(2)3**, it is reasonable that these particles can deform to fit into smaller spaces than expected. There is some evidence of particle deformation (Figure 5.4), particularly in samples with high **(2)3** compositions. It is possible that if a particle is soft enough to "see" the surface, it is soft enough to squeeze into a hole if the electrostatic interaction with the surface is strong enough. This pliability, in conjunction with increased spreading due to softness, will drive the surface coverage higher than expected without increasing the particle numbers significantly. However, there is no evidence that there is any overlapping or stacking of particles, so if the deformation cannot occur, particles will not adhere to the surface with significantly smaller footprints than they occupy at low surface coverage.

5.5 Conclusions

We have shown that films formed from binary mixtures of soft particles display blocking behavior predicted by various simulations, with higher overall surface coverage

observed as a result of particle spreading. A seemingly monomodal solution of two types of particles developed itself into a clearly binary film at the interface due to differences in particle deformability and footprint size. Based on the coverage and distributions of particles in the films, as measured by AFM, it can be concluded that the particle interactions with the surface and the inherent softness of the materials play significant roles in film formation. These studies further our goals of developing generally applicable design rules for the preparation of multicomponent microgel films, where particle deformation and spreading effects strongly influence the resultant material structure and behavior.

References

1. Talbot, J.; Schaaf, P., "Random Sequential Adsorption of Mixtures." *Phys. Rev. A* **1989,** 40, 422-427.

2. Hinrichsen, E. L.; Feder, J.; Jossang, T., "Geometry of Random Sequential Adsorption." *J. Stat. Phys.* **1986,** 44, 793-827.

3. Talbot, J.; Tarjus, G.; Tassel, P. R. V.; Viot, P., "From car parking to protein adsorption: an overview of sequential adsorption processes." *Colloids Surf., A* **2000,** 165, 287-324.

4. Evans, J. W., "Random and cooperative sequential adsorption." *Rev. Mod. Phys.* **1993,** 65, 1281-1329.

5. Schaaf, P.; Talbot, J., "Surface exclusion effects in adsorption processes." *J. Chem. Phys.* **1989,** 91, 4401-4409.

6. Meakin, P.; Jullien, R., "Random-sequential adsorption of disks of different sizes." *Phys. Rev. A* **1992,** 46, 2029-2038.

7. Gray, J. J.; Klein, D. H.; Korgel, B. A.; Bonnecaze, R. T., "Microsctructure Formation and Kinetics in the Random Sequential Adsorption of Polydisperse Tethered Nanoparticles Modeled as Hard Disks." *Langmuir* **2001,** 17, 2317-2328.

8. Adamczyk, Z.; Szyk, L., "Kinetics of Irreversible Adsorption of Latex Particles under Diffusion-Controlled Transport." *Langmuir* **2000,** 16, 5730-5737.

9. Johnson, C. A.; Lenhoff, A. M., "Adsorption of Charged Latex Particles on Mica Studied by Atomic Force Microscopy." *J. Colloid Interface Sci.* **1996,** 179, 587-599.

10. Hu, Z. B.; Chen, Y. Y.; Wang, C. J.; Zheng, Y. D.; Li, Y., "Polymer gels with engineered environmentally responsive surface patterns." *Nature* **1998,** 393, 149-152.

11. Chen, L. H.; McBranch, D. W.; Wang, H. L.; Helgeson, R.; Wudl, F.; Whitten, D. G., "Highly sensitive biological and chemical sensors based on reversible fluorescence quenching in a conjugated polymer." *PNAS* **1999,** 96, 12287-12292.

12. Halls, J. J. M.; Walsh, C. A.; Greenham, N. C.; Marseglia, E. A.; Friend, R. H.; Moratti, S. C.; Holmes, A. B., "Efficient Photodiodes from Interpenetrating Polymer Networks." *Nature* **1995,** 376, 498-500.

13. Dai, L., "Polymer nanostructures." *Encyclopedia of Nanoscience and Nanotechnology* **2004,** 8, 763-790.

14. Hammond, P. T., "Form and function in multilayer assembly: New applications at the nanoscale." *Adv. Mater.* **2004,** 16, 1271-1293.

15. Decher, G., "Fuzzy Nanoassemblies: Toward Layered Polymeric Multicomposites." *Science* **1997,** 277, 1232-1237.

16. Sorrell, C. D.; Lyon, L. A., "Deformation Controlled Assembly of Binary Microgel Thin Films." *Langmuir* **2008**, In press.

17. Nolan, C. M.; Reyes, C. D.; Debord, J. D.; Garcia, A. J.; Lyon, L. A., "Phase transition behavior, protein adsorption, and cell adhesion resistance of poly(ethylene glycol) crosslinked microgel particles." *Biomacromolecules* **2005,** 6, 2032-2039.

18. Singh, N.; Bridges, A. W.; Garcia, A. J.; Lyon, L. A., "Covalent Tethering of Functional Microgel Films onto Poly(ethylene terephthalate) Surfaces." *Biomacromolecules* **2007,** 8, 3271-3275.

19. Nayak, S.; Lyon, L. A., "Ligand-functionalized core/shell microgels with permselective shells." *Angew. Chem., Int. Ed.* **2004,** 43, 6706-6709.

20. Nayak, S.; Gan, D.; Serpe, M. J.; Lyon, L. A., "Hollow thermoresponsive microgels." *Small* **2005,** 1, 416-421.

21. Gan, D.; Lyon, L. A., "Tunable Swelling Kinetics in Core-Shell Hydrogel Nanoparticles." *J. Am. Chem. Soc.* **2001,** 123, 7511-7517.

22. Jones, C. D.; Lyon, L. A., "Synthesis and Characterization of Multiresponsive Core-Shell Microgels." *Macromolecules* **2000,** 33, 8301-8306.

23. Jones, C. D.; Lyon, L. A., "Shell-Restricted Swelling and Core Compression in Poly(N-isopropylacrylamide) Core-Shell Microgels." *Macromolecules* **2003,** 36, 1988-1993.

24. Pecora, R., *Dynamic Light Scattering: Applications of Photon Correlation Spectroscopy*. Plenum Press: New York, 1985.

25. White, R. J., "FFF-MALS - A new tool for the characterisation of polymers and particles." *Polym. Int.* **1997,** 43, 373-379.

26. Blackburn, W. H.; Lyon, L. A., "Size-controlled synthesis of monodisperse core/shell nanogels." *Colloid Polym. Sci.* **2008,** 286, 563-569.

27. McGrath, J. G.; Bock, R. D.; Cathcart, J. M.; Lyon, L. A., "Self-Assembly of "Paint-On" Colloidal Crystals Using Poly(styrene-co-N-isopropylacrylamide) Spheres." *Chem. Mater.* **2007,** 19, 1584-1591.

28. Wyatt Technologies, I., *ASTRA V User's Guide Version 5.1* **2004**.

29. Serpe, M. J.; Lyon, L. A., "Optical and Acoustic Studies of pH-Dependent Swelling in Microgel Thin Films." *Chem. Mater.* **2004,** 16, 4373-4380.

30. O'Connell, P. B. H.; Brady, C. J., "Polyacrylamide gels with modified cross-linkages." *Anal. Biochem.* **1976,** 76, 63-73.

31. Aguilera-Granja, F.; Kikuchi, R., "Polymer statistics. III. Polymer adsorption on a solid surface." *Physica A* **1992,** 189, 81-107.

32. Wu, X.; Pelton, R. H.; Hamielec, A. E.; Woods, D. R.; McPhee, W., "The kinetics of poly(N-isopropylacrylamide) microgel latex formation." *Colloid Polym. Sci.* **1994,** 272, 467-477.

CHAPTER 6

DEGRADATION CONTROLLED *CO*-CROSS-LINKED MICROGEL THIN FILMS

6.1 Introduction

The use of a degradable cross-linker in acrylamide gels has long been employed for electrophoresis. The ability to degrade the gel increases its pore size and permits better control over separation.[1] The amount of degradation can be controlled in two ways. The first is to reduce the quantity of cross-linker used in the preparation of the gel and the second is to control the concentration of the degradation agent. In the case of *N,N'*-(1,2-dihydroxyethylene)bisacrylamide, degradation with periodate ion occurs with a 1:1 stoichiometry (Chapter 3, Scheme 3.5).

Novel microgel materials have already been synthesized as core/shell particles.[2] The core incorporated the degradable cross-linker while the shell contained a traditional cross-linker; degradation of the core yielded a hollow microgel. These structures are ideal candidates for drug delivery because of the large, vacant cavity in the particle's interior. To create the hollow particle, however, the shell must be relatively thin and loosely cross-linked to allow the core to be removed from the particle. Hydrogels in general have a loose enough structure to allow encapsulation of small molecules or peptides. Thus, it is desirable to have a microgel that has a degradable cross-linker used in conjunction with a non-degradable cross-linker so that the porosity of the particles can be controlled without losing the particle's cohesion.

6.2 Experimental

Reagents were purchased from Sigma-Aldrich unless otherwise specified. The monomer *N*-isopropylacrylamide (NIPAm) was recrystallized from hexanes (J.T. Baker) and dried under vacuum prior to use. The cross-linkers *N,N'*-methylenebis(acrylamide) (BIS) and *N,N'*-dihydroxyethylene-bis-acrylamide (DHEA), co-monomer acrylic acid (AAc), and initiator ammonium persulfate (APS) were used as received. The buffer components sodium dihydrogen phosphate monohydrate (Fisher Scientific), sodium chloride (Mallinckrodt), sodium hydroxide (Fisher Scientific), and sodium periodate (Acros) were used as received. The surface modification reagent 3-aminopropyltrimethoxysilane (APTMS, United Technologies, Inc.) was also used as received. Glass substrates were 24 × 24 mm VWR glass cover slips and were obtained from VWR International. Ethanol (95% and absolute) was used as received. Water used throughout this investigation was house distilled and deionized to a resistance of at least 18 MΩ (Barnstead Thermolyne E-Pure system), and then filtered through a 0.2 μm filter.

6.2.1 Microgel Synthesis

Microgel cores were synthesized via aqueous free-radical precipitation polymerization as previously described,[3-5] using 70 mM total monomer concentration. The NIPAm and AAc reactants were maintained in a 9:1 ratio; the BIS mol% was maintained at 2.5% for all particles. The DHEA concentration was modified from 0 to 7.5 mol% of the reaction mixture. The total amounts of NIPAm and AAc were reduced to accommodate the increase in cross-linker concentration. As per the reaction

Table 6.1. Amounts of each reactant used for microgel synthesis.

Particle	DHEA mol%	NIPAm (g)	AAc (μL)	BIS (g)	DHEA (g)	APS (g)
1[1]	0	0.6952	46.84	0.273	0	0.0229
2[1]	0.13	0.6943	46.78	0.0270	0.0018	0.0230
3[1]	0.25	0.6932	46.72	0.0270	0.0035	0.0232
4[1]	0.50	0.6917	46.60	0.0271	0.0071	0.0233
5[2]	0.88	0.6888	46.42	0.0271	0.0123	0.0231
6[1]	1.25	0.6862	46.24	0.0271	0.176	0.0231
7[2]	1.88	0.6818	45.94	0.0271	0.0263	0.0228
8[2]	2.5	0.6773	45.64	0.0270	0.035	0.0230
9[2]	5.0	0.6595	44.44	0.0271	0.0702	0.0229
10[2]	7.5	0.6416	43.24	0.0271	0.1052	0.0228

[1]Purified, lyophilized particles were suspended in water at a concentration of 0.0050 g/mL.
[2]Purified, lyophilized particles were suspended in water at a concentration of 0.0025 g/mL.

conditions outlined in Chapter 3, the monomers and cross-linkers were dissolved in 99 mL of deionized water. The initiator, 0.1 mmol APS, was separately dissolved in 1 mL of deionized water. The polymerization reaction was allowed to proceed for 4 hours at 65 ± 2 °C to give microgel products. Table 6.1 gives the amounts used for each synthesis.

After applying the standard purification methods (Chapter 3), the lyophilized white powders were weighed and resuspended in distilled, deionized water to a known concentration (Table 6.2).

6.2.2 Light Scattering Analysis

Dynamic light scattering (DLS) is a tool for determining mean particle size and particle size distributions[6,7] and has been used for microgel systems. The hydrodynamic radii (R_h) of the particles were determined by DLS prior to their use for thin-film fabrication. Briefly, a dilute microgel solution in buffer was added to a 384-well titer plate and inserted into the DynaPro Plate Reader (Wyatt Technologies, Inc., Santa Barbara, CA). Each microgel sample was evaluated at 23 °C in pH 3.0 formate buffer (10 mM, 10 mM ionic strength) and pH 6.5 phosphate buffer (10 mM, 25 mM ionic strength) by taking five measurements consisting of ten acquisitions each.

The z-averaged radii (R_z) and molar masses (M_z) of the particles were determined by multi-angle laser light scattering (MALLS, DAWN EOS, Wyatt Technologies, Inc.) and differential refractive index measurements (dRI, OptiLab rEX, Wyatt Technologies, Inc.) prior to their being use in thin film fabrication. The MALLS detector is equipped with a Peltier device to maintain a flow cell temperature of 25 °C, and it collects scattered light from 18 different fixed angles to determine the R_z. ASTRA 5.3.1.15 software was applied to determine R_z and M_z by using the Debye fit method.[8] The particle size and molar mass were determined using a known concentration of particles in pH 6.5 10 mM PBS buffer (25 mM ionic strength). The *dn/dc* for each type of particle was determined using dRI measurements; the specifics of the experiments and the results are presented in Chapter 3.

6.2.3 Film Preparation

Glass coverslips (24 mm x 24 mm) were cleaned by using an Ar plasma (Harrick Plasma, Ithaca, NY) for ~15 minutes. Each cleaned slide was functionalized by exposure

Table 6.2. Particle properties for all microgels determined by light scattering at pH 6.5.

Particle	R_h at pH 3.0 (% polydispersity)	R_h at pH 6.5 (% polydispersity)	R_z (% polydispersity)	Molar Mass (g/mol)
1	329 nm (14%)	512 nm (3.8%)	210 nm (3%)	3.2e+8
2	326 nm (4.2%)	503 nm (49%)	167 nm (3%)	4.2e+8
3	347 nm (9.1%)	555 nm (30%)	176 nm (2%)	3.7e+8
4	374 nm (6.5%)	538 nm (21%)	177 nm (2%)	3.3e+8
5	295 nm (3.0%)	279 nm (82%)	234 nm (5%)	3.4e+8
6	384 nm (16%)	506 nm (15%)	162 nm (5%)	3.1e+8
7	326 nm (3.2%)	529 nm (29%)	169 nm (3%)	2.5e+8
8	321 nm (14%)	500 nm (31%)	184 nm (16%)	2.7e+8
9	348 nm (5.7%)	432 nm (69%)	173 nm (4%)	4.4e+8
10	369 nm (7.4%)	231 nm (41%)	176 nm (4%)	5.5e+8

to a 1% solution of 3-aminopropyltrimethoxysilane (APTMS) in absolute ethanol for ~2 h.[9] The functionalized slides were rinsed with ethanol (95%), and stored for up to 1 week in absolute ethanol. Before use, each slide was rinsed with ethanol and dried under a stream of N_2.

The films were fabricated from a 2.5 x 10^{-4} g/mL dilution of each particle type in pH 6.5 PBS buffer (20 mM, 100 mM ionic strength). Each film was fabricated via passive adsorption by placing a sessile drop of the particle solution on a clean, dry, functionalized glass coverslip. The films were allowed to form over 2 hours.

6.2.4 Atomic Force Microscopy Measurements

AFM data were taken in air in the AC mode on an Asylum Research MFP-3D instrument (Santa Barbara, CA). Imaging and analysis were performed using the Asylum

Research MFP-3D software running in the IgorPro environment (WaveMetrics, Inc., Lake Oswego, OR).

Nanoworld FM-10 Pointprobe cantilevers were used (k = 2.8 N/m, f_0 = 75 kHz) to image the films in air. An AR-iDrive cantilever (a modified 100 μm triangular shape Olympus BL-TR400PB cantilever with f_0 = 35 kHz in air and k_0 = 0.09 N/nm) was used for in-liquid imaging with the iDrive. To prepare AFM samples, the film-coated substrates (dried as described above) were attached by adhesion to a standard microscope slide using Leitsilber 200 Silver Paint (Ted Pella, Inc., Redding, CA).

Images were taken at scan ranges of 10 μm x 10 μm, and 25 μm x 25 μm. Images had a resolution of 512 scan lines consisting of 512 points each. All films were imaged in air shortly after fabrication. After imaging in air, the samples were placed in a sessile drop of pH 6.5 PBS buffer (20 mM, 100 mM ionic strength), and the film was imaged in liquid using the iDrive™. A sessile drop of a 1 mM solution of $NaIO_4$ in pH 6.5 PBS buffer was placed on the sample, and the film was allowed to degrade for several hours. The drop was rinsed off the sample with water, and a new sessile drop of pH 6.5 PBS was placed on the sample. The sample was re-imaged in liquid using the iDrive™. After imaging, the sample was rinsed with water and allowed to dry. The sample was re-imaged in air. Some of these images were taken at a scan range of 2 μm x 2 μm. Height analysis of the films before and after degradation was performed by using the image analysis tools built into the software provided with the instrument, specifically, histogram analysis of the height profile of the entire image for the dry samples and single line analysis for in-liquid images.

Table 6.3. Changes in particle height due to degradation determined by AFM.

Particle	Undegraded height (nm)[1]	Degraded height (nm)[1]	ΔHeight (nm)
1	11.2 (±2.8)	10.5 (±3.1)	-0.7
3	16.2 (±3.8)	16.5 (±6.5)	+0.3
4	12.7 (±4.1)	13.7 (±5.5)	+1.0
6	15.1 (±3.2)	11.8 (±3.6)	-3.3
8	10.5 (±2.8)	9.2 (±3.9)	-1.3
9	7.8 (±2.0)	4.5 (±2.2)	-3.3

[1]Error measurements are the full width at half max for the Gaussian curve fit to the height data histogram.

6.3 Results

Ten types of co-cross-linked microgel particles were prepared and analyzed. The sizes and molecular weights of the particles determined by dynamic light scattering and static light scattering are presented in Table 6.2. The particles are all similar in size in solution as are their molar masses. They seem to increase slightly in molar mass as the amount of DHEA used in the synthesis increases above parity with the BIS cross-linker (microgel **8**), but this increase may be due to inaccuracies in the *dn/dc* measurement (Chapter 3).

Detailed AFM results will focus on products **1**, **3**, **4**, **6**, **8**, and **9**. In general, the AFM images show that most of the particles (microgels **1**-**8**) formed a uniform monolayer

within the experimental parameters. Microgel **9** formed a very sparse film (Figure 6.1) and microgel **10** (not shown) appeared to form aggregates on the substrate.

After degradation, the particles in the films do seem changed in morphology with increasing DHEA concentration, but how this affects the particle is not really clear unless the height profile analysis of the images is considered (Table 6.3). The heights of the particles do not change significantly until the concentration of DHEA is ~1.25% of the particle (microgel **6**). However, some samples show evidence that part of the polymer is

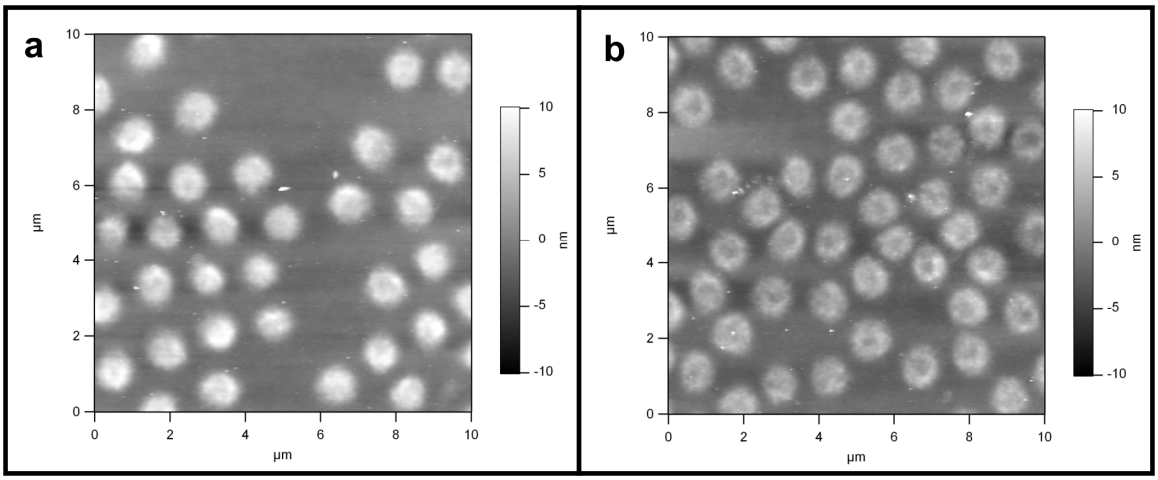

Figure 6.1. AFM images depicting a film formed from microgel **9** in air, a) before degradation, and b) after degradation.

breaking free from the structure of the microgel and interacting with the surface (Figure 6.2).

Intriguingly, the particle swelling do not increase as much as expected to swell significantly in liquid after the films were degraded (Figure 6.3). The only clear changes in morphology were seen after the sample was dried again. The AFM data showed that the particle structures were relatively homogeneous before degradation; but after the heterogeneity of the particles increases. This is clear from the increased "lumpiness" of the particles after degradation (Figure 6.2). Most of the particles exhibit this morphology after they have been degraded, but the degree of the morphology change appears to increase with an increasing concentration of DHEA. This effect is especially clear to see in Figure 6.4 of microgel **8**. The phase analysis image shows an apparent phase separation in the particle.

6.4 Discussion

The most striking result was that the particles did not lose cohesion once they were degraded, even at high concentrations of the degradable cross-linker. It was expected that the particles would break open and create a space-filling film at some concentration of DHEA. The particles with the highest DHEA concentrations do show erosion (Figure 6.1), but they still maintain their original particle conformations in fluid.

Additionally, the degraded particles do not appear to swell significantly more than their undegraded counterparts. One possibility is that particle erosion is occurring at the

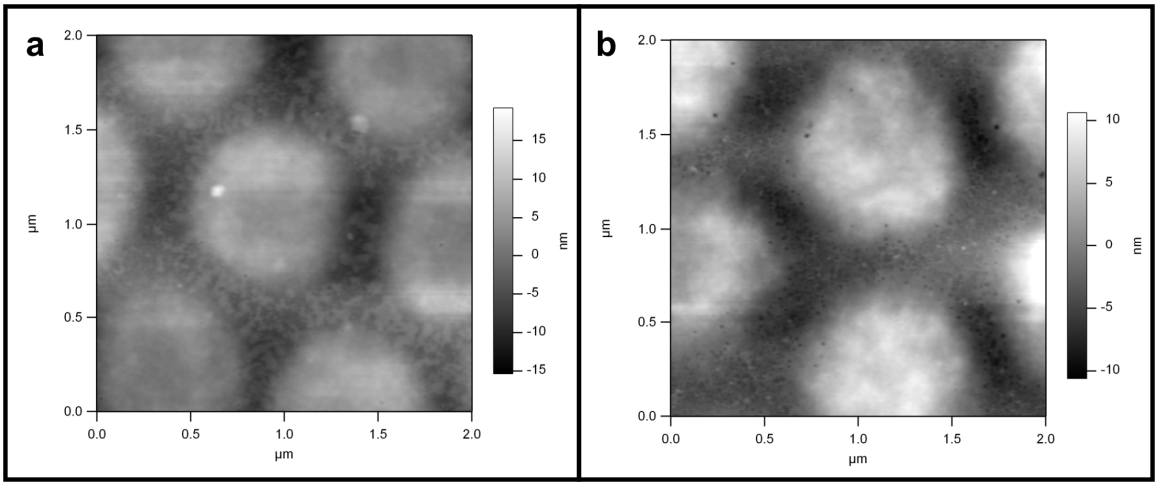

Figure 6.2. AFM height images showing a) microgel **6** and b) microgel **7** after degradation.

same rate as particle swelling, so no change in size is detectable (Figure 6.3). However, the height analysis before and after degradation (Table 6.3) does not indicate that much of the particle mass is being lost to the environment. The presence of a non-degradable cross-linker, even at concentrations much lower than the degradable cross-linker, evidently provides enough local connectivity throughout the particle to maintain its shape and size when it is swollen and degraded. Some of the polymer is being displaced from the particles onto the surface (Figure 6.2), but even from these images it is clear that the displacement is small.

The original purpose for using the DHEA cross-linker was based on the idea that DHEA would provide chemical handles for chemoligation. The cross-linker degrades into two formamide moieties via reaction with periodate ion (Chapter 3, Scheme 3.5). A

cursory glance at the formamide shows a –CHO group attached to the nitrogen atom, so the assumption was made that this formyl group would be available (similar to a normal aldehyde) for reactions with amines via reductive amination. As a result, some studies using purpald[10] and Schiff's[11,12] reagents were performed to attempt quantification of the DHEA incorporation by determining the concentration of the –CHO groups remaining in the particles after degradation. It was only after the failure to produce a response from both that the structure of the degraded cross-linker was reevaluated. The formimide group has a resonance structure in which a double bond exists between the carbonyl carbon atoms and the nitrogen atom of the imide group. The AFM images show that as the DHEA concentration increases, the particles appear to decrease in polymer density (compare Figure 6.3 of microgel **4** to Figure 6.1 of microgel **9**). A marked change in almost all aspects of the data (molar mass, AFM height profiles, apparent degradation by AFM, and *dn/dc* values) occurs when the two cross- linkers have the same concentrations in the synthesis (microgel **8**). Studies performed with capillary zone electrophoresis have shown that the degree of incorporation of the cross-linker and the monomer decreases with increasing concentration of the cross-linker.[13,14] So, when cast in this light the apparent decrease in polymer density is not surprising. However, the decrease does run contrary to the molar mass data, which show a slight increase in mass as the concentration of the cross-linker increases. Inaccuracies in the *dn/dc* values measured via dRI analysis (Chapter 3) are probably the largest factor contributing to this discrepancy.

Studies that described the effect of cross-linker concentrations on monomer incorporation also mention that as the cross-link concentration increases there is a marked

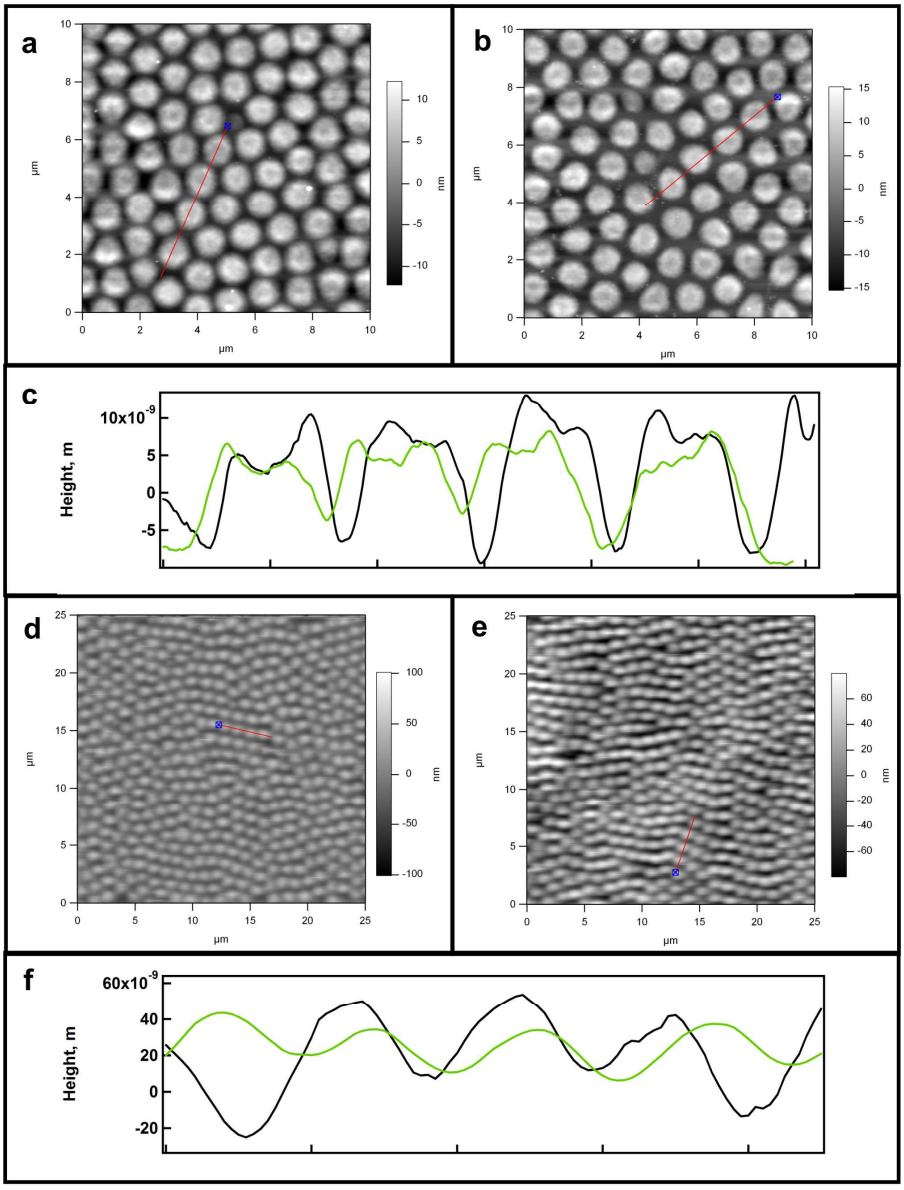

Figure 6.3. Complete analysis of films composed of microgel **4**. Each panel shows a) a non-degraded film imaged in air, b) a degraded film imaged in air, c) the associated section line profiles for panels a and b, d) a non-degraded film in pH 6.5 buffer, e) a degraded film in pH 6.5 buffer, and f) the associated section line profiles for panels d and e. For the profiles, the green trace represents a non-degraded film and the black trace represents a degraded film.

increase in "knottiness" because the cross-link density makes the polymer chains shorter and thicker.[13] For the microgels described here, "knottiness" appears to increase with increasing DHEA concentration and becomes more apparent after degradation (Figures 6.2 and 6.4a).

All of the particles synthesized for these studies show a "divot" near the center of the particle (Figure 6.3). Before degradation, the particles are all flattened in the center. Post-degradation, particularly at high DHEA concentration, this divot becomes more pronounced (Figure 6.1 and 6.3). An AFM image was taken at a scan angle of 90° to make sure the indentation was not a tip artifact. If it were an artifact, changing the scan angle would translate the artifact orthogonally to the original image; if the feature is part of the sample, the image will remain the same. Additionally, several cantilevers were

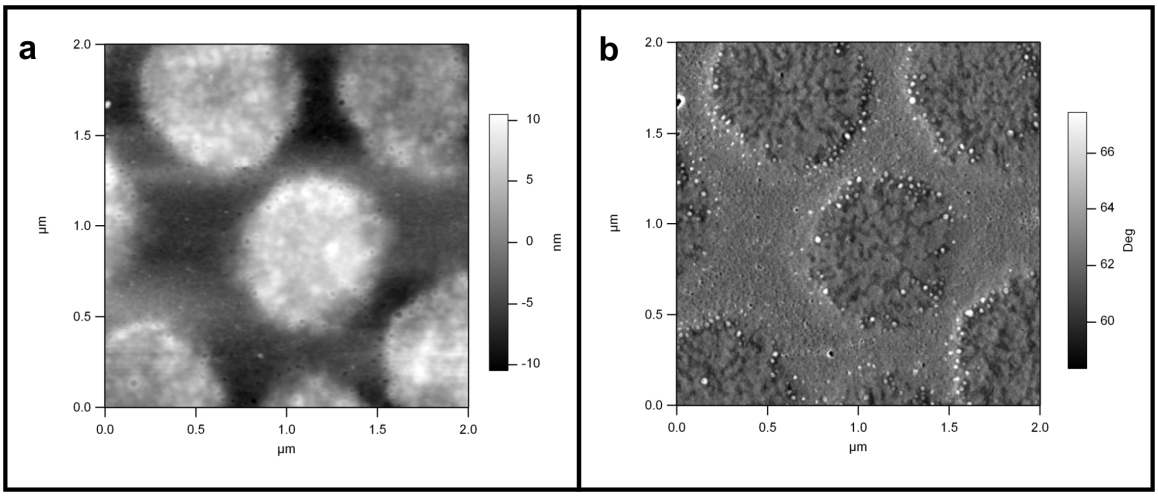

Figure 6.4. AFM a) height and b) phase angle images depicting a film formed from microgel **8** in air after degradation.

used over the course of imaging. The divot appeared to be universal to all tips.

Previous studies have shown that the more hydrophobic the cross-linker, the less it incorporates with increasing concentration.[13,14] What those studies also showed is an inverse correlation between the hydrophobicity of the cross-linker molecule and its incorporation into a polymer network.[14] DHEA and BIS have similar hydrophobicities, but BIS is slightly more hydrophobic with a partition coefficient (into hexanes) of ~0.82.[13] DHEA has a partition coefficient of ~0.27.[13] Depending on the length of the degraded chains, if a core of highly DHEA cross-linked pNIPAm were concentrated in the center of the particle, it is likely after degradation that the polymer would partition out of the particle leaving an essentially hollow core. The uneven incorporation of monomers is most clearly seen in Figure 6.4, which shows a phase separation occurring within the particles. Whether this phase separation resulted from the degradation or the synthesis of the particle is unclear. The phase separation is not apparent before degradation, so that observation might indicate that the change is a result of degradation. However, the AFM height data indicate that those particles do erode upon degradation, so the degradation process may have removed just enough of the outer "shell" of the polymer so as to elucidate the nature of the core.

6.5 Conclusions

The original purpose for making co-cross-linked particles was to increase the number of chemical handles on a microgel to facilitate conjugation of biomolecules onto the particle structure. In solution, such particles could be used for drug delivery; in a thin film bioconjugated particles could be used in sensors. Even though these structures did

not yield any products for use in the conjugation of other molecules, some interesting observations were made about how a co-cross-linked system changes particle morphology. To determine the exact nature of the particle structure, additional studies would need to be performed, but these studies provide a fundamental first step towards a better understanding of microgels and microgel films.

References

1. Aizawa, K., "Elastomeric polyacrylamide gels for high-resolution electrophoresis of proteins." *Polym. Adv. Technol.* **2000,** 11, 481-487.

2. Nayak, S.; Gan, D.; Serpe, M. J.; Lyon, L. A., "Hollow thermoresponsive microgels." *Small* **2005,** 1, 416-421.

3. Gan, D.; Lyon, L. A., "Tunable Swelling Kinetics in Core-Shell Hydrogel Nanoparticles." *J. Am. Chem. Soc.* **2001,** 123, 7511-7517.

4. Jones, C. D.; Lyon, L. A., "Synthesis and Characterization of Multiresponsive Core-Shell Microgels." *Macromolecules* **2000,** 33, 8301-8306.

5. Jones, C. D.; Lyon, L. A., "Shell-Restricted Swelling and Core Compression in Poly(N-isopropylacrylamide) Core-Shell Microgels." *Macromolecules* **2003,** 36, 1988-1993.

6. Pecora, R., *Dynamic Light Scattering: Applications of Photon Correlation Spectroscopy*. Plenum Press: New York, 1985.

7. White, R. J., "FFF-MALS - A new tool for the characterisation of polymers and particles." *Polym. Int.* **1997,** 43, 373-379.

8. Wyatt Technologies, I., *ASTRA V User's Guide Version 5.1* **2004**.

9. Serpe, M. J.; Lyon, L. A., "Optical and Acoustic Studies of pH-Dependent Swelling in Microgel Thin Films." *Chem. Mater.* **2004,** 16, 4373-4380.

10. Hopps, H. B., "Purpald: A Reagent that Turns Aldehydes Purple!" *Aldrichimica Acta* **2000,** 33q, 28-30.

11. Kasten, F. H., The Chemistry of Schiff's Reagent. In *International Review of Cytology*, Bourne, G. H.; Danielli, J. F., Eds. Academic Press: New York and London, 1960; Vol. 10, pp 1-100.

12. Robins, J. H.; Abrams, G. D.; Pincock, J. A., "The structure of Schiff reagent aldehyde dducts and the mechanism of the Schiff reaction as determined by nuclear magnetic resonance spectroscopy." *Can. J. Chem.* **1980,** 58, 339-347.

13. Gelfi, C.; Alloni, A.; Debesi, P.; Righetti, P. G., "Investigation of the Properties of Acrylamide Bifunctional Monomers (Cross-linkers) by Capillary Zone Electrophoresis." *J. Chromatogr.* **1992,** 608, 343-348.

14. Gelfi, C.; Debesi, P.; Alloni, A.; Righetti, P. G., "Investigation of the Properties of Novel Acrylamido Monomers by Capillary Zone Electrophoresis " *J. Chromatogr.* **1992,** 608, 333-341.

CHAPTER 7

FUTURE DIRECTIONS

The projects discussed in the previous chapters were fundamental studies of microgel thin films at interfaces. When these projects were started, the premise was that we would be able to induce a significant change in a material by means of a simple binding experiment. As previously mentioned, the inspiration for this notion was research performed by Lasky and Buttry in 1989 (*ACS Symp. Ser.*) whereby an unexpected and significant change was detected by use of a quartz crystal microbalance when glucose was bound by hexokinase within a polyacrylamide gel. With these facts in mind, the studies presented herein provide a firm foundation for future research aimed at developing microgel thin films into sensitive, soft actuators.

- In Chapter 4, a bimodal swelling behavior for thin films was described. The data showed that the response was dictated at some level by the molecular weight of the polycation used in the thin film's construction. Further studies may find that this sensitivity can be tuned such that the film's response correlates with the molecular weight of an unknown polycation. This goal might be accomplished through a series of studies using many polycations of different molecular weights.
- Some preliminary results using the microgels described in Chapter 4 in a solution phase (not presented) suggest that the bimodal film would be sensitive to multivalent metal ion binding. When the particles used to make the films were placed in a buffer solution doped with metal ions with differing charges (Cu^{2+} or Y^{3+}), the hydrodynamic radius of the microgel decreases with increasing charge of the ion. Although a response from these films as a result of metal ion binding

would not indicate the presence of a *specific* ion, it might provide an indication about the charge of the dissolved species. This sensor could be made reversible by washing with an EDTA buffer at the appropriate pH for binding of the metal ion by the chelating agent.

- An extensive study of binary films was presented in Chapter 5. Understanding how mixtures form films is an important step for any biomaterial, particularly those used for drug delivery. The ability to control the amount of a drug released by a delivery device is of increasing interest. Further research could allow one to limit the amount of drug in the device by using a restricted number of particles or drug carriers or by changing how many reach the surface. If only a certain number of drug carriers are available the dosage can be reduced more easily.
- The ability to control the morphology of a gel is important for myriad applications. The *co*-cross-linked microgels presented in Chapter 6 give some insight into how degradable cross-linker concentration can change the morphology of a microgel particle without loss of particle coherence. A layer-by-layer film constructed from such particles would be ideal for developing permeable membranes and coatings, as well as for creating soft actuators by selectively reducing the cross-link density to enhance responsivity. Degradable cross-linkers also provide useful handles for chemoligation of enzymes or other biomolecules to make nanoreactors. A degradable cross-linker can also open a particle's structure, which can allow encapsulation of larger biomolecules for delivery. If the chemoligation reaction with the degraded cross-linker is biocompatible, a large biomolecule could be encapsulated and caged into the particle via selective re-cross-linking.

APPENDIX A

CHARACTERIZATION OF PHYSICALLY CROSS-LINKED "PAINT-ON" COLLOIDAL CRYSTALS

A.1 Introduction

The facile assembly of optical materials using soft materials has been developed in several different ways. The most well-known soft optical material is described in the work completed by Sanford Asher and co-workers.[1-6] They exploited the physical properties inherent in colloidal dispersions of polymeric materials to create interesting optical materials. Their theories evolved from the idea that one could create colloidal assemblies from monodispersed, highly-charged colloidal particles via a self-assembly mechanism that was due largely to electrostatic repulsions in low-ionic strength media.[3]

With that basic principle in mind, Asher began to make responsive soft optical materials by creating colloidal arrays embedded in a soft *N*-isopropylacrylamide hydrogel matrix.[2] In that system, hard-sphere polystyrene colloids were arranged as a crystalline matrix and their periodicities were locked into a hydrogel network via a light-induced polymerization mechanism. The periodicity of the array can be changed by altering the conformation of the network surrounding the crystal. By mechanically stretching the hydrogel matrix, the layer spacing normal to the film's surface is reduced thus changing the diffraction wavelength of the crystal. They further demonstrate that one could expand this idea to make limiters with a refractive index matched system[1] by using poly(methyl methacrylate) spheres and replacing the fluid in the hydrogel around the spheres with

benzyl alcohol. Perturbation of the system to change the refractive index between the spheres and the surrounding medium causes the system to diffract light and the device becomes a limiter.

Asher and co-workers expanded this work to look at how the thermoresponsivity of the N-isopropylacrylamide affected the system.[3] Initially, they showed that a colloidal crystal formed from microgels has a higher Bragg diffraction efficiency at high temperatures (above the LCST, i.e. deswollen) than the same crystal at low temperatures (below the LCST, i.e., swollen). The lattice spacing of the crystal did not change in this conformation; but because the particles at high temperature were deswollen, the light was diffracted by the particles very efficiently. These materials were touted as easily controlled optical switches as well as optical limiters. As an expansion of their previous work,[2] Asher and co-workers then took a colloidal assembly of polystyrene stabilized by a hydrogel polymer network and fabricated a wavelength-tunable diffraction material.[3] A change in the swelling of the matrix due to an increase in temperature caused the diffraction wavelength to decrease while the extinction coefficient increased. Thus, these materials act as easily controlled optical filters that are affected by changing the temperature or incident angle of light At a fixed angle the same materials acts as tunable reflectors.

After the initial studies of these materials, several forays into sensor technology were undertaken.[4,6] Using a crystal of polystyrene particles stabilized by a hydrogel network,[1,2] researchers were able to demonstrate the use of these materials as a sensor.[4] First, a molecular-recognition entity was embedded in the hydrogel network; a change in the swelling of the gel due to the change in osmotic pressure created by the ingress of an

analyte was measured by a change in the diffraction wavelength of the crystal. It was demonstrated that different kinds of analytes could be detected quantitatively; these included complexation of multivalent ions by a crown ether and glucose oxidation to gluconic acid by glucose oxidase. Further studies led to the design of experiments that probed the effect of changing the pH and ionic strength.[6] It was shown that changes in the wavelength diffraction could be made in the hydrogel matrix by changing the pH and ionic strength of the solution in a partially hydrolyzed acrylamide gel embedded with a polystyrene colloidal crystal. As the ionization of the carboxyl groups changes as a result of what is occuring in the surrounding solution, the gel swells or deswells accordingly. Concomitantly, with changes in the ionization and osmotic pressure associated with those changes, the wavelength diffracted by the crystal lattice embedded in the film is affected.

Hu and coworkers created responsive optical materials by depositing surface patterns onto an *N*-isopropylacrylamide gel.[7] Below the LCST, a periodic pattern of gold squares on the surface of the gel diffracted light with a specific pattern. When the gel temperature was raised above the LCST, the NIPAm gel deswelled and the periodicity of the diffraction pattern was reduced. Similarly, a NIPAm gel with a hexagonal pattern printed on its surface showed lessened periodicity in the diffraction pattern in the dried state than it did in the swollen state. These materials were shown to be similar to the materials developed by Asher and co-workers. Hu and co-workers also looked at materials in which a pNIPAm pattern was deposited onto a pAAm gel. In this system both gels are colorless at room temperature. However, when the temperature was raised above the LCST of pNIPAm, the pNIPAm pattern on the pAAm gel became more turbid due to deswelling of the NIPAm polymer. It was postulated that with further study, this

phenomenon could be used to create sensors by using various stimuli to induce this difference in turbidity of the gels.

To continue their work with optical materials as well as to build on the work done by Asher and co-workers, Hu and co-workers set out to make soft, colloidal materials using soft sphere colloids made primarily of N-isopropylacrylamide in a fixed network.[8] Their work was inspired by opals and entailed using carboxyl- and hydroxyl-terminated pNIPAm microgels. The microgels maintained their thermoresponsive behaviors, and the hydroxyl and carboxyl functional groups provided handles for cross-linking with other particles. Once they were cross-linked, the particles were locked in a 3-D array that was responsive, not to the matrix surrounding the particles, but to the particles themselves. Changing the wt% of the particles altered the lattice spacing of the crystal and generated crystals with different diffractive wavelengths. Hu was able to further demonstrate that the arrays maintained their shape once cross-linked, that they were still thermoresponsive with the wavelength changing concomitantly, and that the materials were useful as sensor materials.

Inspired by the efforts of Asher and Hu, Lyon and co-workers developed an easily processed colloidal material that was stable and wavelength tunable without the aid of a polymer network or supporting solution.[9] They used a semi-soft colloid synthesized from *N*-isopropylacrylamide and styrene that allowed for fast and easy fabrication of materials via a "paint-on" mechanism. The particles in this study are largely composed of styrene (~75%) and are not thermoresponsive, but the pNIPAm co-polymer adds a softness at the surface of the particles that aids in crystal assembly. Changes in the synthesis of the colloids changed the particle size; in these crystals, the Bragg diffraction of the crystal is

dependent on the dried particle spacing, which is initially dependent on the particle size in solution. As the crystal dries on the surface, the wavelength diffracted by the crystal is shifted to the blue as the particles dry and packs into their final conformation.

The body of work completed by Dr. Jonathan McGrath in Prof. Andrew Lyon's group included a study of physically cross-linked poly(styrene-co-*N*-isopropylacrylamide) photonic crystals. The same system described above[9] was used to make stable colloidal crystals that would undergo a wavelength shift when wetted. The work presented in this appendix is a detailed characterization of these materials using atomic force microscopy techniques.

A.2 Experimental

A.2.1 Microgel synthesis

All materials were synthesized and fabricated as described previously by Dr. Jonathan McGrath.[10] Briefly, the particles (280-2, 300-1, and 500-2) were prepared by placing a sessile drop of the microgel solution onto a microscope cover slip and allowing the drop to dry. At least 3 samples were made for each particle type. A sample of each particle type was placed in a 110°C oven for 0, 3, or 6 days. The samples' diffraction wavelength was determined using reflectance UV/visible spectroscopy (Ocean Optics, Inc.) in air, before and after baking, and in water, after baking.

A.2.2 Atomic Force Microscopy Measurements

AFM data were taken in air in AC mode on an Asylum Research MFP-3D instrument (Santa Barbara, CA). Imaging and analysis were performed using the Asylum Research

MFP-3D software running in the IgorPro environment (WaveMetrics, Inc., Lake Oswego, OR).

Nanoworld SEIHR-10 Pointprobe cantilevers were used (k = 15 N/m, f_0 = 130 kHz) to image the films in air. To prepare AFM samples, the crystal-laden substrates (dried and baked as described above) were attached by adhesion to a standard microscope slide using Leitsilber 200 Silver Paint (Ted Pella, Inc., Redding, CA). Standard amplitude modulation imaging in liquid was also performed on the crystal samples that were baked for 6 days. A sessile drop was placed on the sample, and the imaging was performed with an Olympus TR400PB cantilever (100 μm, k = 0.09 N/m, f_0 = 32 kHz) or an Olympus TR800PSA cantilever (100 μm, k = 0.15 N/m, f_0 = 24 kHz).

Center-to-center distances were measured and image processing was performed using the MFP-3D software provided with the AFM. For size analysis, a line was drawn in plane with a lattice row of the crystal. The distance from the top of one particle to another was taken as an average over at least 10 particles.

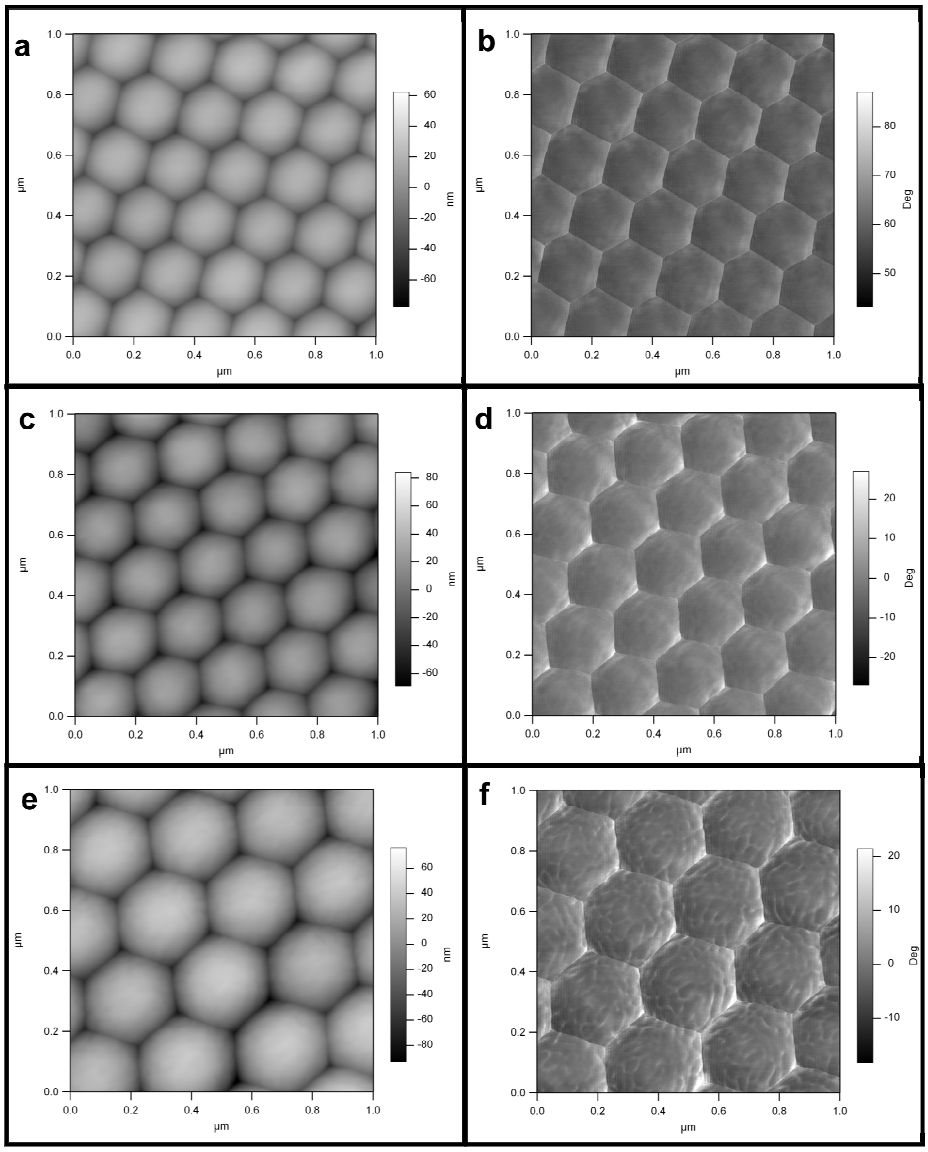

Figure A.1. AFM images for samples that were dried and not annealed at 110 °C. Panels show height and phase, respectively, for colloidal crystals made from 280-2 (a, b), 300-1 (c, d), and 500-2 (e, f).

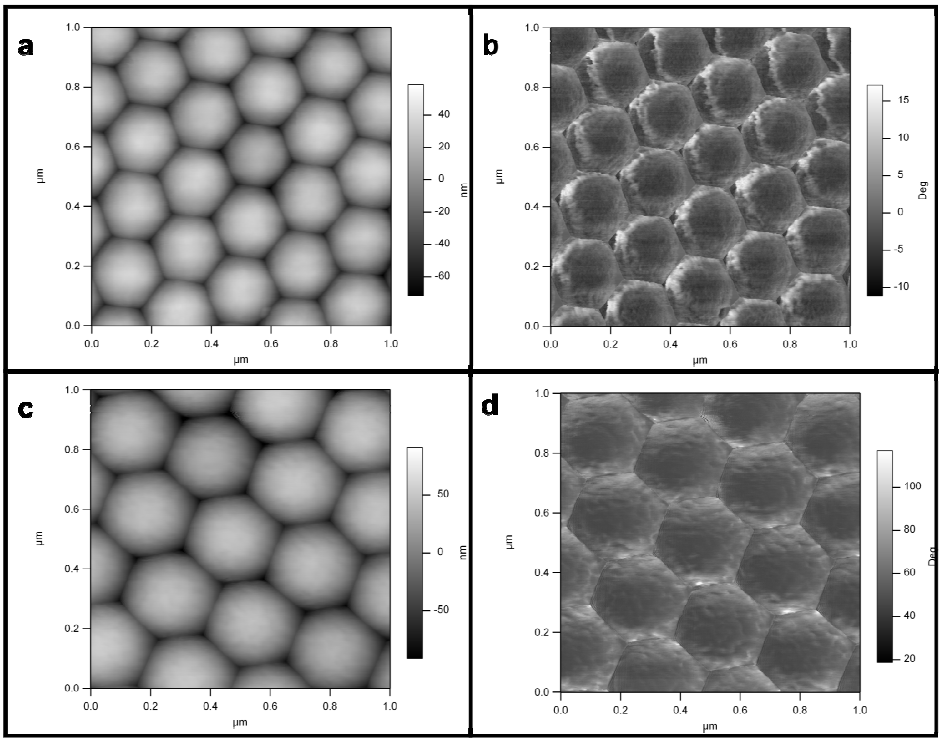

Figure A.2. AFM images for samples that were dried and annealed at 110 °C for 3 days. These samples were wetted and re-dried prior to analysis by AFM. Panels show height and phase, respectively, for colloidal crystals made from 300-1 (a, b), and 500-2 (c, d). The 280-2 sample dissolved upon rewetting so it was not available for imaging.

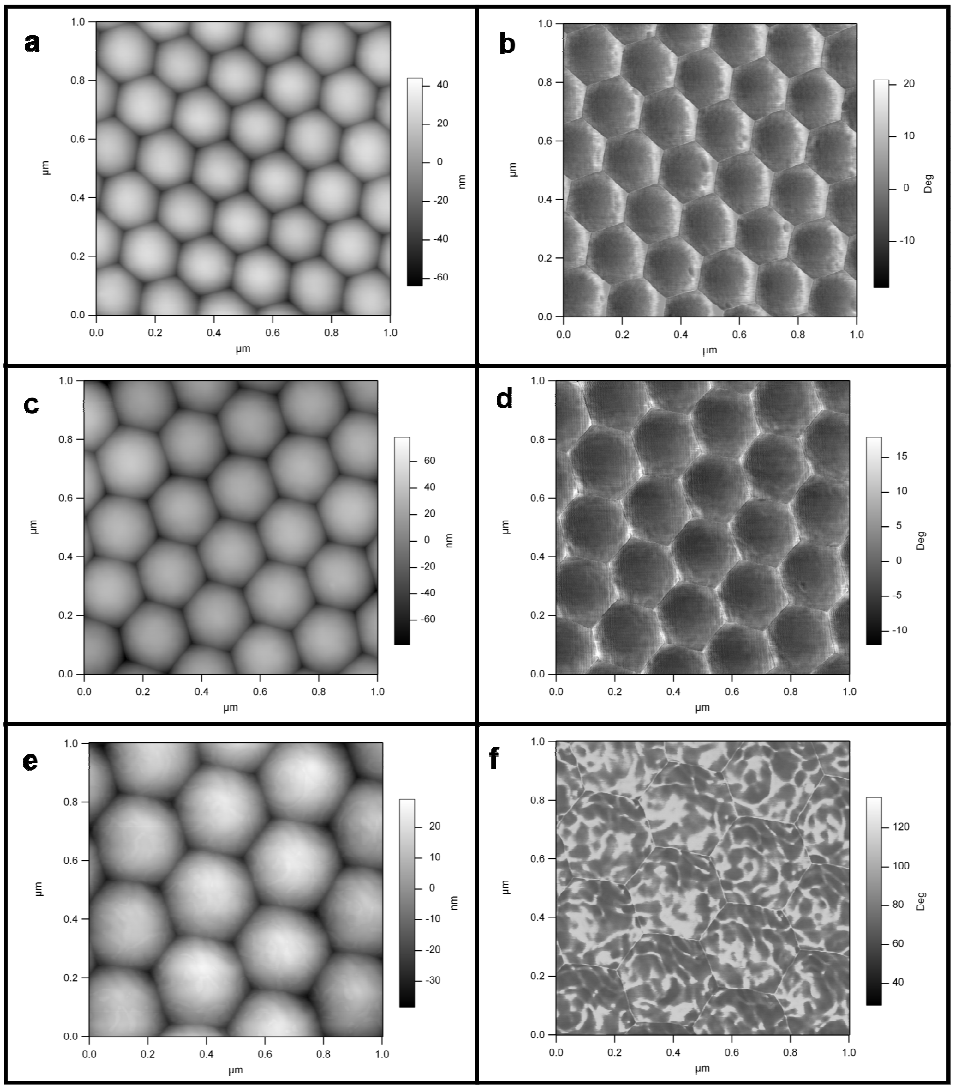

Figure A.3. AFM images for samples that were dried and annealed at 110 °C for 6 days. These samples were wetted and re-dried prior to analysis by AFM. Panels show height and phase, respectively, for colloidal crystals made from 280-2 (a, b), 300-1 (c, d), and 500-2 (e, f).

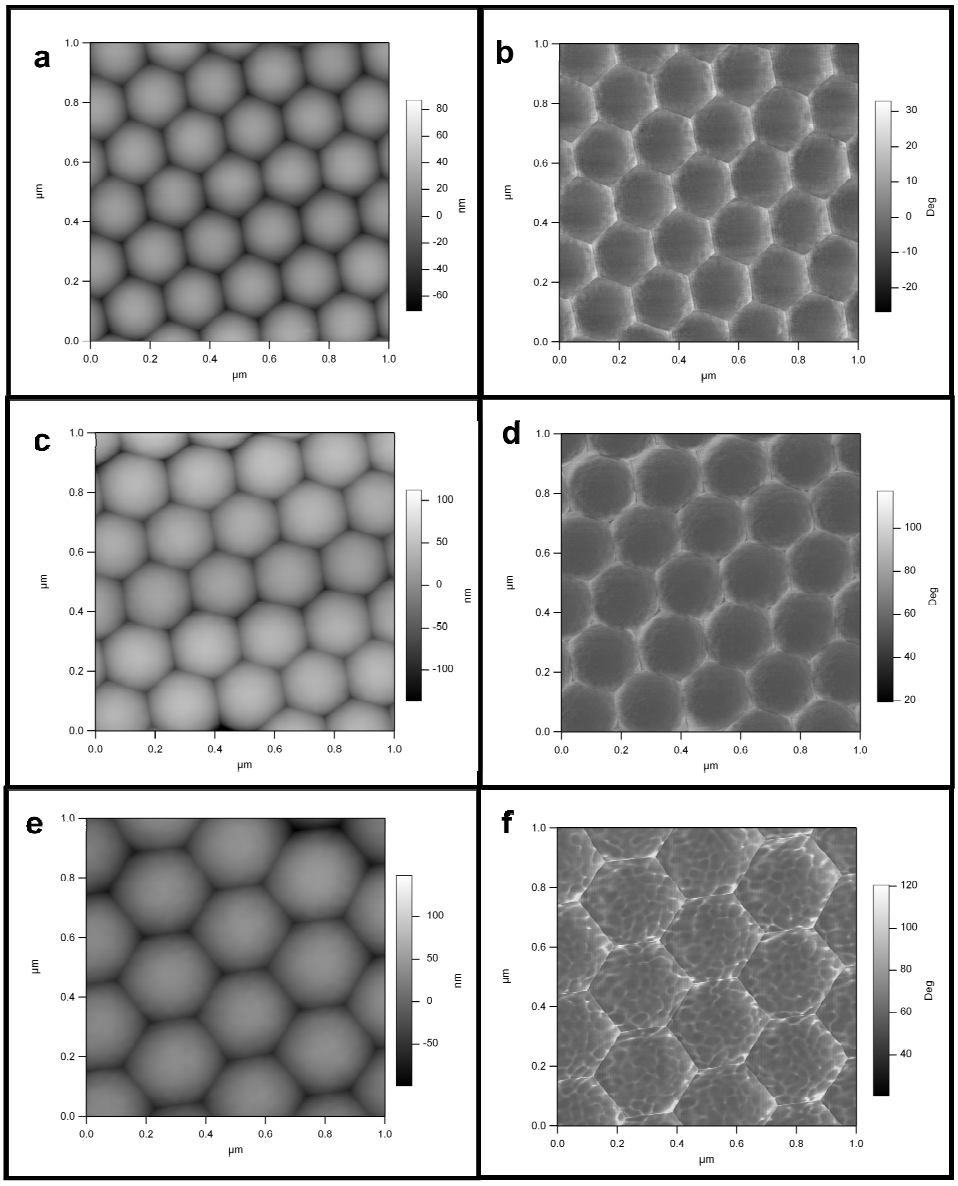

Figure A.4. AFM images for samples that were dried and annealed at 110 °C for 3 days. These samples were not wetted prior to analysis by AFM. Panels show height and phase, respectively, for colloidal crystals made from 280-2 (a, b), 300-1 (c, d), and 500-2 (e, f).

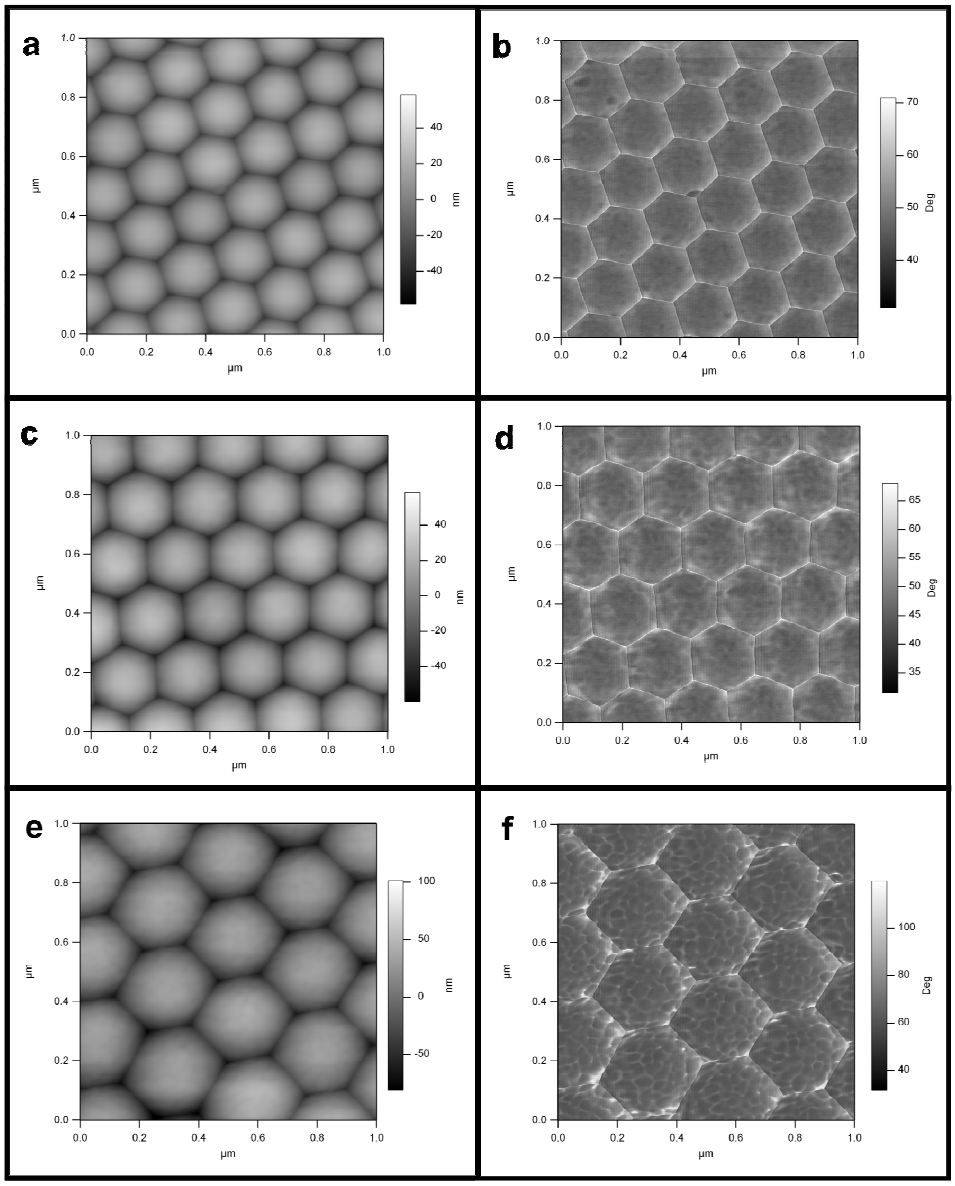

Figure A.4. AFM images for samples that were dried and annealed at 110 °C for 6 days. These samples were not wetted prior to analysis by AFM. Panels show height and phase, respectively, for colloidal crystals made from 280-2 (a, b), 300-1 (c, d), and 500-2 (e, f).

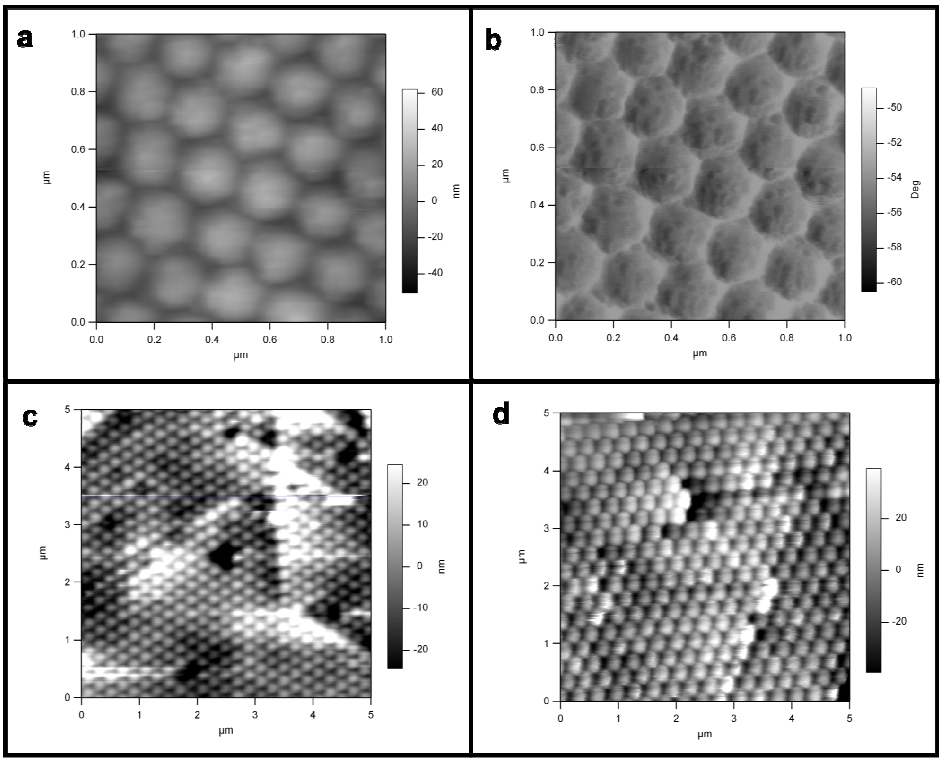

Figure A.4. AFM images in-liquid for samples that were dried and annealed at 110 °C for 6 days. These samples were wetted and re-dried prior to in-liquid analysis by AFM. Panels show height and phase, respectively, for colloidal crystals made from 280-2 (a, b), 300-1 (c), and 500-2 (d).

A.3 Results and Discussion

This novel material is created by using low temperature annealing of microgel particles into a physically cross-linked, non-covalent colloidal crystal. The novelty is that these materials are stable and able to swell in water, though they are not thermoreponsive. Using the Bragg equation (A.1),

$$m\lambda = 2nd \cdot \sin\theta \qquad \text{(A.1)}$$

where m is the diffraction order, n is the refractive index of the material, d is the spacing and θ is the angle of incidence, the center-to-center distance (or diameter) of the particles determined by AFM allowed for the prediction of the wavelength expected to be generated by particles at those wavelengths. Several assumptions were made: the diffraction order was assumed to be 1 for a face-centered cubic crystal, and the refractive index was assumed to be 1.45, which is the refractive index for polystyrene. The angle of incidence used was 90° since the reflectance spectroscopy was performed at that angle. These results are tabulated in Table A.1. It is concluded from the data that the particles swell in an isotropic fashion given that the measured dimensions provide calculable data that matches reasonably well with the measured data taken using UV/vis spectroscopy. The AFM data also indicate that these particles exhibit phase separations in their macrostructures. This phenomenon is exhibited most clearly in the phase data (all figures). Because the phase data is an indication on how the cantilever tip is interacting with the sample, it is reasonable to assume that fluctuations of the phase data are changes

in the hydrophobicity or stickiness of the particle surface. Since these particles are composed of a very non-polar, hydrophobic polymer and a more hydrophilic polymer, it is reasonable to expect that if phase separation were to occur, the tip would interact differently as it went from phase to phase. This phase separation is possibly the reason why these particle form crystals so easily and remain robust. The annealing of the crystal most likely enhances the phase separation and

Table A.1. Tabulated results for the samples baked for 6 days as determined by AFM.

Sample[1]	AFM Diameter	Calculated λ	TEM/DLS Diameter[1]	Measured λ[1,2]
280-2 Dry	180 nm	426 nm	203 nm	415 nm
280-2 Wet	213 nm	504 nm	278 nm	550 nm
300-1 Dry	217 nm	514 nm	219 nm	500 nm
300-2 Wet	235 nm	556 nm	246 nm	625 nm
500-2 Dry	215 nm	509 nm	268 nm	650 nm
500-2 Wet	327 nm	774 nm	318 nm	815 nm

[1]Provided by Dr. Jonathan McGrath
[2]Measured with UV/Vis reflectance spectroscopy at an incident angle of 90°.

is probably the mechanism by which these crystals become stable after baking. The 280-2 sample shows the phase separation best in solution (Figure A.6), while the 500-2 sample shows it best in air (Figure A.3), though all of the phase images show what appears to be phase separation in each of the dried samples (Figures A.1, A.2, A.3, A.4, and A.5). Since the baking temperature is just below the T_g of the copolymer[10] of polystyrene and pNIPAm (determined to be 111.5 °C and 134 °C), it is reasonable to assume that the temperature is high enough to ensure that one of the polymers melts and its phase separates to form physical cross-links that are entropically favored. There is some additional indication in the AFM images that the phase separation within the particles is only fully developed after baking and wetting. Samples that were baked, but not pre-wetted, were also imaged (Figures A.4 and A.5); and they show some evidence of phase separation but not to the extent of the wetted samples.

References

1. Kesavamoorthy, R.; Super, M. S.; Asher, S. A., "Nanosecond photothermal dynamics in colloidal suspension." *J. Appl. Phys.* **1992,** 71, 1116-1123.

2. Asher, S. A.; Holtz, J.; Liu, L.; Wu, Z. J., "Self-Assembly Motif for Creating Submicron Periodic Materials - Polymerized Crystalline Colloidal Arrays." *J. Am. Chem. Soc.* **1994,** 116, 4997-4998.

3. Weissman, J. M.; Sunkara, H. B.; Tse, A. S.; Asher, S. A., "Thermally switchable periodicities and diffraction from mesoscopically ordered materials." *Science* **1996,** 274, 959-960.

4. Holtz, J. H.; Asher, S. A., "Polymerized colloidal crystal hydrogel films as intelligent chemical sensing materials." *Nature* **1997,** 389, 829-832.

5. Pan, G. S.; Kesavamoorthy, R.; Asher, S. A., "Optically nonlinear Bragg diffracting nanosecond optical switches." *Phys. Rev. Let.* **1997,** 78, 3860-3863.

6. Lee, K.; Asher, S. A., "Photonic crystal chemical sensors: pH and ionic strength." *J. Am. Chem. Soc.* **2000,** 122, 9534-9537.

7. Churochkina, N. A.; Starodoubtsev, S. G.; Khokhlov, A. R., "Swelling and collapse of the gel composites based on neutral and slightly charged poly(acrylamide) gels containing Na-montmorillonite." *Polymer Gels and Networks* **1998,** 6, 205-215.

8. Hu, Z. B.; Lu, X. H.; Gao, J., "Hydrogel opals." *Adv. Mater.* **2001,** 13, 1708-1712.

9. McGrath, J. G.; Bock, R. D.; Cathcart, J. M.; Lyon, L. A., "Self-Assembly of "Paint-On" Colloidal Crystals Using Poly(styrene-co-N-isopropylacrylamide) Spheres." *Chem. Mater.* **2007,** 19, 1584-1591.

10. McGrath, J. G. Synthesis and characterization of core/shell hydrogel nanoparticles and their application to colloidal crystal optical materials. 2007.

VITA

Courtney D. Sorrell

Courtney was born and raised in Chapel Hill, North Carolina, where she attended public schools and developed her love of college basketball. She received an A.A. from Oxford College of Emory University in May 1998, and a B.A. in political science and chemistry from Emory University, Atlanta, Georgia, in May 2000. She worked in industry for three years before coming to Georgia Tech to pursue a doctorate in chemistry. During her term in graduate school, Ms. Sorrell was the recipient of a first prize in the SAIC Paper Contest and the Sam Nunn Security Fellowship. She hopes that her love of politics and science will combine into a fulfilling career so that she can work towards making the world safer, cleaner, and more energy efficient. When she is not working on her research, Ms. Sorrell enjoys traveling, cooking, sewing, reading, listening to music, and watching movies. She also enjoys outdoor exercise as well as fundraising and community service. She lives alone with her cat, Savannah, and has a mildly unhealthy obsession with Canada.